ADVANCES IN PHYSICS AND APPLICATIONS

EDITORS :

DR. POPPY HAZARIKA
DR. NILIMA GOGOI

Advances in Physics and Applications (APA-2020)

Editors:

Dr. Poppy Hazarika

Dr. Nilima Gogoi

Preface

In the year 2020, the Department of Physics, Duliajan College, Duliajan completed glorious 25 years of offering honours in Physics. A series of events were planned to celebrate this special year. However, an unprecedented situation in the name of "Covid-19" struck the whole world. Humanity was in danger and chaos. Every country was locked down with people confined to their homes most of the year. But life must go on as well as the desire to gain and propagate knowledge. It was necessary to show hope especially among the student community. With this aim, the Department of Physics in collaboration with IQAC, Duliajan College, Duliajan proceeded with the plan albeit electronically to conduct a *1 week Lecture series in Physics and International e-Poster Conference on "Advances in Physics and Applications (APA-2020)" from 23rd to 28th November 2020.* The lecture series comprised of talks on pure as well as interdisciplinary physics by eminent national and international faculties. The simultaneously held e-Poster conference covered the recent research and developments in various domains of physics. As a part of this lecture series and e-Poster conference, we had planned to bring out an edited book entitled *"Advances in Physics and Applications (APA-2020)"* with ISBN. This book is intended for all those students, teachers, researchers and academicians who's interest lies in and with physics.

Date: 2nd July, 2021

Editors
Poppy Hazarika
Nilima Gogoi

Acknowledgement

We would like to acknowledge the honourable Principal of Duliajan College, Duliajan, Dr. Lok Bikash Gogoi for his allround support and encouragement starting from the process of holding the lecture series and e-Poster conference to the final moment of publication of this book. We would also like to thank Joint Co-ordinators of IQAC, Duliajan College, Duliajan, Mr. Jayanta Dutta and Dr. Dayananda Nath for their constant suggestions and help. We would also like to express our gratitude to our department colleagues Ms. Bhagyalakhi Baruah and Dr. Dipraj Saikia for their engagement and help throughout the process of publication of this book. We also thank our well wishers and ex-faculties of our department Dr. Dip Saikia, Mr. Sadananda Dutta and Dr. Likhon Chandra Borah for their kind words. Finally, we would like to thank all our esteemed contributors and reviewers because of whom this book has taken a genuine and reliable form. We also take this opportunity to thank our publishers "The Assam Computers" for their consent to publish this book and turning it into its present beautiful form. Any copyright infringement made unintentionally and unknowingly is regretted from our side.

Date: 2nd July, 2021

Editors

Poppy Hazarika

Nilima Gogoi

IV

DULIAJAN COLLEGE

Ref. No.: DC/PO/Misc/Message/2021/081   Date: 15.07.2021

Message from the Principal

It has given me immense pleasure to know that Physics Department of Duliajan College is going to publish an Edited Book of research papers presented in the "1 Week Lecture Series and International e-Poster conference" organized by the department under the heading "Advances in Physics and Applications(APA-2020)" held in the month of November 2020.

In recent times, quality of higher education is one of the most significant and widely discussed topics in our learned societies. For quality education in a higher educational institution the quality teaching is one of the major factor without which it would be impossible to reaching the expectations of the learners. Here, we need innovative teacher's role by analyzing real challenging situations faced by the students. So, self development is an important aspect of quality improvement in teaching learning process which transforms the teachers to be a subject expert. The steps taken by Physics Department of Duliajan College by organizing Lecturer Series and International e-Poster conference and also publishing a Edited Book on that occasion is definitely a much needed step towards that goal.

I would like to offer my sincere thanks and gratitude to all the members of Physics Department and also to the contributors of the Edited Book.

Dr. L. B. Gogoi

Principal,

Duliajan College, Duliajan

Vi

Encouraging Words from Peers......

"I have immense pleasure to memorize and express in words about glorious journey of Physics Department of Duliajan College. With able leadership of head of Department, Dr Niranjan Baruah, we tried our best and able to get permission to open HONOURS Course in 1995. One of the FIRST BATCH students passed as expected. Our glorious journey started from 2000 batch, as Miss Binita Pathak secured FIRST CLASS DISTINCTION and Second position in the Dibrugarh University. The same journey is still ahead with new hope and enthusiasm. I sincerely acknowledge the devotion to duty of my colleagues late Dr Niranjan Baruah, Dr Likhon Chandra Borah, Dr Dip Saikia with whom I served the department and with our joint effort, we were able to achieve a prestigious position at Dibrugarh University. I hope, the ongoing stake holders of Physics Department would try their best to maintain the achieved position and uplift to a better place. Again, I express sincerely to the organisation"

-----Mr. Sadananda Dutta
Retired faculty, Physics, Duliajan College

"The past can never be forgotten. Even after retiring as the HoD, Physics, Duliajan College on 31st December 2019, the fond memories of the department keep visiting me. At the time of retirement, we had Dr. Poppy Hazarika, Dr. Nilima Gogoi and Arjuna Phukan (Contractual) as faculty members. I am pleased to know that the department now has four young permanent faculty members. In the year 2020, the Department of Physics had completed 25 years of offering honours in Physics. To mark this occasion, both Dr. Poppy Hazarika and Dr. Nilima Gogoi in collaboration with IQAC, Duliajan College, Duliajan organised an online 1 week Lecture series and e-poster conference successfully in the month of November, 2020. I appreciate their effort. I am also happy to know that as a part of this initiative, they are coming out with an edited book entitled "Advances in Physics and Applications (APA-2020)". The resources available in the book will surely be helpful for the scientific community at large.

I believe that the present faculty members of the Department of Physics, Duliajan College, Duliajan will work single mindedly and sincerely towards a better future keeping pace with the changing times."

-------Dr. Likhon Chandra Borah
Ex. Vice Principal, Duliajan College and Retired faculty, Physics, Duliajan College

"I am glad to know that the Department of Physics , Duliajan College organized an one week lecture series in physics and international e-poster conference on "Advances in Physics and Application (APA-2020") during 23-28 November, 2020 as a part of the Silver Jubilee celebration of the Department . The event was held in online due to the COVID pandemic condition.

The organizer is going to publish few selected articles from the event in the form a volume. I appreciate the organizer in this regard.

I deeply thank the authors for their enthusiastic and high grade contribution. I hope the volume will attract the interest of academician and researchers."

-------Dr. Dip Saikia
Principal, Digboi College, Digboi-786171
Ex- Faculty, Physics, Duliajan College

VI

TABLE OF CONTENTS

VII

LIST OF TABLES

Chapter 1:   TINY ATMOSPHERIC PARTICLES: BIG IMPACT ON HUMAN RACE

Binita Pathak

Dibrugarh University, Dibrugarh, 786004, Assam
Email:binita@dibru.ac.in

1. Introduction

A major surprise of the Apollo Moon missions was the detrimental impact of lunar dust on the astronauts during moonwalks and other external actions even inside the Command and Service Module during their return to Earth. Dust storms are recurrent on the surface of other planetary bodies like Mars, Titan, etc. The experiences by 41 Mars scientists, mission engineers and planners, and medical researchers have led to the publication of a book entitled "Dust in the Atmosphere of Mars and its Impact on Human Exploration," published in 2018. On Earth as well, dust from Deserts is quite common, and we are also familiar with road/continental and industrial dust. The dust can evolve at any place in the globe, particularly in desert regions and can be transported to distant places several kilometres away by wind within a time scale of 4-10 days. For example, Asian desert dust originated over the Taklamakan desert of China can be transported across the Pacific Ocean and North America to the Atlantic is evidence of such a long-range dust transport; a dust storm in the Sahara can alter the Miami Skies and temperatures in the North Atlantic, as revealed by satellite images. The atmospheric pipeline of dust from the Sahara Desert covering a 6,000-mile trip contributes to the existence of the Amazon rainforest, without which the forest can undergo a massive biological change. Hence, the Earth scientists keep a close watch on the dust storms on Earth, which can darken skies and alter Earth's climate patterns through currently available about 16 active polar-orbiting satellites that provide unprecedented views of the size, scale, distribution, and movement of the dust storms from space. Not only desert dust but the industrial dust that originated over the *Asian region during the summer monsoon season can reach American continents crossing the Atlantic Ocean.* In this way a regional problem becomes global.

We are familiar with dust in the atmosphere. Still, the important message here is that it is only a category of omnipresent tiny particles either in solid or liquid phase present in the atmosphere, known as 'aerosols'. When we inhale the fresh and clear morning air or the dense and polluted evening air, we inhale millions of solid and liquid aerosols particles of size ranging from a few nanometres to tens of micrometers. Aerosols can also make their way into the atmosphere depending on the season and weather conditions prevalent in a particular area. About 90% of the aerosols present in the atmosphere are produced from natural sources like volcanoes, wild forest fires, vegetation, sea salt, dust, etc. The rest 10% are considered anthropogenic or human-made. Fossil fuel combustion, biomass burning, deforestation, overgrazing, excessive irrigation, industries, incinerators, smelters, power plants, etc., are some of the anthropogenic (human-made) activities through which sulfate aerosols, black carbon, organic carbon, nitrates, and other particles are released into the atmosphere. Anthropogenic aerosols also include indoor pollutants caused by cigarettes, cooking stoves, fireplaces, perfumes, candles, etc. The recent pandemic essence 'SARS-CoV-2', the COVID 19 disease causing virus falls under the bioaerosol category along with bacteria, fungi, pollen, spores etc.

The physical properties (shapes, sizes, and structure, concentration, density, mixing state etc) of the aerosols are described differently by different specialists. Climatologists and meteorologists use the term particulate matter (PM): PM_1, $PM_{2.5}$ and PM_{10}) depending on their size <1 µm, <2.5 µm, and <10 µm respectively. Some call these nanoparticles, Aitken particles, accumulation particles, coarse particles etc. According to the shape of the particles, aerosols can be categorized as isometric particles (all *three dimensions are roughly the same*), platelets (*two long dimensions and one small third dimension, like a leaf fragment*) and fibers (*great length in one dimension and much smaller dimensions in the other two, like threads or mineral fibers*) Aerosols usually exist as complex

mixtures; for example, particles of black carbon from soot or smoke mix with nitrates and sulfates or sometimes coat the surfaces of dust, creating hybrid particles. Various patterns of aerosols generated over both ocean and land (*dust plumes in deserts, plumes of black and organic carbon from vehicular emissions, sulfates from coal power plants, soil dust from agricultural lands etc*) by nature can be observed from space by the satellites. Usually, aerosols do not have a very long lifetime and remain suspended in the atmosphere for concise periods of four days to a week. Due to wind, these particles can travel long distances up to thousands of kilometers, as already mentioned. It is known that the physics, chemistry, and optical characteristics of atmospheric aerosols are closely related to homogeneous- and heterogeneous-phase chemical reactions. This results in a series of environment problems, including air quality degradation, ozone layer destruction, acid rain formation, and smoke-fog related accidents. *The effects of aerosols on the atmosphere, climate, public health, quality of human life, agriculture, and economy are among the central topics in current environmental research.*

2. Aerosol impact on Weather and Climate

The Sun is the ultimate source of energy for all forms of life on the earth and it drives the Earth's climate system comprising of biosphere, geosphere-lithosphere, atmosphere hydrosphere, cryosphere. The atmosphere acts as a shield which protects the extremities of the sunlight and balances the heat within it. All these effects occur due to the presence of the aerosols in the atmosphere. Aerosols absorb or scatter sunlight depending on their physical properties. Based on this interaction with earth's radiation field, atmospheric aerosols play an important role in the earth's climate through climate forcing and climate feedback mechanisms (Hansen et al., 1997). The perturbation in Earth's radiation budget is known as the climate forcing or radiative forcing due to aerosols. The "climate forcing" that forces the temperature of the earth's surface-atmosphere system to change by modifying the balance between incoming and outgoing radiative energy fluxes, is estimated as the energy per unit area (in watts per meter square, Wm^{-2}) (Seinfeld et al., 1996). Climate feedback is the consequences of changes in weather conditions experienced in response to aerosol forcing, in terms of meteorological variables: surface or atmospheric temperature, precipitation, wind, relative humidity, solar insolation duration etc. The radiative forcing indicates the net change in solar flux at the top of the atmosphere, surface, or within the atmosphere with and without the presence of the aerosols (e.g., Hansen et al., 1997). This change is defined such that a negative/positive radiative forcing implies that the presence of aerosols exerts a cooling/warming effect. Aerosols interact with solar radiation through different mechanisms (Fig. 1-1). Aerosols directly scatter and absorb sunlight which is termed as the "**direct effect**" of aerosols (e.g., McCormick and Ludwig, 1967) on short wave radiation. The scattering aerosols (like sulphate, organic compounds, sulphuric acid, nitrates etc) reduce the planetary albedo and allow less radiation to reach Earth's surface. This results into a reduction of the atmospheric and surface temperature of the earth. At the same time, the absorbing aerosols also reduce the surface reaching flux, reducing the surface temperature but it tends to warm the atmosphere. The direct aerosol effect is reported as -0.35 (-0.85 to +0.15) Wm^{-2} (Intergovernmental Panel on Climate Change, IPCC report 2013) (Fig. 1-2). Earlier IPCC (2007), has clearly indicates that aerosol, as greenhouse gases, is also an important factor impacting climate change.

Aerosols can also affect the radiation budget indirectly by acting as cloud condensation nuclei (CCN) (on which water vapour condenses to form clouds) and thus affecting cloud microphysics. Increase in aerosol concentration leads to formation of large number of small radii clouds. The cloud albedo becomes more (highly reflecting), inducing a negative radiative forcing, which is referred to as the first indirect or the Twomey effect. Under such situation, clouds' lifetime become more as it takes time to grow in size to rain drops, which again depends on amount of water required and precipitation is prohibited (second indirect effect). The entire mechanism is termed as indirect effect or aerosol-cloud interaction (ACI) In addition, highly absorbing type of aerosols, such as black carbon, may reduce cloud cover and liquid water content by heating the cloud and the environment within which the cloud forms. This effect is semi-direct (Hansen et al., 1997) because in this process aerosols reacts directly with radiation but indirectly influences cloud properties. The type and surface of aerosols play
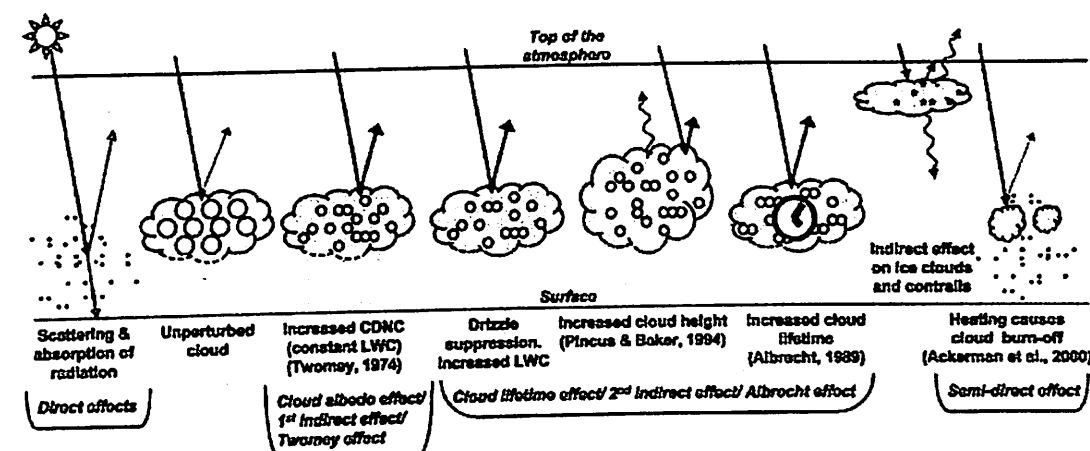
Fig. 1-1. A schematic diagram representing the strong aerosol interaction with solar and terrestrial radiation under

a significant role in determining its radiative/climate impact. Also, the deposition of absorbing aerosols on highly reflecting surfaces like snow and ice not only alters the radiative balance (warming of surface) but also changes the surface albedo (snow darkening effect) (Chylek et al., 1983).

According to the estimates cooling driven by aerosol effect is half the warming caused by greenhouse gases on a global scale. These effects are much uncertain and vary from place to place depending upon space and time. The inconsistency in measuring aerosols within clouds is one of the main drawbacks leading to the partial understanding of aerosol indirect effects. Despite the recent progress and advancement, the study on aerosol influence on climate still remains challenging.

3. Aerosol effect on Antarctic Ozone Hole

Aerosols have the potential to significantly influence our entire planet through their role in heterogeneous chemistry in the troposphere and stratosphere. The depletion of Ozone concentration in the stratosphere in Antarctic region is the well known "Antarctic Ozone Hole" phenomenon. Aerosols can act as sites for chemical reactions to take place (heterogeneous chemistry) in the stratosphere. During winter in the Polar Regions, aerosols grow to form polar stratospheric clouds. The large surface areas of these cloud particles provide sites for chemical reactions to take place. These reactions lead to the formation of large amounts of reactive chlorine and ultimately, to the destruction of ozone in the stratosphere. Evidence now exists which shows similar changes in stratospheric ozone concentrations occur after major volcanic eruptions. For example it was observed in 1993-1994 after Pinatubo eruption that ozone values fell to unusually low levels.

4. Societal impact of aerosols:

Aerosols can affect daily activities by pushing grit through windows and doors, forcing people to stay indoors, causing breathing problems, reducing visibility and delaying flights, and by and large, creating chaos. Some of their long-lasting consequences are discussed below.

4.1. Effects of Aerosols on Air Quality, Human Health and Quality of Life

The COVID 19 outbreak has made us experience existence of atmospheric aerosols and their impact on the human race in an incredible way. It is well established that the SARS-CoV-2 virus that causes COVID-19 predominantly disseminate from person to person through droplet nuclei or aerosols transmission. The droplets formed from the respiratory fluid released during exhalation (e.g., quiet breathing, speaking, singing, exercise, coughing, sneezing) in the form of droplets across a wide spectrum of sizes, with the virus as the nuclei through 'aerosolization' process. The largest droplets (size >10 μm) settle out of the air rapidly, within seconds to minutes, while the fine droplets/aerosol particles can remain suspended in the air for minutes to hours. They can be suspended in the air over

long distances and time, making indoor air more unsafe. Thus creating a healthy building through engineering controls in spaces is a crucial component of combating COVID-19. Apart from this virus, other bioaerosols play an important role in spreading biological organisms and reproductive materials and they can cause or enhance human, animal and plant diseases. These are linked to many different adverse health effects ranging from infectious diseases to acute toxic effects, allergies, asthma and even cancer. Bacteria and fungi within the size range of 1-10 μm may reach the alveoli of lungs and affect the human respiratory system. The bacterial bioaerosols are related to human diseases, like pneumonia, tuberculosis, brucellosis, anthrax, and Q fever, whereas. Fungal bioaerosols are the etiological agents of respiratory diseases, like allergic rhinitis, asthma. Studies now have established that indoor air pollution is more harmful than outdoor air pollution. According to the United States Environmental Protection Agency, indoor air pollutant levels are often ~2 to 5 times higher than outdoor. In some cases, these can exceed 100 times that of outdoor levels of the same pollutants.

It has been proven that air pollution, including both indoor and outdoor, is now fully recognized to be responsible for public health and environmental degradation. Emission sources release a significant portion of atmospheric aerosols, particulate matter (PM), along with other toxic gases and substances such as tropospheric ozone, Sulphur dioxide, nitrogen dioxide, benzo (A) pyrene etc. In general, PM_{10} particles can penetrate up to the lungs and $PM_{2.5}$, can enter the blood. For health assessment, the particulate matter (PM) concentrations measured are further categorized into the inhalable matter, (PM ≤ 100 μm), thoracic (PM ≤10 μm) and alveolar (PM ≤ 4 μm) particles, based on the capability of aerosols to penetrate up to (or absorbed) the nasal tract, thorax and alveoli respectively of the human body. All the criteria pollutants are responsible for human health degradation and premature mortality via: respiratory diseases, cardiovascular damage, fatigue, headaches, and anxiety, irritation of the eyes, nose and throat, deterioration of the reproductive system, harms liver, spleen, and blood and nervous system. The palaeopathological research also suggests the problems of air pollution. Based on computerized tomography, the images of the bodies of the ancient mummies showed evidence of pneumonia, pulmonary edema, emphysema, and atherosclerosis. In recent years the smog over the cities with poor air flow and dispersal are frequent in winters. According to a study by Lelieveld et al. (2015), the present-day $PM_{2.5}$ concentration is responsible for about 2.1/3.15 million deaths annually, and the rate would increase to 6.2 million/year by 2050. This has motivated policies to edge aerosol emissions. Air quality assessment at local to
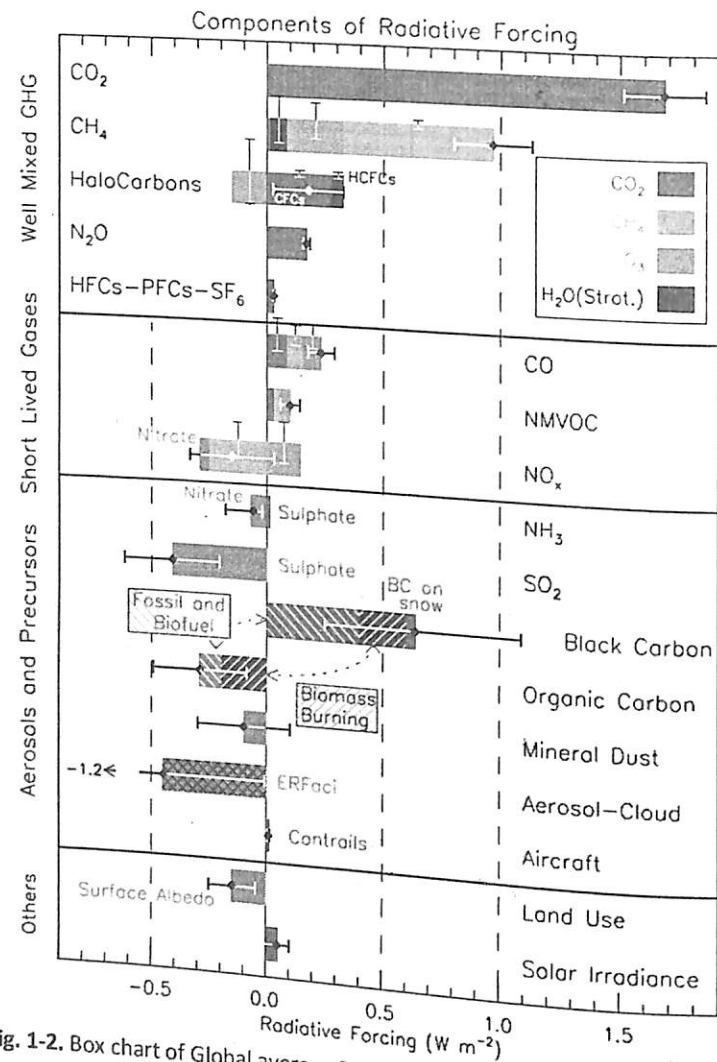
Fig. 1-2. Box chart of Global average Radiative Forcing estimates for emitted compounds or other changes (Courtesy: IPCC 2013)

regional scale is vital for emission control, air quality forecasts. As global economic growth increases, environmental pollution becomes increasingly more serious. The air quality and mortality rate improved during the outbreak of the COVID-19 pandemic due to control in PM concentration through the worldwide lockdown. This effect is experienced both globally and regionally (Pathak et al., 2021 and references therein). Pathak et al., (2021) have shown the improvement of air quality from previous five years moderate air quality to satisfactory level during the nationwide lockdown period.

Further, the air quality and climate change interaction is a widely evolving subject of scientific interest. Climate change-related issues like heat/cold waves etc., and exacerbated underlying conditions associated with it are found to affect human health and mortality to a greater extent. Studies have reported high-temperature extremes in India due to increased abundances of absorbing aerosols (BC and dust), enhancing shortwave heating rate, and altering surface heat fluxes, consistent with the increase in surface temperature (Mondal et al., 2020).

Living in a pollution-free environment signifies a better quality of life. Air pollution in urban areas contain many complex organic chemicals, such as volatile organic compounds (VOCs), polycyclic aromatic hydrocarbons (PAHs), fumigants, and agricultural chemicals, having specific physiological impacts on human health. Therefore, aerosols determine our physical and psychological wellbeing and are closely connected to human existence. With the development of the social economy and environment. Therefore, investigating the impacts of aerosol on human health has been a great concern of the medical science, public health, and atmospheric science communities

4.2. Effects of Aerosols on crop yield and food security

Aerosols affect crop growth by reducing the amount of visible radiation available for photosynthesis. Aerosols have the potential to modulate (raise) minimum temperature indirectly through increased cloudiness. These can also contribute to the spreading of agricultural diseases. For example, bacteria and fungi of plant pathogens cause severe damage to rice and wheat — the staple food grains in Asia. Thus, a decrease in aerosol pollution may lead to an increase in yields. Crop yield is directly related to the economy of an agriculture-based Asian region. The growing industrialization and urbanization have led to the reduction in agricultural land over the Asian countries. This and rising population demand for per capita food consumption threaten food security in Asian countries in the coming decades.

4.3. Aerosol effect on the economy

According to the World Bank's 2000 Annual Review, the health costs in major Asian cities can reach as much as 15-18% of urban income, causing economic hazards. For example, during the life cycle of a dust storm — generation at the source region, transportation along the pathway, and dissipation over the sink area — it can have numerous direct (e.g., injuring people and destroying properties, damaging crops and forests, suffocating livestock, reducing semiconductor yields), indirect (e.g., increasing health costs, depleting fisheries due to a triggered red tide, disrupting transportation (e.g., increasing health costs, shortening the functional life of hydroelectric dams and river channels) economic and communication, shortening the functional life of hydroelectric dams and river channels) economic impacts. Further, heat/cold waves affect the production rate in agriculture and industrial and many outdoor economic activities.

4.4. Aerosol effect on Hydrology, Monsoon, and fresh water availability

It is thought that aerosols suppress precipitation because the particles decrease the size of water droplets in clouds. However, under some environmental conditions, aerosols lead to taller clouds that produce lightning and strong downpours. Meteorologists have even detected a cycle in which the frequency of thunderstorms is connected to peaks in aerosol emissions. A growing number of observational, modeling and satellite-based studies admit that aerosols affect climate through (i) reduction in evaporation and thus slowing down the hydrological cycle (e.g., Ramanathan et al. 2001); (ii) precipitation and circulation pattern changes and reduction in wind speed; (iii) effects on

land surface and sea surface temperature (SST) (e.g., Chung and Ramanathan, 2006) and (iv) effect on monsoon (Lau et al., 2008) etc.

The South West Asian summer monsoon provides up to 80% of the annual mean rainfall received over most regions of India including the North East India and has tremendous impacts on agriculture, health, water resources, economies and ecosystems. Further, the Himalayan Glacier melting is an evident phenomenon under the influence of South/Central Asian biomass burning emission. Such accelerated glacier melting will certainly reduce fresh water availability in future.

5. Conclusions

Aerosol study is included in Atmospheric Physics and Chemistry of the Earth's Atmosphere in particular and is an important topic of Climate Science. Knowledge on aerosols characteristics is vital to critically improve the understanding of climate forcing, air quality, and mutual interactions between the atmosphere and biosphere. The aerosol research is carried out in terms of three methods: laboratory (ground based and satellite observation), modeling, and field studies. It's study in the globe/India started in 1960s/1980s.

The Indian Space research organisation under its Geosphere-Biosphere Programme has set up a network of aerosol observatories named ARFINET (Aerosol Radiative Forcing NETwork) across the Indian subcontinent. Under this network currently more than 40 stations are functional. The 3rd oldest aerosol observatory in India under ARFINET; Dibrugarh University in 1999 is the East Indian region (NEI). The aerosol environment of the NEI is found to be influenced by dust advection from the Indian deserts through westerlies, anthropogenic emissions from the Indo Gangetic plains (IGP), marine emissions from the Bay of Bengal along with local biogenic emissions from large vegetation cover, including primary and secondary bioaerosols as well as local anthropogenic emissions (e.g., biomass burning, fossil fuel burning, oil and gas fields etc.). The eastern part of the region is dominated by biomass burning emissions, while fossil fuel generated trace gases and aerosols override the western part. The columnar aerosols burden exhibits a strong seasonality, a west to east longitudinal (decreasing) and an altitudinal (inverse) gradient. The columnar aerosol loading stands second highest in South Asia next to the Indo Gangetic Plains. The aerosol radiation interaction (ARI), aerosol-cloud interaction (ACI), stratosphere-troposphere exchange during normal and extreme weather events, convective activities leading to elevated aerosol layers are critical over the region. The aerosols of this region are found to affect the surface reaching solar radiation and thus temperature, cloud properties, rainfall to a larger extent.

References

[1] C. Petr, V. Ramaswamy, V. Srivastava, J. Geophys. Res. Oceans. 88 (1983) 1083710843

[2] C. E. Chung, V. Ramanathan, J. Clim. 19 (2006) 2036–2045.

[3] J. E. Hansen, M. Sato, R. Ruedy, J. Geophys. Res. 10 (1997)6831–6864.

[4] K. M. Lau et al, Bull. Am. Meteorol. Soc. 89 (2008) 369– 383.

[5] J. Lelieveld, J. S. Evans,M.Fnais, D. Giannadaki, A. Pozzer, Nature 525 (2015) 367371. E1517.

[6] Mondal, N. Sah, A. Sharma, C. Venkataraman, N. Patil, Int. J. Climatol. 41 (2021) E1498-(2020) 2.

[7] B. Pathak, P. K. Bhuyan, A. Saikia, K. Bhuyan, P. Ajay, S. J. Nath, S. L. Bora, Curr. Sci. 120

[8] V. Ramanathan, J. Geophys. Res. 106 (2001) 28,555– 28,566.

[9] J. H. Seinfeld, S. N. Pandis, Atmospheric Chemistry and Physics: From Air Pollution to Climate Change. John Wiley, New York (1998).

Chapter 2:   PERIODIC ENCLOSED 'SLIME' STRUCTURES AS POLARIZATION-INDEPENDENT MICROWAVE ABSORBER

Sanghamitra Saikia[a] and Nidhi S. Bhattacharyya[a*]

[a]Department of Physics, Tezpur University, Napaam, Tezpur, Assam-784028, India
*E.mail: nidhisbhatta@gmail.com

Abstract

This paper proposes a periodic structure-based microwave absorber with a thickness of 3 mm operating at the 'C' band. The structures are designed using slime and are enclosed within cellulose acetate (CA) as a substrate. Slime for the first time is tested for its absorbing properties. The computational simulations of the designed absorber showed -31.23 dB reflection loss (>90% absorption) at 6.2 GHz with a -10 dB bandwidth of 1.3 GHz and the performance is polarization independent.

Keywords: Metamaterial absorber, slime, cellulose acetate, flexible

1. Introduction

Increasing electromagnetic pollution due to mass utilization of advanced communication devices has resulted in the emergence of new shielding/absorption technology at microwave frequencies. Compact electronic and wireless systems have led to the integration of various components into a single platform putting a constraint on thickness and degree of rigidity. Several thin and flexible water-based metamaterial absorbers with different geometries have been reported [1-6] in the past decade. These absorbers use the advantages of metamaterial structures [7-10] along with good microwave absorption properties of water as unit cells, to manipulate electromagnetic radiations. Water-based absorbers, however, have some potential drawbacks for practical realization as the substrate has to be hydrophobic to retain the shape of the unit cell, thus limiting the material options for the substrate.

'Slime' is a PVA/borate cross-linked polymer that contains plenty of water, making up over 90% of the formula. Higher viscosity of slime as compared to water makes it behaves as semi-liquid thus, making it easier to handle during the absorber development process [11]. In addition, slime has an interesting property of self-healing (retaining its shape after external stress is removed) which is advantageous for flexible absorbers. Herein, slime is used as the resonating structure of the unit cell embedded in cellulose acetate substrate. Cellulose acetate is easy to mold, flexible and lightweight [12-13]. The absorber is designed to operate in C-band and computational simulations are carried out using CST Microwave Studio Suite.

2. Experimental

2.1. Synthesis

Slime is synthesized using three ingredients - polyvinyl alcohol (PVA) with M_W = 146,000 g/mol, borax, and distilled water have been used. The synthesis process is done by mixing 4 wt% of PVA-water and 4 wt% borax-water solutions in 5:1 ratio through vigorous stirring and left undistributed for 12 hours at room temperature (~ 28 °C).

Fig. 2-1. Slime

2.2. Microwave material characterization

Table 2-1

S. No.	Dimensional parameters	Value (mm)
1.	r	3
2.	h	2.4
3.	l	4
4.	t	3
5.	x	0.3

The permittivity of slime is determined in frequency range 1-20GHz at room temperature using a dielectric probe (N1501A) and Keysight material measurement suit software compatible with Agilent Vector network analyzer (E8362C). The permittivity curve is shown in Fig.2-2.

From pieces of literature [12-13], the permittivity of cellulose acetate is found to be 5.2 and the loss tangent to be 0.038 at microwave frequency range. The obtained values for permittivity of slime and cellulose acetate are applied to CST Microwave Studio Suite software for further computational calculations using permeability =1. The density of slime is determined using Archimedes principle and found to be 1540 kg/m^3.
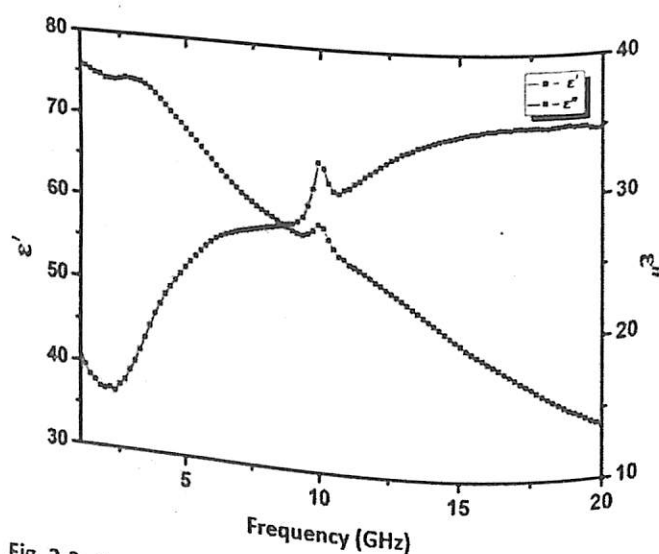
Fig. 2-2. Permittivity curve in frequency range 1-20 GHz at room temperature, where ε' = real permittivity (energy stored) and ε'' = imaginary permittivity (dielectric loss).

3. Design and Simulation

The optimized unit cell design is as shown in the Fig. 2-3. The slime unit cell is enclosed in cellulose acetate forming a capsule. Fig. 2-3 shows the schematic of the design. The optimized parameters are shown in the table 2-1.

In the simulation, electromagnetic wave (linear) is incident on the absorber in the direction of z-axis. Simulation is repeated for circular as well as elliptical polarization. Unit cell boundary conditions are applied for simulation.
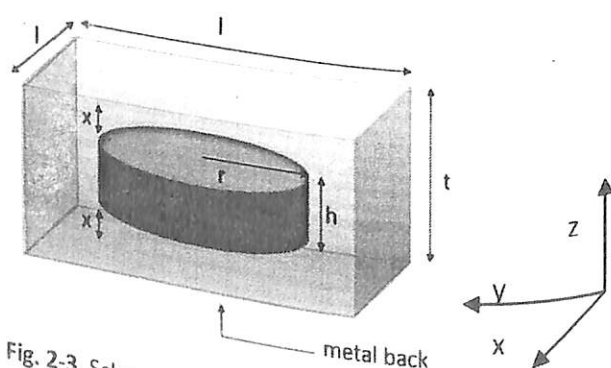
Fig. 2-3. Schematic of the proposed absorber unit cell.

4. Results and discussion

Simulation results of reflection loss curve, current density, surface current, E-field, and H-field distribution for the designed unit cell are shown in the Fig. 2-4. A reflection loss of -31.23 dB is obtained at 6.2 GHz with a -10 dB bandwidth of 1.3 GHz shown in Fig. 2-4(a). Interaction of the microwave penetrating through the absorber at the resonating frequency, 6.2 GHz can be understood through field analysis. The arrow marks in the figures show the direction of the field lines. The direction of current density or the loop current resulted from the interaction of incident wave and the 'slime-tablet' in Fig. 2-4(b), is 180° out of phase with the surface current, in Fig. 2-4(c), on the ground plane at the resonant frequency. These antiparallel currents couples with magnetic components of the impinging TEM(transverse electromagnetic)wave and wave vector at right angles which further partially contributes to effective permeability while the major contributor is the magnetic resonance. This magnetic resonance is generated due to the strong coupling of magnetic field Fig. 2-4(d) of the incident wave with the 'slime-tablet'. Moreover, the magnetic field inside the 'slime-tablet' is surrounded by currents loops that result in strong magnetic resonance at phase 20° of the incident wave. An electric response Fig. 2-4(e) is generated by the 'slime tablet' along with the ground plane when the microwave encroaches, this contributes to the effective permittivity. Electric and magnetic resonances together contribute to obtain the impedance matching conditions. E-field concentration in Fig.4(e) is mainly confined to the 'slime' edges creating two displacement current loops at phase 120° of the incident wave as the permittivity of cellulose acetate (5.2) is less than that of slime (~ 65) at the resonant frequency. The dipole moment of the 'slime-tablet' couples strongly with the incident wave-field components which contribute further to the absorption.

Absorption is mathematically given as $A(\omega) = 1-R(\omega)-T(\omega)$, where $R(\omega) = |S_{11}|^2$ is the reflectance, and $T(\omega) = |S_{21}|^2$ is the transmittance. Since the designed absorber is metal-backed, therefore the transmittance becomes zero, $|S_{21}|^2 = 0$.

The design shows constant reflection loss curve while changing the polarization of the incident wave. Thus, the designed absorber can be considered as polarization independent.
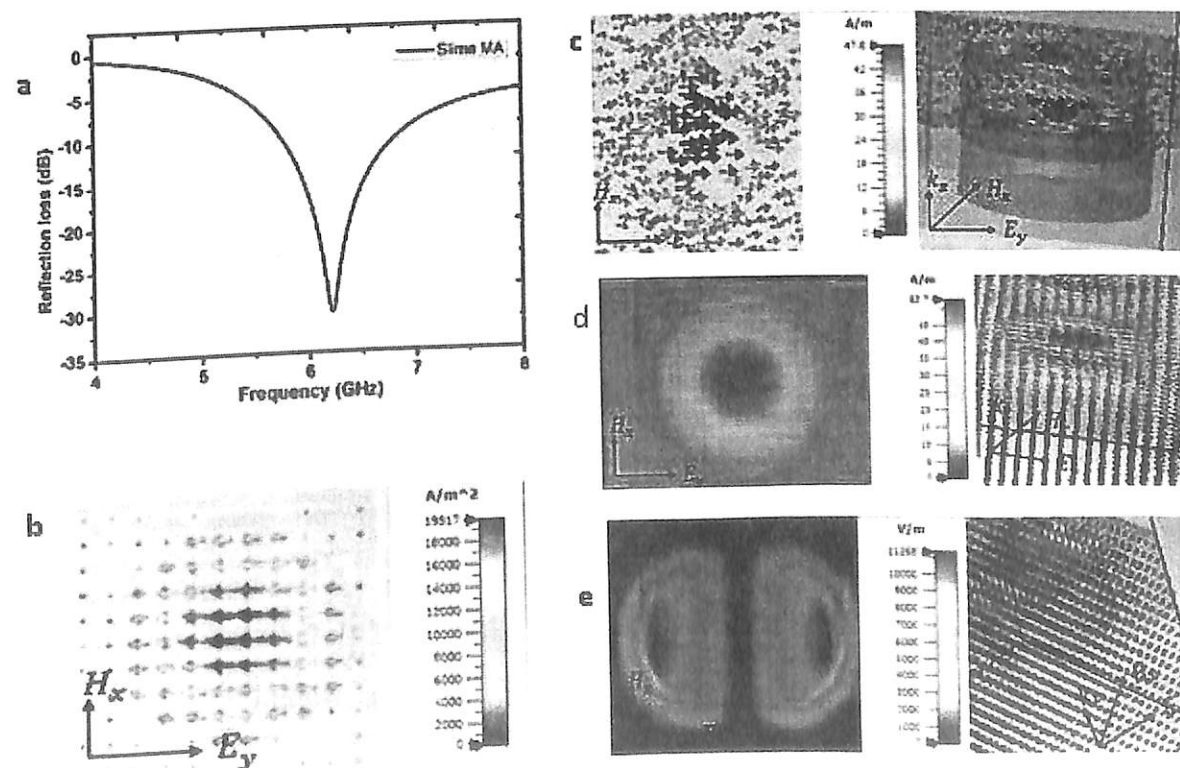
Fig. 2-4. (a) Reflection loss curve, (b) current density, (c) surface current, (d) E-field distribution and (e) H-field distribution obtained for designed absorber

5. Conclusion

This work reports a polarization-independent microwave absorber with a thickness of 3mm designed at 'C'-band which absorbs (>95%) at resonating frequency 6.2 GHz with -10 dB bandwidth of 1.3 GHz. Moreover, the designed absorber is lightweight and cost-effective. Slime showed good performance as an absorber material. The designed absorber has many future scopes and has potential applications. 'Slime' can be used for designing optically transparent absorbers. Both the polymers in the designed absorber contribute to efficient absorption of electromagnetic wave. Further, the use of slime has the added benefit of the realization of a low-profile absorber.

References

[1] X. Zhang, F. Yan, X. Du, W. Wang, M. Zhang, AIP Advances 10 (2020) 055211.
[2] J. Zhao, et al, Optics express 26 (2018) 8522.
[3] D. J. Gogoi, N. S. Bhattacharyya, Journal of Applied Physics 122 (2017) 175106.
[4] J. Xie, et al, Optics express 26 (2018) 5052.
[5] Z. Wu, et al, Applied Physics Express, 12 (2019) 057003.
[6] X. Zhang, et al, IEEE Antennas and Wireless Propagation Letters 19 (2020) 821.
[7] I. A. Buriak, V. O. Zhurba, in: 9th International Kharkiv Symposium on Physics and Engineering of Microwaves, Millimeter and Submillimeter Waves (MSMW), vol. 20, 1, 2016.
[8] K. Tantiwanichapan, et al, Progress In Electromagnetics Research 87 (2019) 33.
[9] J. Lee, Y. J. Yoon, S. Lim, ETRI Journal 34 (2012) 126.
[10] S. Agarwal, Y. K. Prajapati, Optics Communications 439 (2019) 304.
[11] E. Z. Casassa, A. M. Sarquis, C. H. Van Dyke, Journal of Chemical Education 63 (1986) 57.
[12] D. C. Trivedi, S. K. Dhawan, P. N. Prasand, J. K. Nigam, Frontiers of Polymer Research,1992.
[13] H. Lv, X. Wang, C. Ma, L. Ma, Journal of Engineered Fibers and Fabrics 12 (2017) 72.

Chapter 3:   COUPLING STRENGTH BETWEEN DUST GRAINS IN COMPLEX PLASMA IN PRESENCE OF ASYMMETRIC ION FLOW AND DUST CHARGING DYNAMICS

Saurav Bhattacharjee[a]*, Barlin Das[b]

[a]*Department of Physics, Tinsukia College, Tinsukia, Assam, India*
[b]*Department of Physics, Dibrugarh University, Assam, India*
E.mail:sauravtsk.bhattacharjee@gmail.com

Abstract

Interaction mechanism among dust grains immersed in plasma has been reported theoretically in presence of asymmetric ion flow and dynamical charging of dust grains. The ion flow induced particle-wake interaction in addition to repulsive Yukawa type of interaction found to play a significant role in tuning the coupling strength between charged grains and hence the vibrational mode.The transition in coupling strength is obtained as a characteristic of ion flow speed and grain size. The results show a damping in strength of interaction in presence of dynamical charging of dust. The type of interaction shows a mixed phase of Wake-Yukawa in subsonic regime and highly Yukawa dominating phase in supersonic regime of ion flow. The results are significant for understanding the thermodynamic properties and the phase behaviour of colloidal systems and nano-crystals.

Keywords: plasma crystal, ion flow

1. Introduction

The study of inter grain interaction is of fundamental interest in statistical thermodynamics. The phase behavior and the dynamics of a system depend solely on the type and strength of inter grain interaction. Realization of correct and appropriate interaction potential is one of the biggest challenges in many-body systems. The complex plasma or dusty plasma is an immerging branch of research for last few decades because of its strong potentiality to replicate the strongly correlated systems at larger scale. The complex plasma consists of micron-submicron sized dust grains immersed in ambient plasma and radiative background. The dust grains are charged up to a high value of 10^3 to 10^4 electronic charges by various processes [1-2]. In laboratory dusty plasma experiments, the dust grains are commonly negatively charged due to higher electron mobility towards the grains. Because of comparatively larger size of the grains, they can be observed individually and this makes it possible to investigate various phenomena such as phase transition [3], diffusion, self-organization [4] etc. at macroscopic kinetic level.

The interaction mechanism around a test dust charge in an isotropic system is caused mainly due to spherically symmetric Yukawa type of potential [5]. Under suitable conditions, when the intergrain interaction is much higher as compared to their thermal energy, the grains show some regular oriented structures, the so called plasma crystals [4,6]. Near the plasma sheath, where laboratory plasma crystals are formed by balancing the gravity and sheath electric field, there is ion streaming towards the lower electrode. This bombardment of ions over shield the spherical dust Debye cloud and elongate it in lower vertical direction. Thus, an asymmetry in charge distribution arises around the grain along the direction of ion flow. This access accumulation of positive charge in the lower side of the grain attracts other dust grains just below it to align along vertical ion flow direction [7] and shows vertical ordering of dust grains (chain formation) often observed in laboratory experiments [8-10]. This leads to an attractive type of interaction potential along vertical direction named as wake potential [11-12].

Most of the theoretical results aim to study the intergrain interaction is based on stationary charge on dust surface. However, in reality the charge on the dust grains exhibit self-consistent fluctuation in response to the oscillation in plasma currents flowing into them. The charge fluctuation on dust surface leads to some new observations [13-14] based on the damping of electrostatic wave [15].

The study of inter grain interaction is primarily based on the local plasma environment surrounding the dust. This also helps to reduce the multi-component scenario of dusty plasma to one component plasma (OCP) model of dust subsystem. In this letter, we have reported analytical expressions of intergrain interaction potential having background asymmetric ion flow towards the sheath and self-consistent fluctuation of dust charge, for two vertically placed dust subsystem. The potentials thus obtained show a damping in strength in presence of dust charging dynamics.

Moreover, the strength of interaction along the direction of ion flow is found as a characteristic ion flow speed and grain size. The type of interaction in subsonic regime of plasma flow is found in a mixed phase of repulsive Yukawa and attractive wake potential, whereas the supersonic regime is found in Yukawa dominating phase. The presence of this mixed phase in subsonic regime shows an interesting anomalous phase transition of plasma crystal reported recently by Saurav et.al. [16], which is commonly observed in solid state crystals undergo ion irradiation [17].

Since, the interaction potential is the key to understand the phase behavior of a system, the results reflect a tuned transition in crystal phase based on ion flow speed and particle size, which is of fundamental scientific interest in metal nano crystals [18-19] because phase control is the only step to improve the functionalities for various applications.

2. Theoretical Formulation

Our theoretical model composed of an uniform dusty plasma having background Boltzmanian electrons, cold streaming ions and fluctuating negatively charged dust grains, in a collision less scenario, where the collision mean free path is greater than the dust Debye length λ_{De} near the plasma sheath [5, 20]. Dust grains near the plasma sheath encounter a downstream ion flow with uniform velocity u_{io} along z-direction towards the plasma sheath. Under the condition that dust particle radius $a < \lambda_{De}$, one can apply OML (orbital motion limited) theory [21] to describe the charging currents. The dielectric response function in presence of dust charging dynamics is given by [22]

$$\in(\omega,k) = 1 + \frac{1}{k^2\lambda_{De}^2}(1+P) - \frac{k_{\parallel}^2}{k^2}\frac{\omega_{pi}^2}{(\omega - u_{io}k_{\parallel})^2}(1+Q)$$

(1)

propagation vector $k^2 = k_{\parallel}^2 + k_{\perp}^2$, P and Q are normalized electron and ion attachment frequency to dust grain and are given as

$$P = \frac{|I_{eo}|}{e(\eta - i\omega)}\frac{n_{do}}{n_{eo}},$$

$$Q = \frac{|I_{eo}|}{e(\eta - i\omega)}\frac{n_{do}}{n_{io}}M\sqrt{\frac{\pi m_e}{8m_i}}(n_{io}/n_{eo})^{3/2}\left(1 - \frac{2eQ_{do}}{m_i u_{io}^2 r_d}\right)\exp\left(-\frac{Q_{do}e}{K_B T_e r_d}\right)$$

where $|I_{eo}|$ is the equilibrium electron current and is given by $I_{eo} = \pi a^2 e\sqrt{\frac{8k_B T_e}{\pi m_e}}n_e \exp(e\phi_s/k_B T_e)$

for $\phi_s < 0$.

Here $\phi_s = \frac{Q_{do}}{r_d}$ is the dust surface potential or floating potential with respect to surrounding plasma, $\eta = \frac{1}{\tau_c} = \frac{eI_{eo}}{ak_B T_e}\left[1 + \frac{1}{M}\sqrt{\frac{\pi m_e n_{io}}{2m_i n_{eo}}}\exp\left(\frac{-eQ_{do}}{k_B T_e a}\right)\right]$, τ_c is the dust charging time, ω is the frequency of the ion acoustic wave and $k_{\parallel}$ is the propagation parallel to ion flow (along z-direction) towards the plasma sheath.

Using the integral form of electrostatic Poisson equation and dielectric response function given in equation (1), we can write the interaction potential due to a moving test dust charge Q_{dt} based on the model described above as follows:

$$\phi(r,t) = \frac{Q_{dt}}{(2\pi)^3 2\pi\in_0}\int d^3k\, d\omega\, \frac{\delta(\omega - v_t k)}{k^2\in(\omega,k)}e^{ik.r'}$$

(2)

Where $r' = r - v_t t$.

For cold stationary dust grains, $v_t = 0$, as compatible to our physical model, the interaction potential is modified as

$$\Phi(r) = \frac{Q_{dt}}{(2\pi)^3\epsilon_0}\int d^3k\, \frac{1}{k^2\epsilon(0,k)}e^{ik.r}$$

(3)

In steady state and normalized scale of electron debye length, the dielectric response function given in equation (1) can be written as

$$\in(0,k) = 1 + \frac{1+P}{k^2} - \frac{1+Q}{M^2 k_{\parallel}^2}$$

(4)

where it is assumed that $k_{\parallel} \gg k_{\perp}$.

Above equation can be simplified as follows

$$\frac{1}{k^2\in(0,k)} = \frac{k_{\parallel}^2}{(k_{\parallel}^2 - k_R^2)(k_{\parallel}^2 - k_{Im}^2)}$$

(5)

where all k are normalized with λ_{De}. k_R and k_{Im} corresponds to real and imaginary screening modes as a function of $k_{\perp}$, in a complex $k_{\parallel}$ plane.

$$k_R = \sqrt{-A+B}$$

(6)

$$k_{Im} = \sqrt{-A-B}$$

(7)

where A and B are given as

$$A = \frac{1}{2}(k_{\perp}^2 + 1 + P - \frac{1+Q}{M^2})$$

(8)

$$B = \sqrt{A^2 + \frac{k_{\perp}^2}{M^2}(1+Q)}$$

(9)

Using the relation in equation (5) we can write the interaction potential due to test dust particulate in YZ plane in presence of dust charging dynamics as

$$\Phi(r) = \frac{Q_{dt}}{(2\pi)^2 \lambda_{De}\epsilon_0} \int dk_\perp exp(ik_\perp y) \int dk_\parallel \frac{k_\parallel^2 exp(ik_\parallel z)}{(k_\parallel^2 - k_R^2)(k_\parallel^2 - k_{Im}^2)} \qquad (10)$$

where $= \sqrt{y^2 + z^2}$, all y and z are normalized with electron Debye length λ_{De}.

The second part of the above integral can be solved by performing closed contour integration in a complex $k_\parallel$ plane for two poles corresponding to $k_\parallel = k_R$, (real one) gives oscillatory wake potential and $k_\parallel = k_{Im}$, (imaginary one) gives repulsive Yukawa type of potential $\phi_D(y,z)$. Finally using the saddle point integration method one can get the potentials as follows

$$\phi_w(0,z) = \frac{-Q_{dt}}{4\pi\epsilon_0\lambda_{De}}\sqrt{\frac{2\pi}{6zM}}\frac{(1+Q)^{1/4}}{\sqrt{1+P}}sin\left[\frac{z}{M}(1+Q)^{1/2}\right] \qquad (11)$$

$$\phi_D(y,z) = \frac{Q_{dt}\sqrt{\pi}}{4\pi\epsilon_0\lambda_{De}}exp\left(-\sqrt{1+P}\sqrt{y^2+z^2}\frac{(1+P)^{7/4}}{(y^2+z^2)^{1/4}}(z/y)^{1/2}\right) \qquad (12)$$

The expressions for corresponding interaction potential in absence of dust charge fluctuation can be obtained by putting P=Q=0.

The normalized equation of motion for the mode of vibration of two vertically (z-direction) placed dust grains above the plasma sheath in presence of asymmetric ion towards the sheath is given as

$$\frac{d^2 z_{n1}}{dt^2} = [K_z + K_{zw}](z_{n1} - z_{m1}) \qquad (13)$$

Here, we have considered the vibrational mode propagates along y-direction. (n:m) represents the particle pair and $Z_{(n,m)1}$ stands for their displacements from equilibrium positions. The length and time are normalized by λ_{De} and $\sqrt{m_d\lambda_{De}^2/K_B T_d}$ respectively having K_B as the Boltzmann constant and T_d is the dust temperature. K_z and K_{zw} are the spring constant or coupling strength correspond to repulsive Yukawa and attractive wake potential respectively.

Using equation (11), we can write the expression for the normalised Yukawa potential as

$$K_z = \left(\frac{d^2\phi_D}{d(y,z)^2}\Big|y,z=a\right) = \frac{\Gamma\sqrt{\pi}}{2^{9/4}}\frac{(1+P)^{7/4}}{k^{3/2}}exp\left(-\sqrt{2(1+P)}k\right)\left[5/4 + 2^{3/2}\sqrt{1+Pk} + 2(1+P)k^2\right] \qquad (14)$$

Here, a is the average interparticle distance, Γ is the Coulomb coupling parameter [9] and $k = \frac{a}{\lambda_{De}}$ is the screening constant.

Similarly, using equation (12), we get the spring constant for wake potential as

$$k_{zw} = -\sqrt{\frac{2\pi}{6M}}\frac{(1+Q)^{1/4}}{\sqrt{1+P}}\frac{1}{k^{5/2}}\left[\left(\frac{3}{4} - \frac{k^2(1+Q)}{M^2}\right)sin\left(\frac{k}{M}\sqrt{1+Q}\right) - \frac{z\sqrt{1+Q}}{M}cos\left(\frac{z}{M}\sqrt{1+Q}\right)\right] \qquad (15)$$

Thus, the effective spring constant along vertical z-direction is

$$K_{eff} = K_z(Yukawa) + K_{zw}(Wake) \qquad (16)$$

Considering a small oscillation in wave amplitude $z_{n1} = A_z exp\left[i(k_y a - \omega t)\right]$ and substituting this in equation (13), we get the dispersion relation for the transverse vibrational mode as

$$\omega^2 = 2(K_z + K_{zw})sin^2\left(\frac{k_y a}{2}\right) \qquad (17)$$

3. Results and Discussion

The ion flow induced elongation of spherical dust Debye cloud and the formation of attractive wake potential in addition to repulsive Yukawa type of potential pulls the dust grain just below it to displace along the direction of ion flow. Thus, the effective strength of attraction along vertical direction is mainly depends upon the amount of distortion in Debye cloud and relative strength of both repulsive Yukawa and attractive wake potential respectively. From equation (1) it is clearly visible that the dust Debye length λ_{De} around the grain is modified in two different ways: first, by a factor $\frac{1}{\sqrt{1+P}}$ and is attributed to shift in Boltzmanian electron distribution having normalized electron attachment frequency P and second, by a factor $\frac{1}{\sqrt{1+Q}}$ interms of ion flow speed M and normalized ion attachment frequency Q. Both the changes contribute to two different interaction potentials given in equation (12) and (11) respectively. This shows that the modification in dust Debye cloud is caused
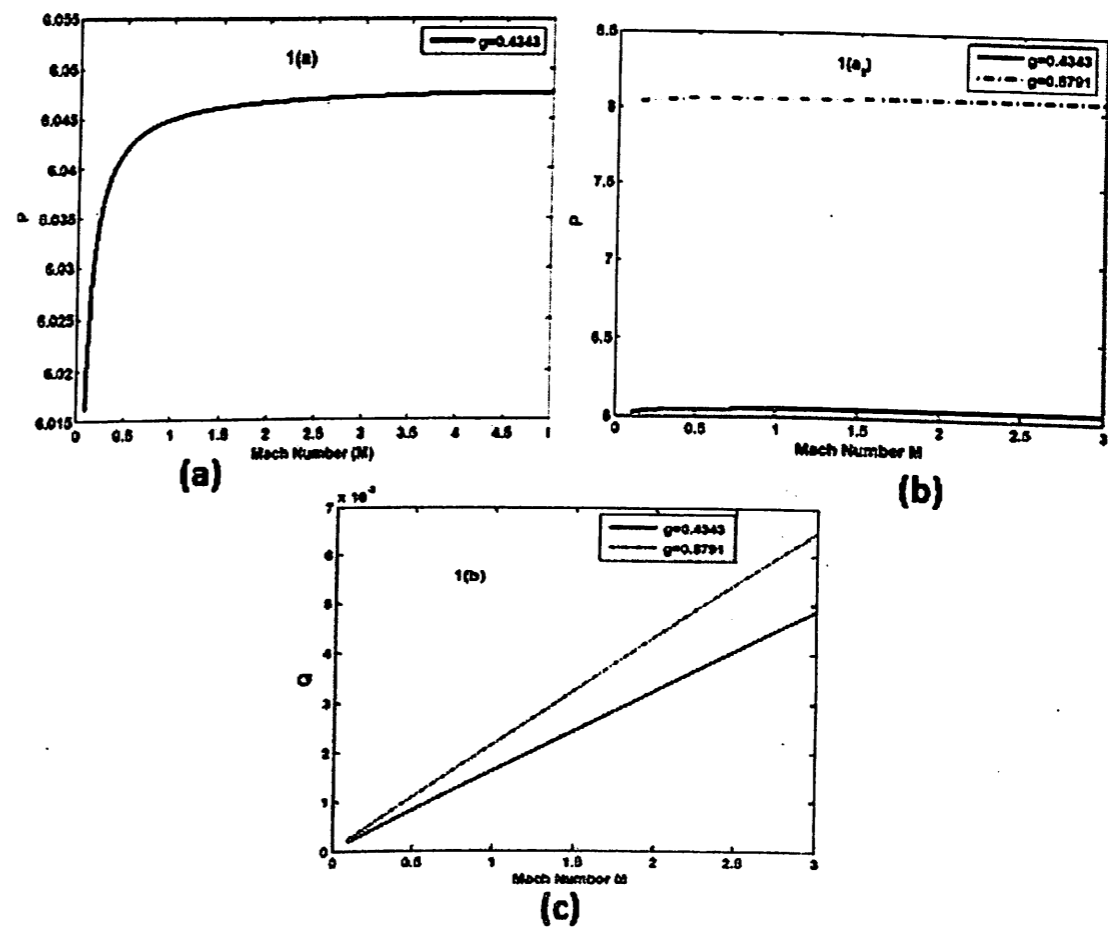
Fig. 3-1. The plot shows (a) the variation of electron attachment frequency P vs. M (Mach number), for a given normalized dust radius g=0.4343. (a₁) P vs. M, for g=0.4343 (red solid) and g=0.5791 (red dash). (c) Ion attachment frequency Q vs. M, for g=0.4343 (red solid), g=0.5791(red dotted).

mainly due to ion flow speed M and background plasma response towards the grain through P and Q. From Fig.3-1, it is seen that P value increases with increase in ion flow speed from subsonic regime and becomes saturated approaching the supersonic regime. This makes the repulsive Yukawa potential independent of M in supersonic regime and can be realized from equation (12).

Whereas, the Q increases linearly with ion flow speed M. As a result, the strength of both repulsive Yukawa and attractive wake potential given in equation (12) and (11) are reduced in presence of dynamical charging of grains as compared to that of constant charged dust grains having P=Q=0 and is shown in Fig.3-2(a) for wakepotential, with typical dust plasma parameters having electron temperature T_e=1.7eV, ion temperature T_i=0.02T_e, ion to electron density ratio $\frac{n_i}{n_e} \approx 1$ and normalised dust radius$g = r_d/\lambda_{De} < 1$. It also clears the fact that for P=0, case having stationary charge on dustsurface, Yukawa potential is completely independent of ion flow speed M. The strength of wake potential from equation (11) shows an enhancement with decrease in flow speed M in Fig.3-2(b).

It is also shown in Fig.3-1 that both the electron (ion) attachment frequency P (Q) increases with increase in grain size g. This says larger grain will have smaller effective Debye length and weaker effective strength of interaction for a given ion flow speed M and is shown in Fig.3-2(c) for a given Γ and k, using equation (16). The corresponding transverse mode of vibration also shows a decrease in frequency of vibration with increase in grain size and is visible from Fig.3-2(d). This transition in coupling strength with grain size finally assures a transition in crystal phase, which is of recent scientific interest in metal nano crystals [18].
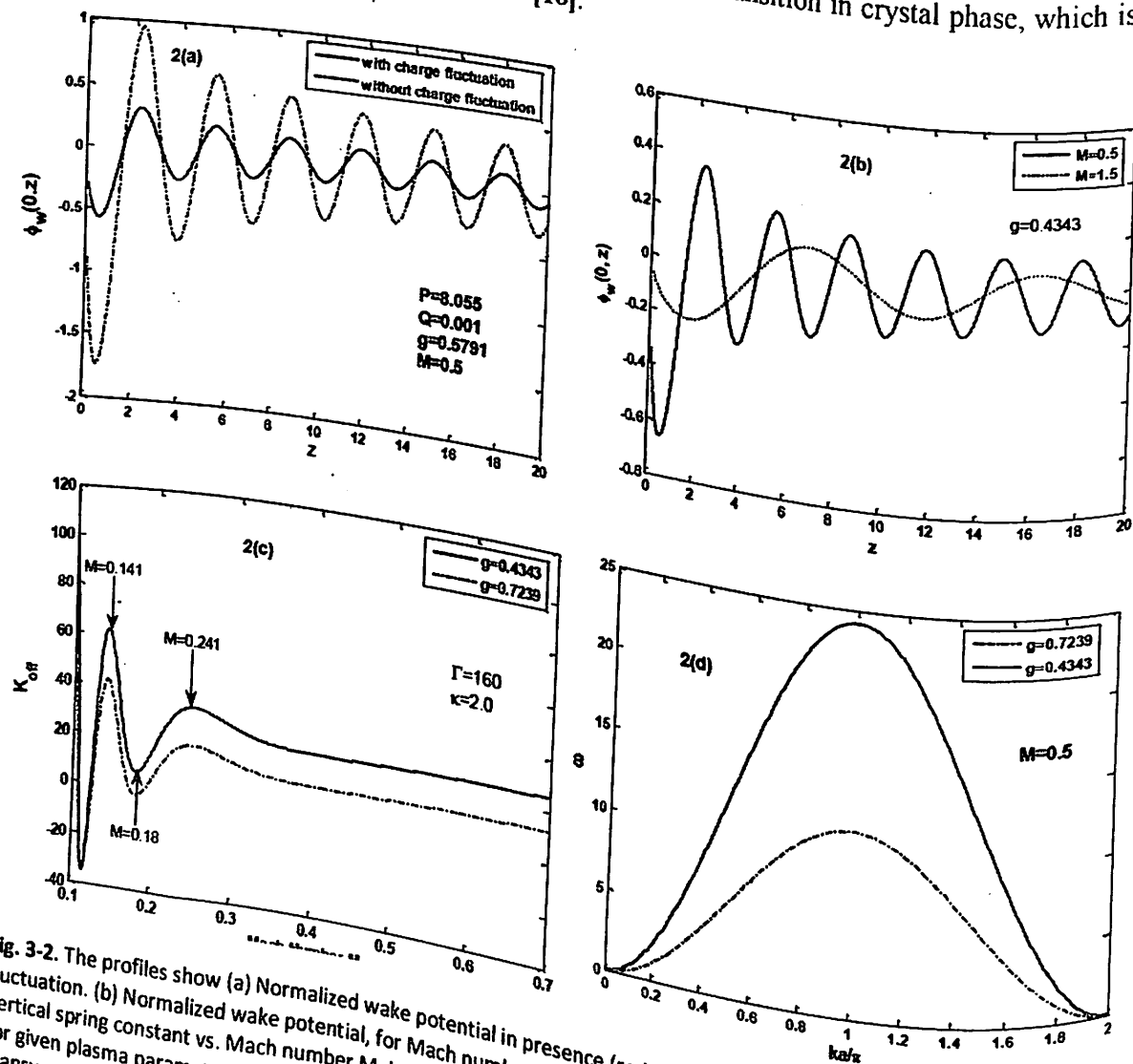
Fig. 3-2. The profiles show (a) Normalized wake potential in presence (red solid) and absence (red dotted) of dust charge fluctuation. (b) Normalized wake potential, for Mach number M=0.5 (red solid) and 1.5 (red dotted). (c) The effective vertical spring constant vs. Mach number M, having normalized grain size g=0.4343 (red solid) and g=0.7239 (red dotted), for given plasma parameters and showing a transition from M=0.241 to M=0.18 to M=0.141. (d) Dispersion relation for transverse vibrational modes having g=0.4343 (red solid), g=0.7239 (red dash) and Mach number M=0.5.

To get an estimation of the relative strength of Wake and Yukawa potential in both sub and supersonic regime, we defined a dimension less ratio $R = \frac{K_{eff}}{K_z}$, where $K_{eff}$is the combinedStrength of Yukawa and Wake potential from equation (16) and $K_z$is the coupling constantfor Yukawa potential from equation (14). The behaviour of relative strength of interaction Rwith subsonic ion ow speed M is plotted in Fig.3-3(a) and is as follows

Subsonic regime (0.1< M < 0.7): The ratio R shows a fluctuation in strength with decrease in M value and is shown in Fig.3-3(a). It is clear from Fig.3-2(b), that particle-wake interaction is dominant in subsonic regime of plasma flow and is also reported in recent experiment [23]. However, the effective confinement strength of particle along vertical direction in presence of both Yukawa and Wake undergo a transition from stronger to weaker and again back to stronger confinement as a characteristic of oscillatory confinement frequency of wake potential with decrease in ion flow speed
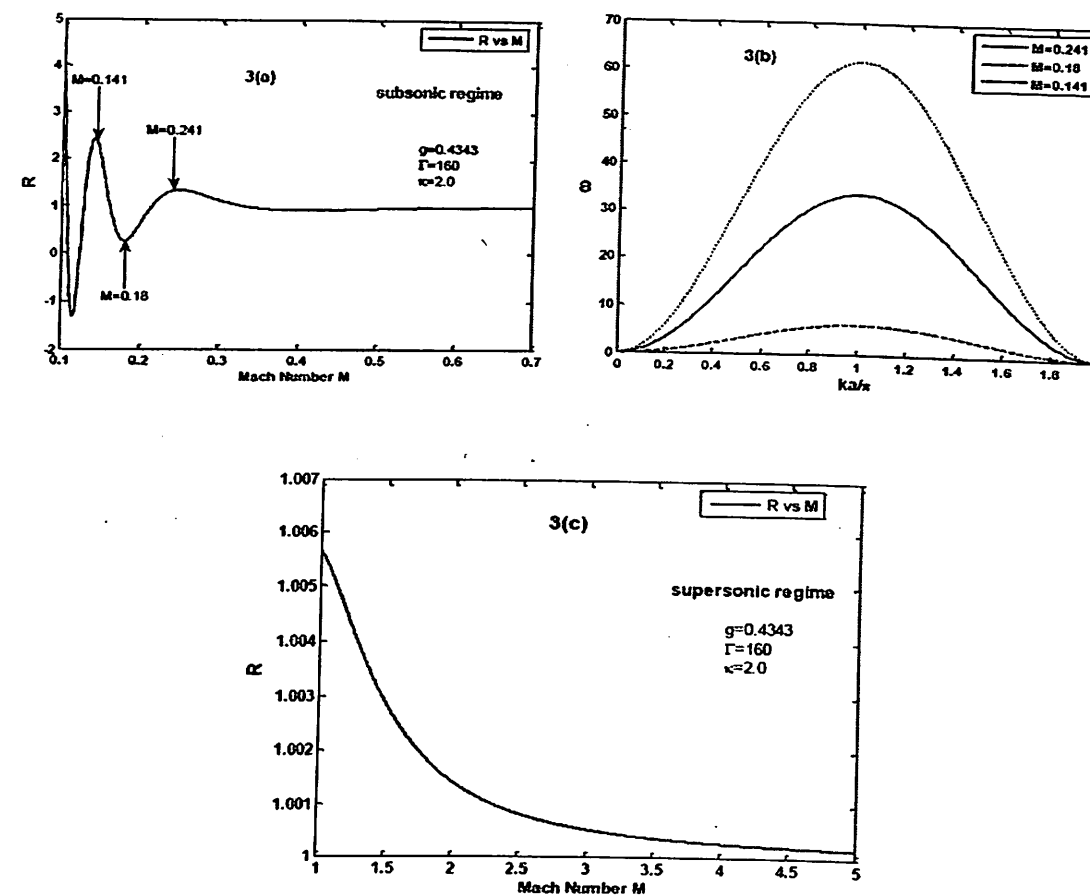
Fig. 3-3. (a) The ratio R vs. Mach Number M, (subsonic regime) for the given set of parameters. (b) The transition in vibrational mode from M=0.241(red solid) to M=0.18 (red dashed) to M=0.141 (red dotted). (c) The ratio R vs. Mach number, (supersonic regime) for the given set of parameters.

M. At M=0.249, the ratio R, shows an enhancement. It implies that the effective interaction is repulsive in nature. On decrease of M at 0.18, the effective coupling is relatively weaker and the interaction becomes attractive in nature. The corresponding mode of vibration also decreases and is shown in Fig.3-3(b). On further decrease, at M=0.141, the ratio R again shows an increment. As a result, the mode increases once again. The behaviour may be realized as such that on gradual decrease in flow speed M, the attractive wake potential of upstream particle starts to dominate and align the lower dust particle along vertical direction of ion flow. On further decrease in M, when the two particle becomes very close to each other, the repulsive Yukawa dominates over there and the particle gets back to its original configuration. The presence of this mixed phase of wake and Yukawa in subsonic regime show an anomalous transition [16] in vibrational mode for given ion flow speeds and is shown in Fig.3-3(b).

Supersonic regime (1.0< M <5.0): In this regime the strength of wake potential is significantly reduced and it makes this region highly Yukawa dominating phase of interaction. It can be seen from Fig.3-3(c), that the ratio R asymptotically approach 1, with increase in ion flow speed M. This is due to the fact that electron attachment frequency P becomes independent of M in supersonic regime and is discussed above. This leads to the strength of Yukawa potential independent of M, for higher ion flow speed.

4. Conclusion

In this letter, we have presented an elaborate discussion on the formation of wake potential along with Yukawa potential in complex plasma and discussed the strength of interaction for a vertically placed dust subsystem, as a characteristic of ion flow speed and grain size. The observations can be summarized as follows:

(a) The effective plasma debye length surrounding the dust gets distorted and reduced in presence of dust charge fluctuation in terms of ion flow speed and particle size.
(b) The strength of both Yukawa and wake potential is reduced with increase in grain size, in terms of electron (ion) attachment frequency P(Q). The corresponding mode of vibration also decreases with increase in grain size. This implies a size dependent transition in crystal phase often observed in nano crystal.
(c) The type of interaction is found to be in a mixed phase of Wake and Yukawa in subsonic regime of plasma flow. In this regime the frequency of vibrational mode shows an anomaly with gradual decrease in ion flow speed M. This implies an ion flow induced anomalous transition in crystal phase, a well known phenomena in solid state physics [17].The supersonic regime is found to be in Yukawa dominating phase.
(d) The study is expected to play a significant role in controlling the phase behaviour and diffusion phenomena in complex plasma in absence of magnetic field.

References

[1] H. Fechting, E. Grun, G. E. Mor_ll, Planet. Space Sci. 27(1979)511.
[2] O. Havnes, C. K. Goertz, G. E. Mor_ll, E. Grun, W.Ip, J. Geophys. Res. 92(1987)2281.
[3] S. Baruah, N. Das, Phys.Plasmas 17 (2010) 073702.
[4] J.H. Chu, I.Lin, Phys.Rev.Lett. 72 (1994)4009.
[5] U. Konopka, G.E. Mor_ll, L. Ratke, Phys. Rev. Lett. 84(2000) 891.
[6] H. Thomas, et al, Phys.Rev. Lett. 73(1994)652.
[7] A. Melzer, V.S. Schweigert, A. Piel, Physica Scripta 61 (2000) 494.
[8] Jie Kong, et al, Phys. Rev. E 84 (2011) 016411.
[9] C. Chia-Ling, I. Chong-Wai, I. Lin, Contrib. Plasma Phys. 49(2009)215.
[10] V. Steinberg, R. Sutterlin, A. V. Ivlev, G. Mor_ll, Phys. Rev. Lett. 86 (2001)4540.
[11] N. N. Rao, P. K. Shukla, M.Y. Yu, Planet. Space Sci. 38 (1990) 4.
[12] D. S. Lemons, M. S. Murillo, W. Daughton and D. Winske, Phys. Plasmas 7 (2000) 6.
[13] O. S. Vaulina, S. A. Khrapak, A. P. Nefedov, and O. F. Petrov, Phys. Rev. E 60 (1999) 5959.
[14] N. Das and K. S. Goswami, Phys. Plasmas 5 (1998) 312.
[15] F. Melandsø, T. Aslaksen and O. Havnes, Planet. Space Sci. 41 (1993) 321.
[16] S. Bhattacharjee, N. Das, Phys. Rev. E 88 (2013) 043106.
[17] Yang-Bo Zhou, et al, J.Chem.Phys.133 (2010) 234703.
[18] R. Bardhan , et al, NatureMater. 12 (2013) 905.
[19] D. Szwarcman, D. Vestler, G. Markovich, ACS Nano 5 (2011)507.
[20] V. E. Fortov , et al, Physics Reports421 (2005) 1.
[21] J. E. Allen, Physica Scripta. 45 (1992) 497.
[22] S. Bhattacharjee, N.Das, Phys. Plasmas 20 (2013)113701.
[23] O. Arp, J. Goree, A. Piel, Phys. Rev. E 85 (2012)046409.

Chapter 4:   Characterization of Ultraviolet Photodetector Based on TiO2 Nano-Particle with Au Schottky Contact

Palash Phukan[*], Rewrewa Narzary, Satyajit Das and Partha Pratim Sahu
Department of Electronics and Communication Engineering, Tezpur University, Napaam, Sonitpur, Assam, India-784028
[*]E.mail: phukan.palash@gmail.in

Abstract

In this work, nanostructured TiO_2 thin film was synthesized using sol-gel process and Metal-Semiconductor-Metal ultraviolet photodetector was fabricated.The chemical and optical properties of TiO_2 thin film were investigated using XRD, SEM, Raman spectroscopy, and UV spectroscopy. The UV photodetector properties were studied by illuminating devices with 370nm UV light source with light intensity of 50 $\mu W/cm^2$ - 150 $\mu W/cm^2$. The detector shows photocurrent of 3.8 μA under light intensity of 150 $\mu W/cm^2$ with 5 volt bias voltage. The fabricated device shows excellent rise time and fall time of 1.9 sec and 3.4 sec respectively. The optical switching characteristics show good reproducibility and stability. The fabricated device has great potential to use in different UV-A detection applications.

Keywords: sol-gel, XRD, SEM, EDX, Raman Spectroscopy, UV-vis spectroscopy.

1. Introduction

Ultraviolet (UV) photodetectors have received considerable attention andare widely used in various military and civil applications, such as secure space-to-space communications, water sterilization, pollution monitoring, fire sensing, etc. [1-3]. Also, exposure to UV light to the human body may cause different types of diseases including cataracts and skin cancer, and even accelerate the aging process [4]. So the detection of UV light is very important. Generally, wideband materials are used as photodetctor material as they have many useful characteristics, such as high electron saturation rates, low permittivity, high breakdown electric-fields, and good thermal conductivity [5]. Many different wide-bandgap materials have been used for UV detection to achieve higher photosensitivity. Many researchers have working on different photosensitive materials such as ZnO, MgO, TiO_2, GaN, ZnS, SiC, MoS_2,Nb_2O_5,Ga_2O_3, NiO, SnO_2, etc.[6-16]. Among the above Titanium dioxide (TiO_2) has drawn increasing attention in many fields such as photocatalysis, solar cells, and gas sensors due to its excellent optical properties and stability [17–20]. Titanium dioxide (TiO_2) is a wide bandgap n-type semiconductor (anatase 3.2 eV and rutile 3.0 eV) [2]. Recently, a variety of TiO_2 based UV photodetectors, such as Schottky barrier photodiodes [21], Hetero-junction photodetector [22], metal-semiconductor-metal (MSM) structure [23], have been reported. Also, TiO_2 thin films can be prepared by different techniques such as sputter depositions, sol-gel process, chemical vapor deposition (CVD), and ion beam-assisted processes [24].

In this investigation, metal-semiconductor-metal (MSM) structure has been used for the fabrication of the device, and sol-gel process is used for the preparation of TiO_2 and the spin coating technique was used for the deposition of TiO_2 thin films. Structural, morphological, and optical properties of obtained layers were studied and well discussed in this work.

2. Experimental methods

2.1. Chemicals

Titanium (IV) Isopropoxide (TTIP), Acetic Acid, and ethanol were purchased from Merck and Sigma-Aldrich. All chemicals were analytical grade.

2.2. Synthesis of TiO_2

Sol-gel process was used for the preparation of TiO_2 nano-particle thin films. Titanium (IV) Isopropoxide (TTIP) as a precursor and ethanol as a solvent for the synthesis of TiO_2. At the beginning, 10 ml of ethanol and 1 ml of deionized water was taken into a beaker stirred for 10 minutes with 1000 rpm. Then, 1 ml of Acetic acid was added to the solution and stirred for another 10 min. Finally, 1 ml of TTIP was added drop wise to the solution. The solution was stirred for another 1 hour at 85°C. Finally, we get a milky white solution.

2.3. Fabrication MSM photodetector

For the fabrication, we used p-type <100> silicon wafer of 10 ohm-cm as a substrate. The schematic illustration of the fabrication process is shown in Fig.4-1. The fabrication process was started with the cleaning of silicon wafer using standard cleaning process (RCA-1 and RCA-2) and dried in an oven for 30 mins at 200°C. 200 nm of Silicon oxide layer was deposited using the thermal oxidation process. The spin coating process was used for the deposition of TiO_2. The prepared TiO_2 solution was deposited uniformly on Si substrates by using spin coating at 1500 rpm. The coated samples were dried at 80°C for 5 minutes. The TiO_2 coated sample was dried at 150°C for 1 hour. Then the prepared samples were calcinated at 500°C for 1 hour. The annealing was done for the formation of uniform nanostructure, which will play a vital role in optical properties of the material. Nano crystalline structure formed during annealing above decrystalization temperature as atoms migrated in crystal lattice. Also, dehydration reaction occurs during the annealing process, which leads to formation of new Ti-O-Ti bonding [25].The gold inter-digited electrode was deposited using thermal evaporation technique and lithography process. Finally, contacts were made using silver
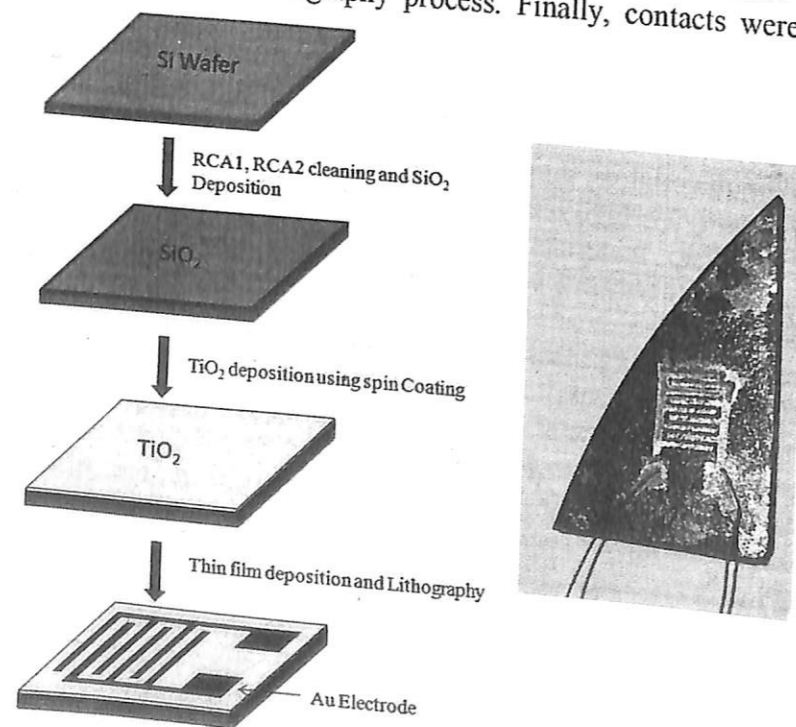
Fig. 4-1. Schematic illustration of the fabrication process of Au/TiO₂/Au MSM photodetector

conductive paste.

2.4. Characterization

The X-ray diffraction (XRD, diffractometer Bruker AXS D8) analyses of samples were conducted to determine the crystalline phase of TiO_2. by Cu-Ka radiation of $\lambda = 1.540598$ A° and 15 mA. Raman spectroscopy is done to investigate the molecule characteristics using Renishaw Basis Series, The SEM analysis was performed using (SEM, JOEL, JSM6390LV) to investigate the surface morphology of the prepared sample.

3. Results and Discussion

3.1. X-ray diffraction (XRD)

The X-ray diffraction (XRD) was performed for analysis of crystalline structure of the material. Fig.4-2(a) shows the XRD pattern of TiO_2 film as synthesized observing no peak in the pattern. So, it concludes that the TiO_2 is amorphous in nature without annealing, which can also be observed in the SEM image. The XRD pattern of the annealed TiO_2 film is shown in Fig.4-2(b). In the pattern, a strong diffraction peak at 25.4° was observed, which confirms the formation of anatase structure of the TiO_2. Also, the TiO_2 anatase peaks of <004>, <200>, <105>, and <211> were observed. The peak at 28° was due to the formation of rutile phase TiO_2. Peaks at the different 2Θ angle of the TiO_2 sample in Fig.4-2(b) confirm the formation of anatase phase. The crystallite size of the TiO_2 was calculated using Scherrer's formula [26]:
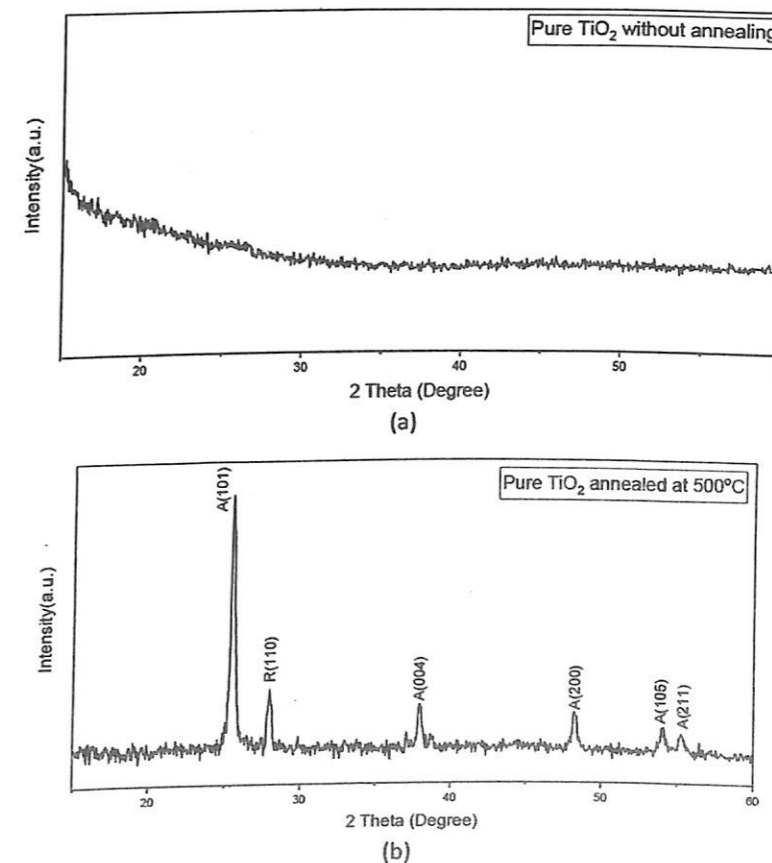
Fig. 4-2. XRD spectra for (a) TiO₂ without annealed and (b) TiO₂ annealed at 500°C

$$D = \frac{k\lambda}{B\cos\theta} \qquad (1)$$

where D is the crystallite size, k is the fixed number 0.9, where $\lambda = 0.71A^\circ$ is the wavelength of Mo Kα X-ray, Θ is the Bragg's angle in degrees, and B is the full width of half maximum (FWHM) of the first peak. The average crystallite size of the prepared sample was found 21 nm, which was also confirmed from the SEM analysis.

3.2. SEM and EDX analysis

The surface morphologies of the semiconducting TiO_2 nanostructure were analyzed using

(a)   (b)
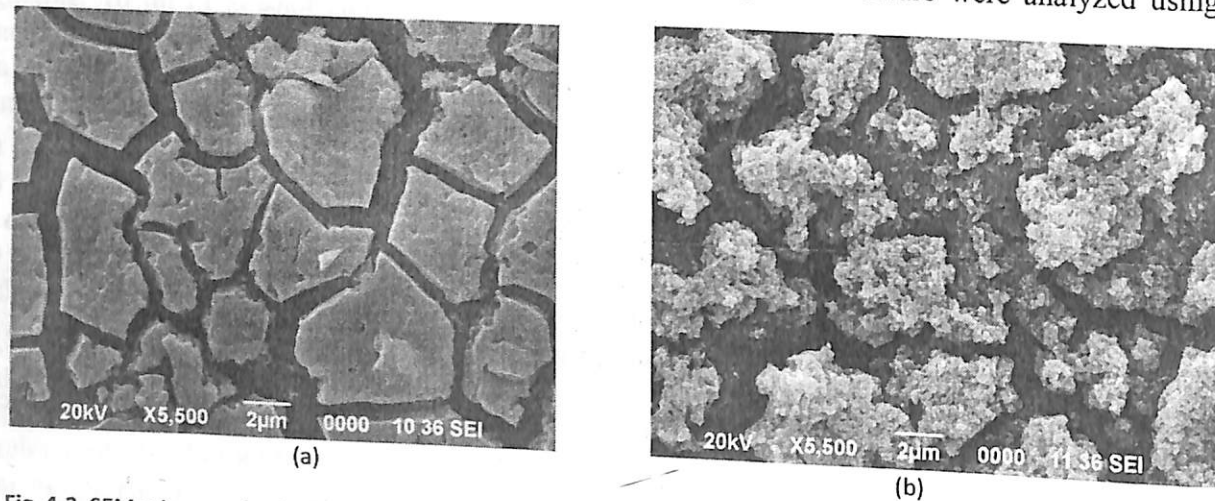
Fig. 4-3. SEM micrograph of TiO_2 samples (a) without annealing and (b) annealed at 500 °C

scanning electron microscopy (SEM). Fig.4-3 shows the scanning electron micro-graph of the synthesized samples. Fig.4-3(a) shows the TiO_2 thin film without annealing and Fig.4-2(b) shows TiO_2 sample after annealing at 500°C. From the SEM analysis, it was evident that the annealing temperature has a significant role in the growth of nanoparticles. No nanoparticles were developed prior to annealing. This virtue can have a significant role in the transportation of electrons and holes to the electrodes and prove to be important in the enhancement of the performance of the devices.

Fig.4-4 shows the EDX analysis of TiO_2. EDX analysis was performed to investigate the percentage of elements present in the prepared samples. Here, the Titanium to oxygen (Ti/O) ratio was found to be 0.15 (Titanium 13.18 weight % and oxygen 86.82 weight %).

3.3. Raman Spectroscopy

Raman spectroscopy was performed for the confirmation of the formation of anatase TiO_2. The Raman spectrum of the synthesized sample was shown in Fig.4-5. A strong peak was found at 159 cm^{-1}, attributing to the E_g of anatase TiO_2. The E_g mode was originated due to the symmetric vibration of O-Ti-O molecule. The other peaks at 393.4 cm^{-1}, 514.3 cm^{-1}, and 635.7 cm^{-1} were attributed to different modes of anatase TiO_2. The peak at 443.5 cm^{-1} confirms the rutile phase of TiO_2. From the Raman spectrum, it was confirmed that the synthesis sample mainly contained anatase TiO_2.

(a)
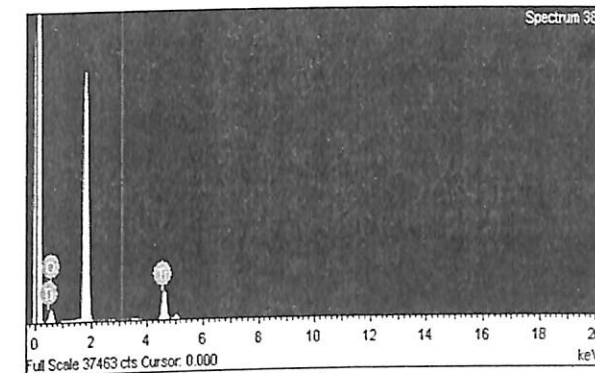
Element	Weight(%)	Atomic(%)
Ti	31.24	13.18
O	68.76	86.82

(b)

Fig. 4-4. (a) EDX spectrum of TiO_2 sample annealed at 500°C and (b) elemental percentage

3.4. UV-vis spectroscopy

UV-Vis spectroscopy was carried out at room temperature using UV–vis spectrophotometer to investigate the optical properties of the prepared thin film of nanostructure. The range of wavelength used for analysis was 200 nm to 800 nm. Fig.4-6(a), shows the absorption spectra of the synthesized thin-film TiO_2 sample. The maximum absorption is found near wavelength of 268 nm. The optical direct band gap of the semiconducting nanostructure was calculated using Tauc's plot by plotting $(\propto h\upsilon)^2$ versus $h\upsilon$ (Fig.4-6(b)). The band is found 3.21eV.

3.5. Characterization of the devices

Current–voltage (J–V) characteristics were investigated both under dark and illumination using 370 nm UV light source with light intensity of 50-150µW/cm^2 having illumination area of 0.25 cm^2, and data were recorded using Keithley 2400 source meter. Fig.4-7(a) shows the current-voltage measurement of the fabricated MSM UV detector under investigation. The device was able to detect very low-intensity UV light. The detector shows a low dark current of 0.52 µA and photocurrent of 2.5µA, 3.4µA, and 3.8 µA under the illumination of 370nm UV light with an intensity of 50 µW/cm2,
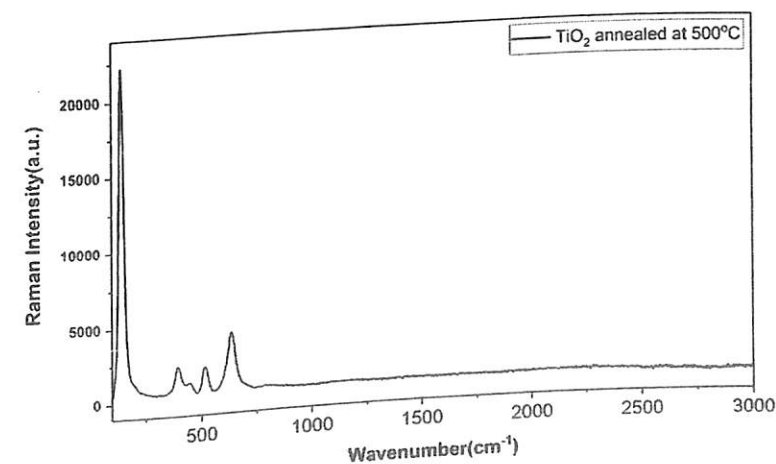
Fig. 4-5. Raman spectra of synthesised TiO_2 sample
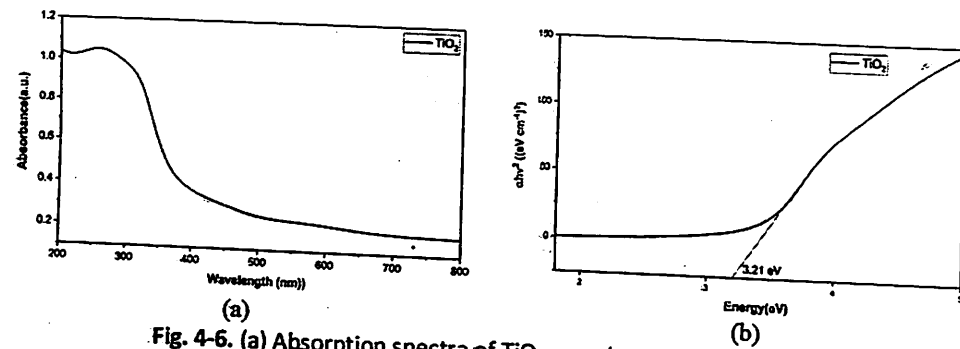
Fig. 4-6. (a) Absorption spectra of TiO2 sample, and (b) Tauc's plot

100 µW/cm2,and 150µW/cm2respectively.

Fig.4-7(b) shows the switching characteristic of fabricated UV detector, where bias voltage was 5 volt under 370 nm UV light source with an intensity of 150µW/cm². The rise time and fall time were measured as 1.9 sec and 3.4 sec respectively.

4. Conclusions

The present work successfully shows a simple and cost-effective process for the synthesis of nanostructured TiO2 thin films, which are very efficient to detect UV light. The chemical, physical,
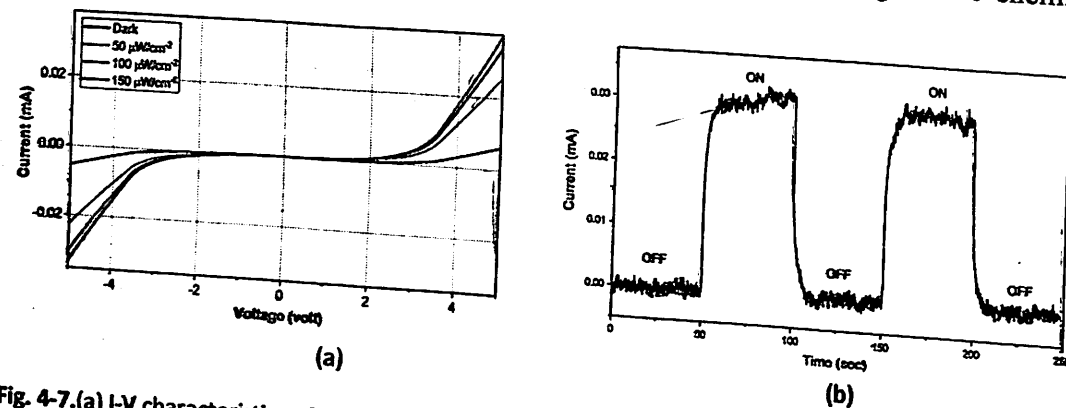
Fig. 4-7.(a) I-V characteristics of Au/TiO2/Au MSM UV detector under dark and UV illumination, and (b)Switching characteristics of the detector

surface morphology and optical properties have been analyzed. XRD analysis indicated characteristic peaks mostly corresponding to the anatase phase of TiO2. SEM analysis was performed to investigate the surface morphology of the TiO2 nanostructure, which shows the amalgamated forms of TiO2 nanoparticles. Au/TiO2/Au metal semiconductor metal UV photodetector was successfully fabricated and investigated. The devices show 3.8 µA of photocurrent under 370 nm light source with light intensity of 150 µW/cm².The fabricated device also shows a good switching time. The device has the potential to detect UV light.

References
[1]   K. Liu, M. Sakurai, M. Aono, Sensor 10 (2010), 8604.
[2]   R. Del Angel, J. C. Durán-Álvarez, R. Zanella, Titanium Dioxide: Material for a Sustainable Environment, 2018.

[3]   Y. Xie, L. Wei, Q. Li, Y. Chen, S. Yan, J. Jiao, G. Liu, L. Mei, Nanotechnology 25 (2014) 075202.
[4]   E. R. Gonzaga, American journal of clinical dermatology 10 (2009) 19.
[5]   Y. Zou, Y. Zhang, Y. Hu, H. Gu, Sensors 18 (2018) 2072.
[6]   Y. Ning, Z. Zhang, F. Teng, X. Fang, Small 14 (2018) 1703754.
[7]   X. H. Xie, Z. Z. Zhang, C. X. Shan, H. Y. Chen, D. Z. Shen, Applied Physics Letters 101 (2012) 081104.
[8]   Y. Xie, et al, Nanotechnology 25 (2014) 075202.
[9]   J. Lahnemann, et al, Nano letters 16 (2016)3260.
[10] X. Fang, et al, Advanced Materials 21 (2009) 2034.
[11] A. Aldalbahi, et al, Scientific reports 6 (2016) 1.
[12] E. Oksenberg, R. Popovitz-Biro, K. Rechav, E. Joselevich, Advanced Materials 27 (2015) 3999.
[13] X. Fang, et al, Advanced Functional Materials 21 (2011) 3907.
[14] W. Y. Kong, et al , Advanced materials 28 (2016) 10725.
[15] A. A. Ahmed, M. Devarajan, N. Afzal, Sensors and Actuators A: Physical 262 (2017) 78.
[16] J. M. Wu, C. H. Kuo, Thin solid films 517 (2009) 3870.
[17] Q. Hongfei, D. Songyan, L. Dabo, W. Jinpeng, Rare Metal Materials and Engineering 46 (2017) 2781.
[18] D. Nunes, et al, Topics in Catalysis 61 (2018) 1591.
[19] H. Zhang, et al, IEEE Electron Device Lett. 33 (2011) 83.
[20] S. Ni, et al, ACS Sustainable Chemistry & Engineering 6 (2018) 7265.
[21] P. Chinnamuthu, et al, Journal of Physics D: Applied Physics 45 (2012) 135102.
[22] D. Y. Zhang, et al, Applied Surface Science 387 (2016) 1162.
[23] H. Ferhati, F. Djeffal, Optik 127 (2016) 7202.
[24] S. Takeda, S. Suzuki, H. Odaka, H. Hosono, Thin solid films 393 (2001) 338.
[25] M. Nakamura, et al, Journal of Materials Research 16 (2001) 621.
[26] A. L. Patterson, Physical Review 56 (1939) 972.

Chapter 5: PERFORMANCE ESTIMATION AND COMPARISON OF CNP BASED INTERDIGITATED ELECTRODES RESISTIVE SENSOR WITH TWO ELECTRODES RESISTIVE SENSOR

Satyajit Das[a,b,*], Palash Phukan[b], Rewrewa Narzary[b], P.P. Sahu[b]

[a]Department of Electronics and Telecommunication Engineering,
Jorhat Institute of Science and Technology, Jorhat, Assam 785010
[b]Department of Electronics and Communication Engineering,
Tezpur University, Tezpur, Assam-784028
E.mail: satyajit.nov7@gmail.com

Abstract

Interdigitated electrodes(IDEs) are widely used sensor structures in the field of biological and chemical sensing. Here in this work, the performance of IDEs resistive sensor structure and normal two electrode resistive sensor has been investigated by observing its change in resistance with a change in the material property like resistivity of the material. The model material here we considered as Ceria nanoparticle (CNP) which changes its material property while interacting with electroactive elements under test. Results show the smaller the values of resistance for the IDEs sensor as compared with the normal one.

Keywords: Interdigitated electrodes, Ceria nanoparticle, Biosensors

1. Introduction

The biosensor comprises a bioactive substance that can specifically detect a species of interest, in intimate contact with a suitable transduction device [1]. Biosensors are advantageous to analytical methodology providing a powerful and often considerably less expensive alternative to well-established laboratory techniques. Biosensors depend on the estimation of currents and/or voltages in detecting the material under test [2].

IDEs based biosensors are one of the most favored sensors, widely utilized in technological applications especially in the field of biological and chemical sensors. It is inexpensive, easy in the fabrication process and has high sensitivity. To detect and analyze a biochemical molecule or analyte, the impedance or capacitance signal needs to be obtained from the sensor's output. The sensors working from the intake of input to getting a sensor's output is shown in fig.5-3. Generally, such sensors have been utilized for detecting capacitance, impedance, dielectric constant and mass conductivity in the biological medium [3].

The interdigital Electrodes based structure includes two parallel coplanar electrodes, with periodical repetition of design (length, width, electrode spacing) [4]. The planar structure enables the examination of material under test (MUT) from only one side, which is especially beneficial when there is a restriction for accessing both sides of the MUT [5, 6]. Here in this study, the sensing material considered for deposition on the substrate is ceria Nanoparticles (CNP). Literature states that the redox-active CNPs acts as antioxidants due to the coexistence of their oxidations states, Ce3+ and Ce4+ [7–11]. The transition between these oxidation states results in the production/obliteration of oxygen vacancies that act as hot spots for actively reacting with electroactive entities [12]. Here, CNPs reacting with electro active chemicals like citrus limonoids will change oxidation states and thereby changes their material property which results in the change in the resistivity of the sensing material. Resistivity change causes resistance to change while applying a voltage across the electrodes.

These sensor structures require the optimization of their structure to maximize the sensitivity of the measurement. In this paper, an interdigitated electrode (IDE) sensor is simulated and compared with a two electrodes sensor structure. This study aims to evaluate the change in resistance of IDEs

and the normal two-electrode structure keeping electrode geometry such as thickness, width, the gap between electrodes, spatial wavelength and sensitive layer thickness same. The fig.5-1 shows a normal two electrode resistive sensor structure with separation between electrodes as G, l is the length of the sensing layer and t is the thickness. The resistance for the structure is given as

$$R_E = \rho \frac{G}{l.t}$$

Or
$$R_E = R_o \frac{G}{l} \tag{1}$$

where R_o is the sheet resistance.

The fig.5-2 shows the repetitive electrode structure of IDE with a sensing layer deposited on top of the IDE structure. Resistance for the IDE structure between electrodes of separation G, width

(a)

(b)
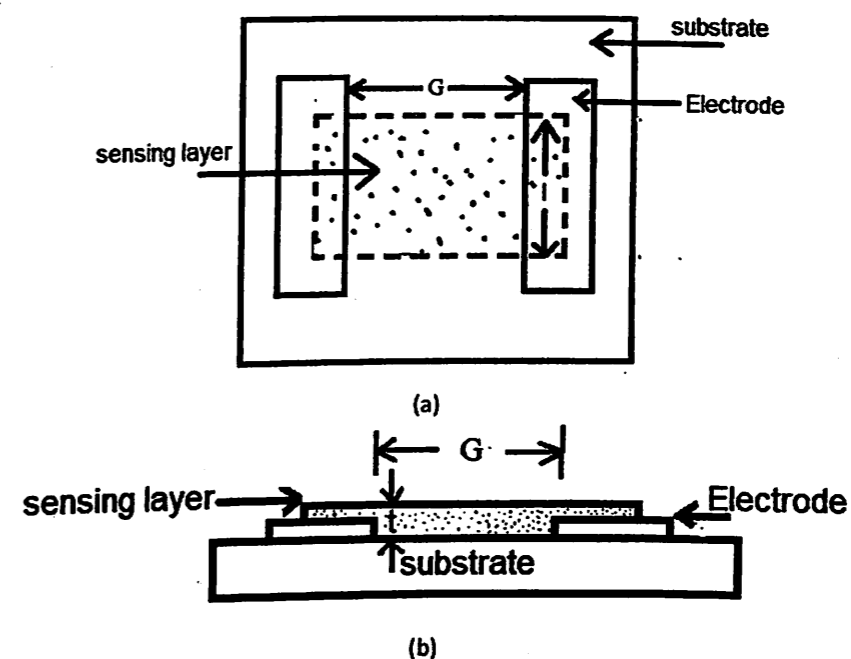
Fig. 5-1. Normal two electrode Resistive sensor a) top view b) side view

W, sensing layer width l and sensing layer thickness t is given as in equation 2.

$$R_{ide} = R_o \frac{G}{(N-1)(l+2.G+W)} \tag{2}$$

where R_o is the sheet resistance that is equal to ρ/t, is the resistivity of the material, N is the number of digits. Then the ratio of the resistance

$$R_E/R_{ide} = (N-1).(l+2.G+W).l \tag{3}$$

2. Methodology

The sensing layer here is considered as Ceria nanoparticle which acts as antioxidants that transit its valence states while reacts with electroactive chemicals. Sensors' sensitivity can be maximized by optimizing the sensor structure. Here in this work geometrical parameters of the sensors are kept as G=W=20 µm, overlapping length l=5mm and number of digits N=8. The electrical resistivity of cerium is approximately 828 nΩ·mOr 828 Ω·nm (at room temperature) as from literature. When sensing material comes in contact with electroactive components its resistivity will change and consequently resistance. The objective is to evaluate the performance of the two types of the sensor while reacting with the electro active components. Simulation has been done using the MATLAB (13 version) tool.
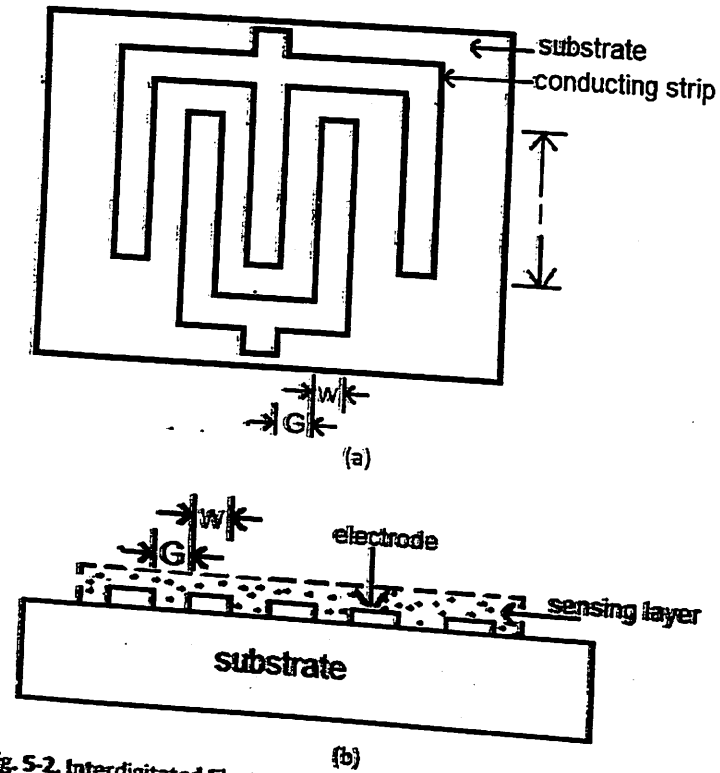
Fig. 5-2. Interdigitated Electrodes resistive sensor a) top view b) side view

3. Results and discussion

Simulation has been done using MATLAB (version 13) for finding the resistance of the IDE sensor and normal two electrode sensor as per the equation (1) and equation(2). The only variable quantity in finding the resistance is the resistivity of the sensing material which changes as it interacts with the material under test. The resistivity of the CNP material has been considered in the range from 0.00000081 Ω.m to 0.0000009 Ω.m. The thickness of the sensing layer has been considered as 10nm, 20nm, 30nm. Resistance for IDE and two electrode structure has shown as 0.457 Ω and 0.324 Ω for t=10nm and resistivity of CNP in 0.00000081 Ω.m as shown in table 5-1. Table 5-2 gives a comparison of resistances for both structures. Results show approximately 7 times less resistance for IDEs compared to the normal structure with the same geometry of electrode structure. The fig.5-4 and
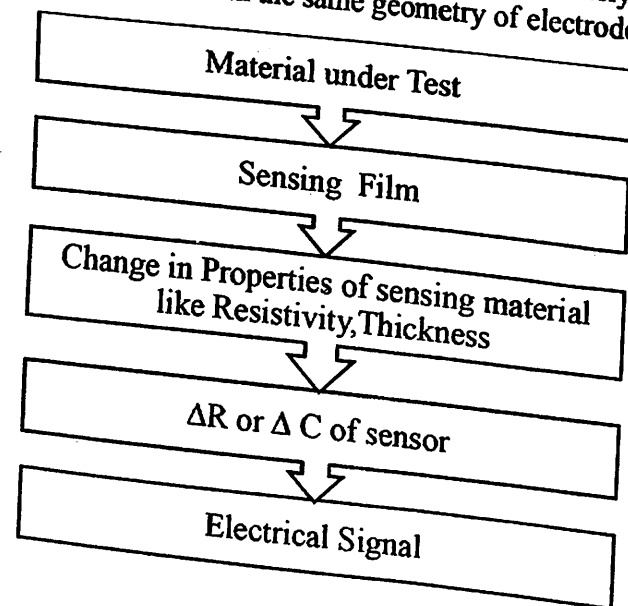
Fig. 5-3. Flow chart for the working of a biosensor
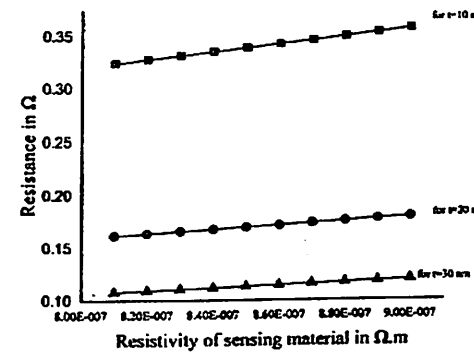
Fig. 5-4. Change in resistance for normal two electrodes resistive sensor with respect to resistivity of material (CNP) for different values of t
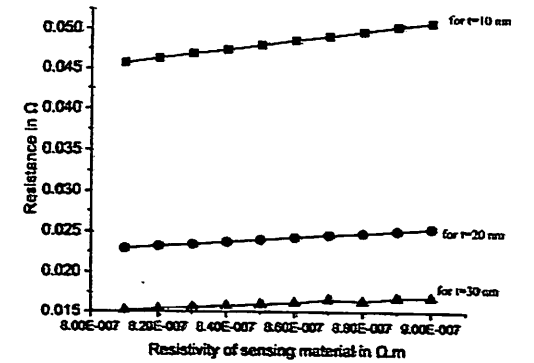
Fig. 5-5. Change in resistance for normal two electrodes resistive sensor with respect to resistivity of material (CNP) for different values of t

fig.5-5 explain nearly step response for the resistance with the increase in resistivity of sensing material in Ω.m.

4. Conclusions

Performance in terms of change in resistance with respect to change in resistivity of the material while interacting with the analyte has been investigated. Results in figures show smaller resistance for IDE structure compared to the other structure keeping all other geometric parameters the same. Interdigitated electrode resistance will decrease with an increase in the number of electrode digits. At AC investigation of interdigital structure, both capacitive and resistive effect needs to be considered. The resistance ratio shows approximately 7 times less resistance for IDEs which is much greater than one without interdigitation. The resistance of the sensor for the same area w.l will be much smaller than that without interdigitization. Consequently, conductivity increases with interdigitization.

Table 5-1.Calculation and comparison of resistance for IDE resistive sensor and normal two electrodes resistive sensor

Sl. no	The resistivity of sensing material in Ω.m	Resistance in Ω for IDE resistive sensor considering N=8			Resistance in Ω for two Electrodes resistive sensor		
		t=10nm	t=20nm	t=30nm	t=10nm	t=20nm	t=30nm
1	0.00000081	0.0457	0.0229	0.0152	0.324	0.162	0.108
2	0.00000082	0.0463	0.0232	0.0154	0.328	0.164	0.1093
3	0.00000083	0.0469	0.0234	0.0156	0.332	0.166	0.1107
4	0.00000084	0.0474	0.0237	0.0158	0.336	0.168	0.112
5	0.00000085	0.048	0.024	0.016	0.34	0.17	0.1133
6	0.00000086	0.0486	0.0243	0.0162	0.344	0.172	0.1147
7	0.00000087	0.0491	0.0246	0.0166	0.348	0.174	0.116
8	0.00000088	0.0497	0.0248	0.0164	0.352	0.176	0.1173
9	0.00000089	0.0503	0.0251	0.0168	0.356	0.178	0.1187
10	0.0000009	0.0508	0.0254	0.0169	0.36	0.18	0.12

Table 5-2. Calculation for the ratio of resistance for IDE resistive sensor and normal two electrode resistive sensor

Sl no	The resistivity of sensing material in $\Omega.m$	The ratio RE/Ride		
		t=10nm	t=20nm	t=30nm
1	0.00000081	7.08972	7.07424	7.10526
2	0.00000082	7.08423	7.06897	7.0974
3	0.00000083	7.07889	7.09402	7.09615
4	0.00000084	7.08861	7.08861	7.08861
5	0.00000085	7.08333	7.08333	7.08125
6	0.00000086	7.07819	7.07819	7.08025
7	0.00000087	7.08758	7.07317	6.98795
8	0.00000088	7.08249	7.09677	7.15244
9	0.00000089	7.07753	7.09163	7.06548
10	0.0000009	7.08661	7.08661	7.10059

References:

[1] F. Jane, E. H. A. O. Hill, Anal. Chem. 15 (1987) 933A-944A.

[2] J. S. Daniels, N. Pourmand, An International Journal Devoted to Fundamental and Practical Aspects of Electroanalysis. 19 (2007) 1239-57.

[3] P. Geng, et al, Electrochim. Acta. 53 (2008) 4663-68.

[4] R. Igreja, C. J. Dias, Sens. Actuators A Phys. 112 (2004) 291-301.

[5] X. Hu, W. Yang, Sens. Rev. (2010) 26.

[6] A. V. Mamishev, et al, Interdigital sens. Transd. Proceed. IEEE. 92 (2004) 808-45.

[7] A. Gupta, S. Das, C. J. Neal, S. Seal, J. Mater. Chem. B. 4 (2016) 3195-202.

[8] A. S. Karakoti, et al, Jom. 60 (2008) 33-7.

[9] C. Korsvik, S. Patil, S. Seal, W. T. Self, Chem. commun. 10 (2007) 1056-8.

[10] H. J. Kwon, et al, ACS nano. 10(2016)2860-70.

[11] G. Pulido-Reyes, et al, Sci. Rep. 5 (2015) 1-4.

[12] N. Saraf, et al, Sens. Actuators B Chem. 283 (2019) 724-30.

Chapter 6: ELECTRICAL PROPERTIES OF NATURAL FIBRES REINFORCED COMPOSITES: A REVIEW

Parvind Kr. Sahu

Department of Physics, Digboi College, Digboi -786171, Assam
E-mail: parvind15011992@gmail.com

Abstract

Natural plant fibers and their composites have received considerable attentions over synthetic fibers due to their important aspects of biocompatibility, possible biodegradation, non-toxicity and abundance. Composites of natural fibres have got wider range of applications in manufacture of automobile parts, construction materials and electrical appliances. For electrical application selection is required on the basis of evaluation of electrical property parameters. Keeping this in view an effort has been made to survey the recent research works on electrical resistivity of natural fibre reinforced composites. The studies show that moister absorptions plays an important role in electrical properties of natural fibre composites.

Keywords: Natural fibre composites, Electrical properties, Moisture absorption

1. Introduction

Natural Fibres are hair-like materials that may be continuous or discrete elongated pieces, which can be obtained from plants and spun into filaments, thread, or rope. Plant fibres of jute, banana, bamboo, hemp, sisal, flax, abaca, broom, coir, elephant grass, kenaf, Linseed, oil palm fruit , rice husk etc. are commonly used in making natural fibre composites. Researchers are continuously working to improve natural fibres and their composites to support their potential across a wider range of application in constructions and buildings, railway coaches, marine, military, sports, packaging industries aerospace and automotive.

Natural fibres have not only got application in mechanical engineering but in electrical application too. They can be used as insulators in electronic devices, for shielding the cables etc. electrical, physical and mechanical properties play a very important role in making wires and cables. Electrical properties include dielectric constant, dielectric strength, impedence factor etc. Dielectric strength means ability of the material to withstand with the voltage without breakdown. Dielectric constant of natural fibre composite mainly depends upon the dipole interaction present and orientation effect. Lower the value of dielectric constant, insulator will be more efficient. But as there is moisture absorption in natural fibres, so conductivity of fiber increases and hence dielectric constant of fiber increases and its insulating property decreases. So in order to minimize this problem fibers are usually treated with chemicals. Physical properties mean specific gravity, temperature rating etc. Specific gravity is the comparison of density of composite with water. It depends upon the density of material and hence lower density materials are always preferred. Temperature rating means the range of temperature within that material can be used without degradation. Wider temperature range is always better for electrical application. Mechanical properties include elongation, tensile strength, flexibility etc. Elongation is the property of material which defines how much a material can be stretched without breaking. Those composite fibers which have good flexibility can be rolled or coiled easily without any physical damage. Flammability is another important property which means the temperature at which wire catches fire (industrial standards are applied) should be considered for the electrical application of the natural fibres.

2. Literature survey

Electric properties of pineapple reinforced polyethylene composites have been studied by Jayamol et. al. [1] and they observed that the increase in the dicletric constant of composite with fiber loading was due to increased orientation and interfacial polarization. The electric properties of sisal fiber reinforced composite showed that the composite has electric anisotropic behavior [2]. Joseph et al. [3] have observed that in banana fiber composites, at low frequencies, dielectric loss factor increased with increase in fiber loading and also found that In hybrid composites, the dielectric constant decreases with increase in glass fiber content. This was due to hydrophobic nature of glass fiber while banana fiber in hydrophilic. Treatment with silane, NaOH, latex, heat and acetylation has decreased the dielectric constant value. Andrej K.B. et. al. [4] studied the effect of acetylation of the fibre on the basis of moisture resistance and dielectric properties of the resulting composites and observed It was found that the moisture absorption and swelling properties of the composites were reduced respectively by 60% and 30% due to acetylation. Elammaran Jayamania et. al. [5] made a comparative study of dielectric properties of hybrid natural fiber composites, and found that dissipation factor decrease with an increase in the frequency. J. B. Naik and S. Mishra [6] prepared composites of banana, hemp, and agave with HDPE resin in different ratios, 60:40, 55:45, 50:50, and 45:55 (wt/wt) and these fibers were also treated with maleic anhydride and the effect of maleic anhydride was studied on surface resistivity and volume resistivity of wood polymer composites. They found that the surface resistivity decreases with an increase in fiber content in the composites, while volume resistivity increases. The maximum surface and volume resistivities were observed in untreated banana fiber composite, while minimum surface resistivity and volume resistivity were found in maleic anhydride-treated agave fiber composite. D.s Pramila Devi et. al. [7] report the characterization and properties of conductive elastomeric composites of polypyrrole (PPy) and PPy coated short Nylon-6 fiber (F-PPy) based on natural rubber (NR) prepared by in situ polymerization method. PPy/NR blends were prepared by polymerizing pyrrole in NR latex using anhydrous ferric chloride as oxidizing agent, p-toluene sulphonic acid as dopant and vulcastab VL as stabilizer. Comparing The electric properties of sisal fiber reinforced low density polyethylene composite have been with that of carbon black and glass fiber filled low density polyethylene composite it is found that dielectric constant increased steadily with increasing fiber content for all frequencies in the range of 1to 107 Hz [8-11]. They observed that dielectric constant decreased with increase of fiber length and frequency. It was also noted the effect of surface treatment on the electric properties of low density polyethylene composite reinforced with short sisal fibers with alkali, steric acid, peroxide, acetylation and permanganate treatment the dielectric strength of composite materials decreased due to decrease in hydrophilic nature of the composite. Jayamani et al.[28] analysed the effect of alkali treatment on electric properties of four types of fabricated bio composites. The values of dielectric constants of treated fibre composites were lower than that of the untreated ones. This may be owing to the decrease in orientation polarisation of the composites made of treated fibres. Yan et. al [12] reported that sisal/ low density polyethylene composites containing 5% carbon black can be used in antistatic applications to dissipate static charge. It is essential to study the effect of interfaces on the change carrier generation, transport and storage in polymeric system because polymeric interfaces act as charge carrier generation sites [13].In determining the dielectric behavior physical structure of polymer composites in the solid or viscoelectric state is of great importance [14]. Elammaran Jayamani et al.[28] made comparative studies of dielectric properties such as the dielectric constant, the dissipation and loss factor of four different types of composites made of lignocellulosic fibers with respect of fiber loading and alkali treatment and found that the dielectric constant, dissipation factor and loss factor progressively increases with increase in fiber loading and decreases with an increase in frequency. Kakar et al.[31] prepared luffa polylactide quadratic splint composites (LNFC) and studied dielectric behavior of LNFC. They found greater dielectric constants upon increasing the fiber volume fraction; for instance, the addition of heat-treated Luffa fibers into a Polylactic acid matrix exhibited higher dielectric constants compared to pure polylactide (PLA) at all applied frequencies, yet increasing the frequency decreased the dielectric constants. Based on epoxy resin with polyaniline-DBSA fillers W. Jia et al. analysed electrical conductivity of composites [16]. Composite material was made of using conductive filler PANI-DBSA in form of powder and paste in matrix polymer

bisphenol, an epoxy resin, anhydride hardener and an accelerator and graph was plotted for variation of electrical resistivity which is the inverse of electrical conductivity with content of PANI powder. It was observed that With 40% wt./wt. of filler content electrical conductivity of the order of 10-8 ohm-cm was observed which gradually increases or the resistivity gradually decreases as the wt. % of filler material increases. M.M. Pavlović et al.[17] studied electrical conductivity of lignocellulose composites loaded with electrodeposited copper powders at different pressures and stated that the electrical conductivity of the composites is < 10-15 MS/m, unless the metal content reaches the percolation threshold of 14.4% (v/v), beyond which the conductivity increases markedly. Choh et al. [29] prepared oil palm empty fruit bunch (OPEFB) fiber composites by melt blending and compression molded into sheets and found that the electrical conductivity of the composites decreased with increasing OPEFB fiber content. Inspite of slight decrease in conductivity, the composites still were sufficiently conductive relative to applications such as sensors and electromagnetic shielding after the fiber addition. Recently, Garip Gencet al.[30] prepared a green fiber-reinforced PCB laminate using plant-based fiber as reinforcement and found that the electrical resistivity values (both surface and volume resistivity) of this Luffa-PCB were higher than FR2 and FR4 type PCB laminates. Hence luffa fiber has a better insulation effect.

3. Discussion

The various factors on which resistivity on the natural fiber composite depends are moisture content, crystalline and amorphous component present, presence of impurities, chemical composition, cellular structure, microfibrillar angle etc. Fibers and flakes having elongated shapes affect the electrical conductivity [15]. Dielectric constant of natural composite depends on orientation and interfacial polarisation of fibres and matrix. Due to moisture absorption conductivity of fiber increases and hence dielectric constant of fiber increases and its insulating property decreases. Treating the natural fibers with alkaline solution or with coupling agents' moisture absorption problem can be reduced. Fibers treated with alkaline or acidic solution, prevents the establishment of hydroxyl groups on the filler surface and functional groups resulting in reduction of moister content. The dielectric constant of material depends upon the polarizability of the material. The resistivity of fiber reinforced composites depends on the moisture content, crystalline and amorphous component present, presence of impurities, chemical composition, and cellular structure. The electrical conductivity increases as the natural fiber content in the fiber increases beyond percolation threshold value. Dielectric loss factor is measure of loss of energy in a dielectric material through conduction, slow polarization of currents and other dissipative phenomena. NaOH treatment decreases the dielectric loss factor. With the increase of frequency at fixed temperature dielectric loss factor decreases and the loss peaks were observed at about 1 kHz at high temperature in composite materials, which may be due to the temperature glass transition in polyester [26]. The absorbed moisture in the composite materials at the fiber resin interface acts as a politicizing agent for the polymer and as a result increases the mobility of the polymer chain and hence brings the loss peak due to temperature glass transition of polyester at higher frequency value [27]. Joseph et al. have observed that at low frequencies, in banana fiber composites, dielectric loss factor increases with increase in fiber loading. They also found that at high frequency, a reverse behavior occurs which was due to the polarization of the fibers at low frequencies and at higher frequencies it was absent. The dielectric loss factor increased with increasing temperature. At lower frequencies dielectric loss due to chain motion of polymer is more effective due to glass transition temperature of the polymer and at higher frequencies, the dielectric loss factor is low which remained more or less constant with increasing temperature because the orientation polarization due to chain motion of polymer cannot keep phase with the rapidly oscillating electric field. It is observed that dielectric constant, dissipation factor and loss factor depends on fiber loading and frequency. They increase with fiber loading and decrease with increase in frequency. In LNFC dielctric constant increases with increase in fibre-volume fraction and with increasing frequency, dielectric constant decreases due to the interfacial polarization produced between the dipoles of the matrix and fibers [31]. Analysis of electrical conductivity based on polyaniline-DBSA fillers in composite fibers tell that electrical conductivity increases with increases in filler content in composites. In study of oil palm empty fruit bunch (OPEFB) fiber composites it is found that

electrical conductivity of the composites decreased with increasing OPEFB fiber content signifying that OPEFB has good insulation property [29]. Study of surface and volume resistivity of Luffa fibre reinforced PCB laminates showed that they have better insulation effect as compared to FR2 and FR4 PCB laminates and so they can replace them [30].

4. Conclusions:

The regular plastic material which was used for making electrical insulators are less dense compared to the natural fiber and so by reinforcing natural fiber, density of the material increases with considerable increase in strength. Fiber loading and fiber treatment not only alters mechanical but electrical properties like dielectric constant and dissipation factors. With higher fiber loading dielectric constant of the fiber decreases, but due to moisture absorption dielectric constant increases and tensile strength decreases. Moisture absorption can be reduced by fiber treatments. It has been observed that dielectric dissipation factor increased with temperature and decreased with frequency. Also dielectric loss decreased with the increase of frequency at fixed temperature Natural fiber reinforced composites can be used not only in mechanical engineering applications but also in electrical applications with certain modifications.

References:

[1] G. Jayamol, S. S. Bhagwan,S. Thomas, J. Polm. Eng. 17 (1997) 5.
[2] N. Chand, D. Jain, Compos. A. 36 (2005) 594.
[3] S. Joseph, S. Thomas, J. Appl. Poly. Sci. 109(2008) 256.
[4] K. B. Andrej, L. Marta, Bioresources. 4 (2009) 111-126.
[5] E. Jayamania, S. Hamdanb, Proced. Eng. 97 (2014) 536 – 544.
[6] P. A. Sreekumar, J. M. Saiter, K. Joseph, Composites Part A: Appl. Sci. Manufact. 43 (2012) 507-511.
[7] D. S. Pramila Devi, et al, Mater. Design 43 (2013) 337–34
[8] S. Paul, J. Thomas, Appl. Poly. Sci. 63 (1997) 247.
[9] G. Kulkarni, K. G. Satyanarayana,P. K. Rohatgi, J. Mater. Sci. 16 (1981) 1719.
[10] Paul, K. Joseph,S. Thomas, Compos. Sci. Technol. 57(1997) 67.
[11] Paul, S. Thomas, C. Pavitharan, J. Appl. Polm. Sci. 63 (1997) 247.
[12] L. Yan, W. M. Yiu,Y. E. Lin, Compos. Sci. Technol. 60 (2000) 2037.
[13] K. Tripathi, P. K. C. Pillai, Proceeding of the 5th International Symposium on Electrets, Heidelber IEEE, New York, (1985).
[14] L. Aras, M. Baysal, J. Polym Sci. Polym. Phys. Edn. 22 (1984) 1453.
[15] R. Blythe, Electrical properties of polymer, Cambridge University Press Cambridge, London, (1979)
[16] W. Jia, R. Tchoudakov, E. Segal, R. Joseph, M. Narkis, A. Siegman, Synth. Met. 132 (2003) 269-278.
[17] M. M. Pavlovic, et al,Int. J. Electrochem. Sci. 6 (2011) 3812 – 3829.
[18] G. M. Virginia, P. V. G. Silvab, T. Daniel, Materials Research. 14(2011) 360-365.
[19] M. Akram, A. Javed,T. Z. Rizvi, Turk. J Phys. 29 (2005)355.
[20] E. Polac, Epolac Technical data Bulletin, Nippon Shokubai Kaguku, Kogyo, Co. Ltd, Japan, (1985).
[21] M. S. Sreekala, Ph.D. Thesis, Mahatma Gandhi University, Kottayam, Kerla, India, (2000)
[22] R. Blythe, Electrical properties of polymer, Cambridge University Press Cambridge, London, (1979)
[23] P. Smyth, Dielectric behavior and structure, McGraw Hill Oxford, (1956).
[24] H. Frohlick, Theory of Dielectrics, Oxford University Press Oxford, (1956).
[25] K. S. Moon, S. Liong, H. Li, C. P. Wong, J. Electron. Mater.33 (2004) 1381-1388.
[26] Mateen, PhD Thesis, Centre for Solid State Physics, University of Punjab, Lahore, Pakistan, (1983).

[27] E. Polac, Epolac Technical data Bulletin, Nippon Shokubai Kaguku, Kogyo, Co. Ltd, Japan, (1985).
[28] E. Jayamani, S. Hamdan, M. R. Rahman, Mater. Today. Proc. 2 (2015) 2757–266.
[29] J. L. Choh, Y. C. Ching, S. N. Gan, S. Rozali, S. Julai, BioRes. 11 (2016) 913-928.
[30] G. Genc, A. Sarikas, U. Kesen, S. Aydin, IEEE Trans. Compon. Packag. Manuf. Technol. 10 (2020) 933–940.
[31] Kakar, E.Jayamani, K. H. Soon, M. K. B. Bakri, J. Vinyl. Addit. Technol. 24 (2018) 388–394.

Chapter 7: AN EFFICIENT AND LOW-COST METHODOLOGY FOR THE FABRICATION OF ZnO/p-SILICÓN HETEROSTRUCTURE FOR APPLICATION IN HETEROJUNCTION SOLAR CELLS

Rewrewa Narzary*, Palash Phukan, Satyajit Das, and Partha Pratim Sahu

Department of Electronics & Communication Engineering, Tezpur University, India
E.mail: rewa325@tezu.ernet.in

Abstract

This work reports a simple, efficient and low-cost methodology for the fabrication of ZnO/p-Si heterostructure for application in optoelectronic applications. ZnO nanostructure could be successfully grown on silicon substrate employing a sol-gel approach. The importance of annealing temperature for the successful growth of crystalline nanostructure has been highlighted. The XRD result revealed the formation of a highly ordered crystalline phase of prepared semiconducting zinc oxide. The UV-vis spectroscopy analysis revealed that the zinc oxide nanostructure exhibited a transmittance of above 80 % in the visible spectrum. The optical bandgap was estimated using Taucs' plot and found to be 3.27 eV.

Keywords: low-cost, ZnO nanostructure, ZnO/p-Si heterostructure, heterojunction solar cell

1. Introduction

In the last decades, the development of first-generation p-n junction based on crystalline solar cell has dominated the photovoltaic market due to the high photoconversion efficiency and long lifetime over other technologies [1]. However, the fabrication techniques demand inherent pitfalls, including a very high-temperature diffusion process and the use of potentially harmful chemicals. Therefore, the research community is motivated for the development of more efficient solar cells incorporating various device structures, cost-effectiveness, and eco-friendly fabrication methodologies.

During the past decade, researchers have been continuously working for the development of high-performance, and cost-effective materials and fabrication processes. The new device structure based on heterojunction of silicon with transparent conducting oxides (TCO) such as zinc oxides, graphene oxides/reduced graphene oxides, titanium oxides, etc has gained the attention of the research community for the development of high-performance low-cost heterojunction photovoltaics [2-5]. ZnO, SnO2, TiO2, CuO, and GO/rGO are the potential semiconducting materials used in various optoelectronic devices [6-11]. Among these materials, semiconducting wide-bandgap zinc oxide nanostructure has attracted much attention due to having excellent photosensitivity, high exciton energy (~60eV), low resistivity, wide bandgap (Eg=3.37eV at 300K), stability, availability, low cost, non-toxic, and its remarkable optoelectronic properties[12, 13]. Undopedzinc oxide is an important TCO, naturally n-type attributed to native defects such as oxygen deficiencies and excess zinc. These important properties can play a pivotal role in the development of low-cost optoelectronic devices. It has potential applications in various electronic and optoelectronic devices including photodetector, photocatalyst, piezoelectric sensors, nanoelectromechanical systems (NEMs), and energy harvesting applications [6, 7, 14]. These structures can enhance the aspect ratio by the formation of nanostructures, a desirable factor for efficiency enhancement of solar cells. Zinc oxide nanostructures can be grown on silicon substrates by various classical, physical, and chemical methods, ranging from chemical vapour deposition (CVD), sputtering [15], atomic layer deposition (ALD)[16], pulsed laser deposition (PLD) [17]chemical spray pyrolysis (CSP), and oxidation of zinc nanoparticles [18].

Aqab.et.al [16], reported on the fabrication of aluminium doped heterojunction solar cell employing a combination of low-pressure CVD and ALD, achieving a power conversion efficiency (PCE) of 0.46 %, corresponding to a short circuit current density (J_{sc}) of 19.12 mA/cm^2, the open-circuit voltage of 67 mV, and a fill factor (FF) of 35.70 %. Shen.et.al [15], reported on ZnO/p-Si heterojunction solar cell using DC magnetron sputtering and achieved a PCE of 1.14 %, corresponding to J_{sc} = 17.27 mA/cm^2, V_{oc} = 400 mV, and FF = 16.50 %. Pietruzzka.et.al [19], reported on ZnO-MgO/p-Si solar cells by varying the concentration of magnesium. Though a PCE of 6 % could be achieved, the fabrication methodology requires multiple processing steps such as doping of zinc oxide and ALD, and double-layer; aluminium doped zinc oxide (AZO) and $Zn_{(1-x)}$-Mg$_x$O. In other work [20], Pietruszka and his team could achieve a PCE of 10.6 %, but similarly, the fabrication technique becomes complex and multiple processing steps such as texturing of silicon, hydrothermal process, ALD, and even doping of zinc oxide. In the process, potentially environmentally hazardous chemicals such as nitric acid (HNO$_3$) and hydrofluoric acid (HF) is also used. Similarly, several researchers have reported on heterojunction solar cell employing a combination of complex and multiple processing steps, use of multiple layers, and doping of zinc oxides [21-23]. Among the various methods available, sol-gel process is highly appealing due to the simplicity in film deposition, low processing temperature, and requirement of simple equipment, low expenses, and simple fabrication methodology, motivating the research community with limited laboratory facilities.

In this direction, we demonstrate an efficient, simple, and cost-effective methodology for the fabrication of ZnO/p-Si heterostructure to be used in heterojunction solar cell. The sol-gel prepared zinc oxide solution was spin-coated on the p-silicon. Further, to study the effect of annealing temperature on the growth of zinc oxide nanostructures the sample was annealed at 400 °C. The crystal phase and orientation, surface morphology, elemental composition, and optoelectronic properties of the samples were investigated using various characterization techniques such as X-ray diffraction analysis (XRD), scanning electron microscopy (SEM/EDX), UV-vis spectroscopy.

2. Experimental

2.1. Synthesis of zinc oxide nanostructure

Synthesis or preparation of semiconducting zinc oxides (ZnO) exhibits a variety of morphology, such as nanorods, nanofibers, nanowires, hollow spheres, nanosheets, nanoflowers, and nanoparticles, depending on various proportions of oxidants, dopants, synthesis conditions, and methods of synthesis. We have employed a simple, efficient, and low-cost methodology for the preparation of ZnO/p-Si heterostructure. Typically, zinc acetate dihydrate (Zn(CH$_3$COO)$_2$·2H$_2$O, polyvinyl alcohol (PVA), and sodium hydroxide (NaOH) were used as the precursors. The methodology consisted of, preparation of the solutions; cleaning of the substrates, deposition of the prepared ZnO solution onto the substrates using spin coating and subsequently annealing of the samples for the growth of ZnO nanorods and the formation of the heterostructure. The whole methodology is depicted in the form of flowchart as shown in Fig.7-1.
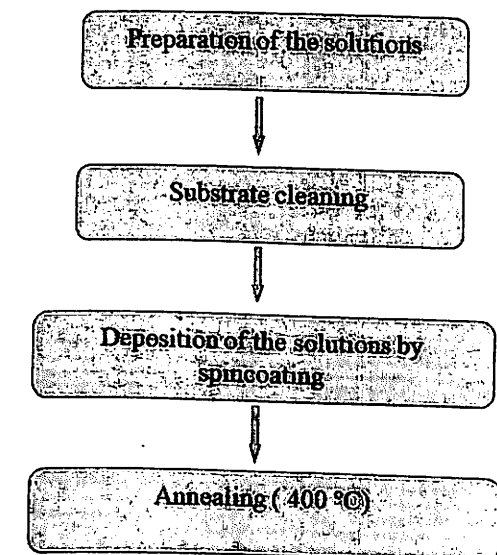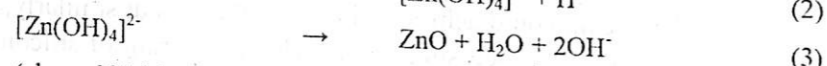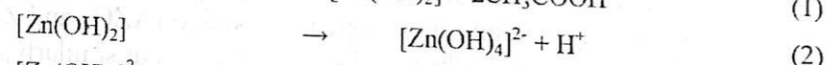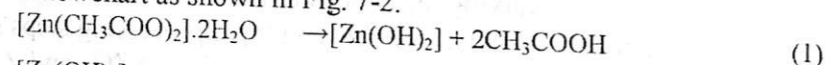

Fig. 7-1. Fabrication of ZnO/p-Si heterostructure

2.2. Synthesis of zinc oxide solution

Thin films of semiconducting ZnO nanostructures were successfully synthesized via a simple and cost-effective solution-based process. Here 20 ml deionized (DI) water was taken in a clean beaker. 0.1 g of polyvinyl alcohol (PVA) was then added and stirred continuously for 2 hr at 1200

rpm, maintaining the temperature at 80-90°C until a transparent solution was obtained. 2.0 g of $(Zn(CH_3COO)_2 \cdot 2H_2O$ was added to the solution maintaining the temperature at 100°C and stirred continuously for 10 minutes at 1200 rpm. To neutralize the pH of the solution, 0.2 ml of sodium hydroxide (NaOH) was added drop-wise to the final solution and was stirred continuously at 150°C till we get a homogeneous milky white solution. The whole reaction involved in the formation of ZnO nanostructure is given below. The methodology for the synthesis of the zinc oxide solution is depicted in the form of the flowchart as shown in Fig. 7-2.

$$[Zn(CH_3COO)_2].2H_2O \rightarrow [Zn(OH)_2] + 2CH_3COOH \qquad (1)$$
$$[Zn(OH)_2] \rightarrow [Zn(OH)_4]^{2-} + H^+ \qquad (2)$$
$$[Zn(OH)_4]^{2-} \rightarrow ZnO + H_2O + 2OH^- \qquad (3)$$
(above 300 °C)

2.3. Substrate cleaning, Deposition of the solutions and Annealing of the samples

The commercially purchased silicon wafer (p-type, 100) was diced into 1x1 cm² and thoroughly cleaned using standard RCA-I and RCA-II cleaning procedures. After cleaning, the wafers were dried in an oven at 200 °C for 2 hrs and stored for further use. The zinc oxide solution synthesized as discussed in section 2.1, was spin-casted on a clean silicon substrate using a spincoater (spin NXG-M1, APEX EQUIPMENTS) to obtain uniform thin films of semiconducting zinc oxide. Typically, the solution was fed into a syringe and dropped on the substrate, held by the substrate holder by a means of the inbuilt vacuum system and spin-coated (RPM: 1000, time: 60 secs). The process was repeated five times. Subsequently, the samples were dried in an oven for 30 minutes and annealed in the furnace at 400 °C for 1 hr where the rise in the furnace temperature was set at 4 °C/minute, to obtain crystalline thin films of semiconducting zinc oxide.

3. Results and discussion

3.1. X-Ray Diffraction (XRD) analysis

X-ray diffraction analysis is an important characterization technique mostly used in solid-state chemistry and material science processing. It enables us to probe the crystalline structure at the atomic level. The size and shape of the unit cell for a particular compound can be determined using X-Ray diffraction. This technique is used for the investigation of the atomic and molecular structure of a crystal, where a beam of incident X-ray is diffracted to a specific angle from each set of lattice planes of the crystalline atoms. The information regarding the structures of the materials, phase, and preferred crystal orientation can be obtained from this analysis. It can also provide information regarding average grain size, crystallinity, strains, and crystal defects. To investigate the crystallographic structure and phase of the prepared

20 ml DI + 0.1 g PVA

1200 rpm, 80-90 °C → Stirring for 2 hrs

Add 2 g (Zn(CH₃COO)₂·2H₂O

1200 rpm, 100 °C → Stirring for 10 mins

Add 0.2 ml NaOH (drop-wise)

1200 rpm, 150 °C → Stirring for ~ 2 hrs

Final ZnO milky white solution
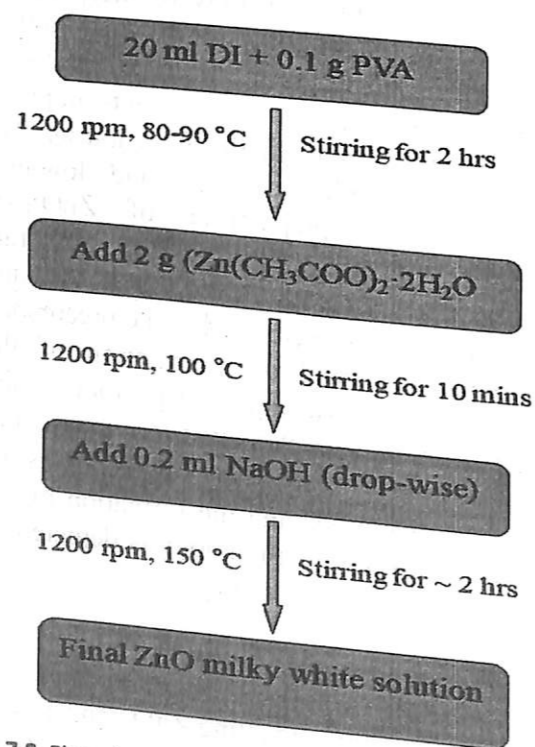
Fig. 7-2. Flow chart depicting the synthesis of zinc oxide solution
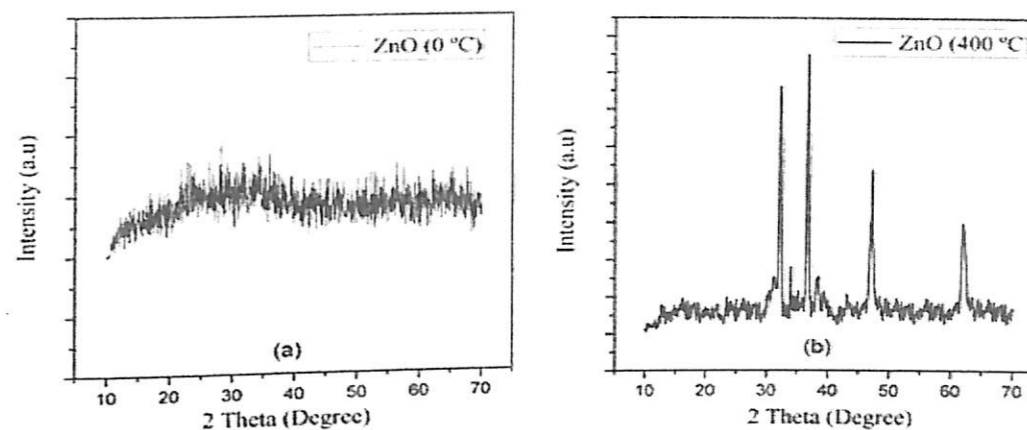
Fig. 7-3. XRD spectrum of ZnO nanostructure (a) (0 °C), (b) (400 °C)

samples X-ray diffraction analysis was performed by using (XRD, RIGAKU-MINIFLUX Cu-Karadiation(λ=1.540598 Å) with 30 kV, 15 mA) at a scan rate of 1°/min in angles from 10 to 70 degrees. The X-ray diffraction pattern of ZnO nanostructures before annealing (Fig. 7-3(a)) shows no characteristic peaks, indicating poor crystalline nature, revealing an amorphous structure of the film[24], whereas the spectrum for the sample annealed at 400 °C (Fig. 7-3(b)), showed the characteristic peaks related to (100), (101), (102), and (103) planes of ZnO.

Annealing is an important process in the semiconductor material processing. Generally, the aforementioned process results in transformation in the inner structure. The process leads to phase transformation by a means of crystallization process. Experimentally, annealing of nanostructured semiconductor is commonly used, resulting to successful alteration in the semiconductors properties [25, 26].Due to the annealing of the sample, it is noticed that the alignment of ZnO particles was also increased due to which the intensity of the peaks is increased at corresponding crystal planes of the crystalline phase of ZnO, attributed to a reduction in the density of samples, resulting in enhanced crystalline phase of ZnO. The average crystal size of nanostructures was calculated using Debye-Scherrer's formula given by equation (4).

$$D=K\lambda / (\beta cos\theta) \qquad (4)$$

where D is the crystal size; λ=0.15406 nm is the wavelength of the X-ray radiation used; K ~0.89, is the shape factor, and β is the full-width at half-maximum of the main peak (FWHM). The average crystal size along with various parameters obtained from the diffraction spectra are presented in Table 7-1. The average crystal size of the samples annealed at 400 °C, was found to be 20.80 nm.

Table 7-1. Parameters obtained for the Diffraction peaks

Sample	(hkl) planes	2θ (Deg)	FWMH (Deg)	Crystal size (nm)	Average size (nm)
ZnO(0 °C)	--	--	--	--	--
ZnO(400 °C)	(100)	32.22	0.316	25.88	20.80
	(101)	36.71	0.290	28.55	
	(102)	47.13	0.600	14.29	
	(103)	62.12	0.632	14.51	

3.2. Scanning Electron Microscopy/Energy Dispersive X-ray analysis

The scanning electron microscope, shortly known as SEM is an analysis technique used to investigate the surface morphology of the materials, thin films, particles and fibres using image analysis. In principle a focused beam of electrons is used for scanning the sample, producing various signals due to the interaction between the electrons and the atoms in the samples. The positions and the intensity of the detected signals are combined to produce an image, using a secondary electron detector. In certain areas of research such as material science, chemical science, semiconductor processing, biological sample analysis etc, SEM becomes a powerful technique for the investigation/exploration of the surface morphologies and the chemical characteristics of the sample. SEM/EDX analysis is a powerful technique with an added benefit, where the elemental composition (atomic % and weight %) of the sample being studied can be obtained. Elemental mapping along with the distribution across the surface of the sample is also available.
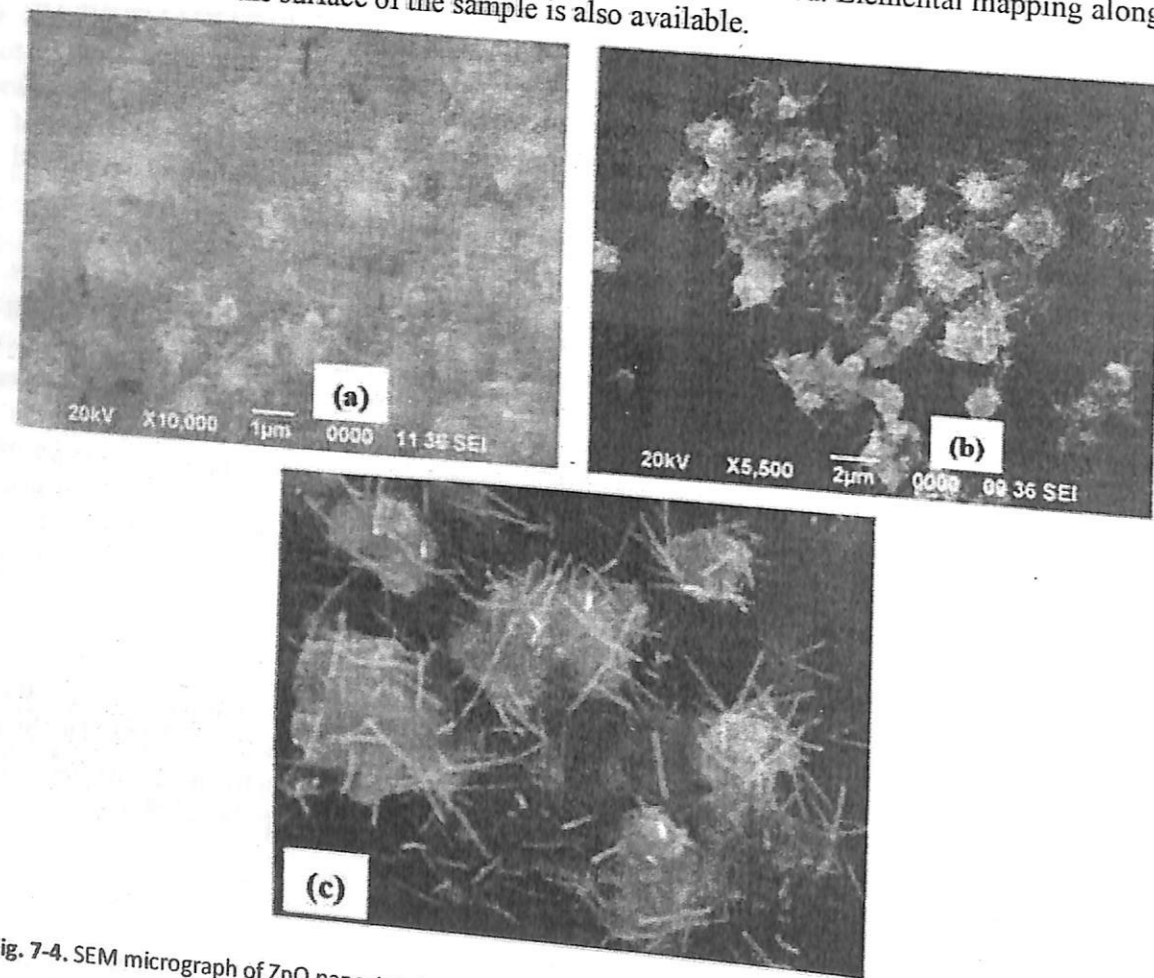
Fig. 7-4. SEM micrograph of ZnO nanostructure, (a) (0 °C), (b) (400 °C), (c) zoomed at a portion of (b)

The structure, morphology, and elemental composition of the prepared zinc oxide nanostructure were investigated using scanning electron microscopy, SEM (JOEL, JSM6390LV).Fig. 7-4(a) and (b), show the morphology of the synthesized zinc oxide nanostructure before annealing and annealed 400 °C, respectively. From the SEM analysis result, it is evident that the annealing temperature has a significant role in the formation of the nanorods. High-temperature heat treatment (annealing) is required for the development of zinc oxide nanoparticles/nanorods. The SEM image of the sample without annealing does not show any distinct structure. The SEM micrograph, Fig. 7-4(b), clearly shows that annealing is a mandatory step for the formation of nanorods/nanowires, and the generation of crystalline phase (as supported by XRD analysis). Fig. 7-4 (c), shows the SEM micrograph zoomed at one portion of Fig. 7-4 (b), clearly depicting the successful growth of ZnOnanorods/nanowires. This property plays a significant role in the semiconductor properties by enhanced conductivity/mobility of the semiconductor, resulting in enhanced charge transfer efficiency

and reduced charge recombination, making it an interesting material to be used in various optoelectronic applications.

EDX analysis has been carried out to investigate the percentage of elemental composition in the prepared samples. The EDX result of ZnO before annealing shows a composition weight percentage of 24.31 and 75.69 for zinc and oxygen, respectively. Whereas, zinc oxide annealed at 400 °C contains 35.06 and 64.94 percentage of zinc and oxygen in the sample. The EDX spectra for the samples are presented in Fig. 7-5 (a & b), and the essential parameters are depicted in the corresponding Table 7-2.

Table 7-2. Elemental composition of ZnO samples

Sample	Zn Weight%	O Weight%	Zn Atomic%	O Atomic%
ZnO (0 °C)	24.31	75.69	7.29	92.71
ZnO (400 °C)	35.06	64.94	11.68	88.33
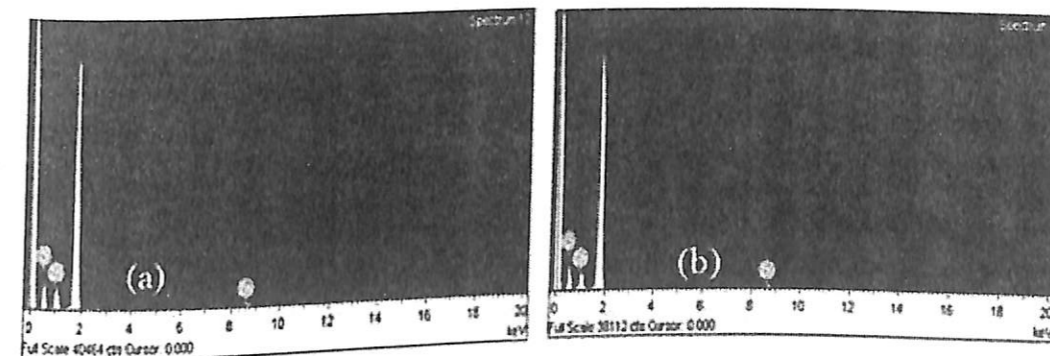
Fig. 7-5. EDX spectrum of zinc oxide nanostructure, (a) (0 ºC), (b) (400 ºC)

3.3. UV-vis spectroscopy analysis

UV-vis spectroscopy was performed in the ambient condition by UV-vis spectrophotometer (UV-10) to study the optical characteristics of the deposited thin films of zinc oxides. Fig. 7-6 (a & b) depicts the transmission spectra of samples before annealing and annealed at 400 °C, respectively.
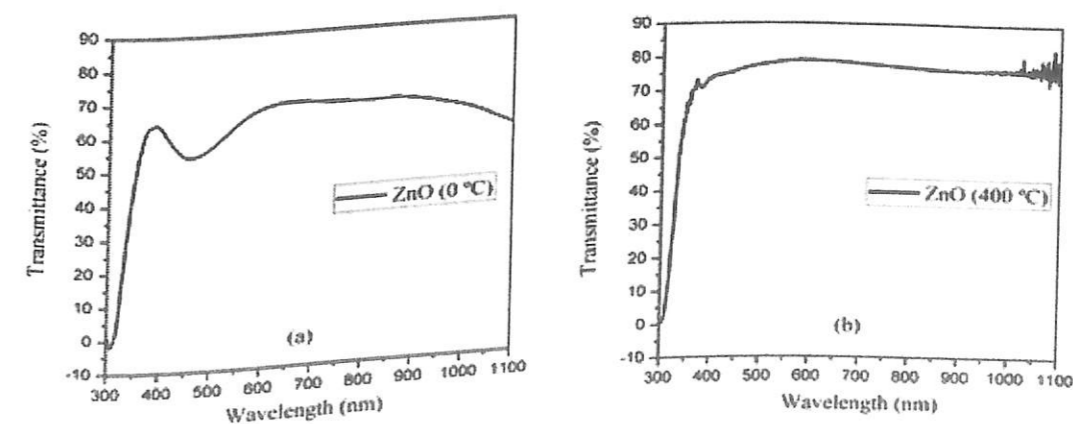
Fig. 7-6. Transmission spectrum of ZnO thin film nanostructure, (a) (0 °C), (b) (400 °C)

From the results, it is concluded that the transmittance of the film could be enhanced from around 70% to above 80% in the visible regime after annealing the sample at 400 °C for 1 hour. This
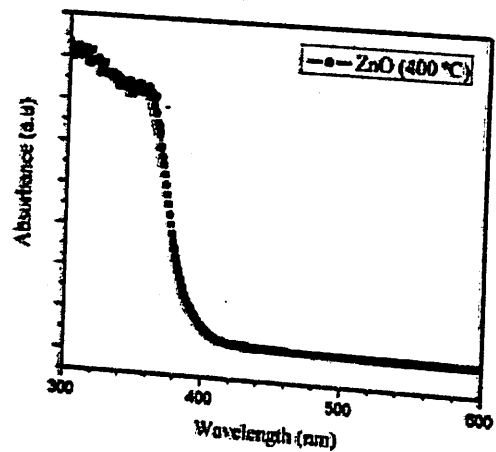
Fig. 7-7. Absorbance spectrum of ZnO thin film annealed at 400 °C

property can play a pivotal role in the efficiency enhancement of heterojunction solar cells by allowing more numbers of incident photons to strike at the interface or the junction, resulting in the
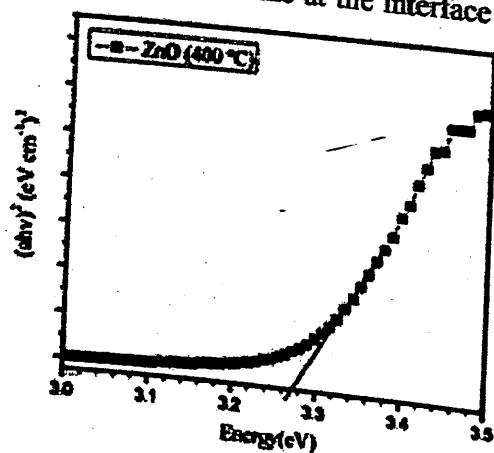
Fig. 7-8. Taucs' plot for estimation of optical band gap for ZnO annealed at 400 °C

generation of enhanced numbers of photo-excited charge carriers. Fig. 7-7, shows the absorption spectra of samples annealed at 400 °C. The optical bandgap of semiconducting zinc oxide nanostructure was estimated using Tauc' plot (Fig. 7-8) by plotting $(\alpha h\upsilon)^2$ versus $h\upsilon$ and found to be 3.27 eV.

Fig. 7-9 presents the schematic band diagram of ZnO/p-Si heterostructure. Uponheterojunction formation between p-silicon (Φ=4.91 eV, χ =4.05 eV, E_g =1.12 eV), and n-zinc oxide (Φ=5.2 eV, χ =4.3 eV, E_g =3.26 eV) [28], an electron depletion layer is generated at the interface between the p-Si and n-ZnO, due to which bend bending occurs. A small discontinuity in the band bending is due to the unavoidable native SiO_x/SiO_2 on the top of the silicon. Negatively charged ions and positively charged ions are distributed on p-Si and n-ZnO sides, respectively, creating an electric field at the interface from ZnO to p-Si, resulting to the generation of barrier potential (Φ_{ZnO-Si}) (Fig. 7-9), which prevents the flow of electrons and holes from one side to the other. The barrier potential was found to be 0.3 eV, pretty close to the difference in the work function of zinc oxide and p-silicon. Upon illumination, the electric field generated at the junction will immediately sweep the photo-excited charge carriers generated at the space charge region. Electrons will be swept towards zinc oxide, and the holes will be pushed towards p-silicon. This causes a potential difference to appear across the junction to generate photovoltage when light is incident on the cell.
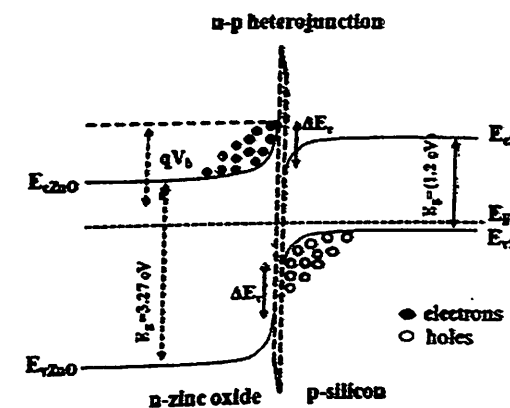
Fig. 7-9. Schematic Energy band diagram of ZnO/p-Si heterostructure

4. Conclusions:

In the present work, a crystalline thin film of semiconducting zinc oxide nanostructure could be synthesized by using a simple, efficient and low-cost sol-gel approach. The characteristics material properties including crystallinity, surface morphology, elemental compositions, transmittance, and absorbance of the semiconductor were analyzed using XRD, SEM/EDX, and UV-vis spectroscopy. The formation of highly crystalline ZnO nanostructure is attributed to the sintering of the sample at 400 °C for 1 hr. This property can play a pivotal role in efficiency enhancement in the heterojunction solar cell by faster transportation and extraction of photoexcited charge carriers to the electrodes due to enhanced conductivity and reduced series resistance. The UV-vis result revealed a high transmittance of above 80 % in the visible regime and the bandgap of the prepared semiconductor was estimated by using Taucs' plot and found to be 3.27 eV. The successfully fabricated ZnO/p-Si heterostructure has the potential application in many optoelectronic devices including photodetectors and heterojunction solar cells.

References
[1] M. Green, Solar energy 76 (2004) 3.
[2] E. Shi, et al, Scientific reports 2 (2012) 884.
[3] N. F. Habubi, A. O. Mousa, World Scientific News 18 (2015) 118.
[4] S. K. Behura, S. Nayak, I. Mukhopadhyay, O. Jani, Carbon 67 (2014) 766.
[5] D. Barpuzary, M. Qureshi, ACS applied materials & interfaces 5 (2013) 11673.
[6] N. Akçay, Journal of Materials Science: Materials in Electronics 31 (2020) 22467.
[7] K. Liu, M. Sakurai, M. Aono, Sensors 10 (2010) 8604.
[8] T. Ji, et al, Applied Surface Science 449 (2018) 358.
[9] K. Singh, et al, Sensor Letters 15 (2017) 771.
[10] Q. Hong, et al, ACS applied materials & interfaces 6 (2014) 20887.
[11] J. Jayachandiran, et al, Journal of Inorganic and Organometallic Polymers and Materials 28 (2018) 2046.
[12] D. C. Look, Materials Science and Engineering: B 80 (2001) 383.
[13] M. Rusop, Transactions on Electrical and Electronic Materials 13 (2012) 102.

[14] X. Chen, Z. Wu, D. Liu, Z. Gao, Nanoscale research letters 12 (2017) 1.
[15] L. Shen, et al, Superlattices and microstructures 48 (2010) 426.
[16] N. Aqab, H. Riaz, A. Nayfeh, IEEE 43rd Photovoltaic Specialists Conference (PVSC), 2016.
[17] R. Kek, et al, Materials Research Express 5 (2018) 116201.
[18] R. AIsmail, S. M. Al-Jawad, N. Hussein, Applied Physics A 117 (2014) 1977.
[19] R. Pietruszka, et al, Solar Energy Materials and Solar Cells 147 (2016) 164-70.
[20] R. Pietruszka, et al, Solar Energy Materials and Solar Cells 143 (2015) 99.
[21] R. Pietruszka, et al, Solar Energy 155 (2017) 1282.
[22] M. Dutta, S. Sarkar, T. Ghosh, D. Basak, The Journal of Physical Chemistry C 116 (2012) 20127.
[23] Z. Zang, Applied Physics Letters 112 (2018) 042106.
[24] M. Malek, et al, Journal of alloys and compounds 610 (2014) 575.
[25] S. Xue, et al, Journal of Alloys and Compounds 448 (2008) 21.
[26] T. Y. Ma, D. K. Shim, Thin Solid Films 410 (2002) 8.
[27] M. M. H. Farooqi, R. K. Srivastava, Proceedings of the National Academy of Sciences, India Section A: Physical Sciences (2019) 1.
[28] J. Y. Park, S. W. Choi, S. S. Kim, Journal of Physics D: Applied Physics 44 (2011) 205403.

Chapter 8: PRECISION MEASUREMENTS OF ATMOSPHERIC MIXING PARAMETERS AND OCTANT RESOLVING

Ankur Nath[a*] and Ng. K. Francis[a]

[a]Tezpur University, Sonitpur, Assam, India
*E.mail: ankur04@tezu.ernet.in

Abstract

This study performs precision measurements of atmospheric mass mixing parameter Δm^2_{31} and mixing angle θ_{23} in light of two accelerator experiments, T2K-II (Tokai-to-Kamioka) and NOvA-II (Neutrino Off-axis ν_e Appearance), and a reactor-based neutrino experiment JUNO. The work also explores the sensitivity of the three experiments combined to resolve octant degeneracy of θ_{23}. It is shown that the θ_{23} octant resolving can be improved significantly with short baseline reactor constraints θ_{13}.

1. Introduction

Super-Kamiokande discovered neutrino oscillation in 1998 and since then, neutrino experiments embarked into solving the problems of neutrino mass hierarchy (MH), leptonic CP violation (CPV), θ_{23} octant resolving and precision measurements of neutrino mixing parameters. Neutrino oscillations is a quantum mechanical phenomenon where neutrino can switch its identities when traveling. Probability for a α-flavor to oscillate into β-flavor, $P(\nu_\alpha \to \nu_\beta)$, depends on three mixing angles (θ_{12}, θ_{13}, θ_{23}), one CP-violating phase δ_{CP}, two mass square splittings (Δm^2_{21}, Δm^2_{31}), its energy E_ν, propagation distance L, and matter density which neutrino passed through, ρ. The probability for the appearance of β-flavour of neutrino from α-flavour neutrino is given by -

$$P(\nu_\alpha \to \nu_\beta) = \delta_{\alpha\beta} - 4\Sigma_{i>j}\Re\left(U^*_{\alpha i}U^*_{\beta i}U_{\alpha j}U_{\beta j}\right)\sin^2\left(\frac{\Delta m^2_{ij}L}{4E}\right) + 2\Sigma_{i>j}\Im\left(U^*_{\alpha i}U^*_{\beta i}U_{\alpha j}U_{\beta j}\right)\sin\left(\frac{\Delta m^2_{ij}L}{4E}\right)$$

where U is the PMNS mixing matrix [1], α, $\beta = \mu$, e and $i, j = 1, 2, 3$. $\alpha = \beta = \mu$ gives the survival probability of ν_μ. Disappearance (survival) probability of ν_μ provides a precise measurement of the atmospheric neutrino parameters, $\sin^2 2\theta_{23}$ and Δm^2_{31}, whereas appearance of ν_e is driven by $\sin^2 2\theta_{13}$ and sensitive to δ_{CP}.

To measure θ_{23}, one can use a measurement of ν_μ survival probability and/or appearance probability of ν_e from produced ν_μ, shown in Fig.8-1. The left plot shows that ν_μ survival probability is proportional to $\sin^2 2\theta_{23}$. With this measurement, it is unknown whether $\theta_{23} > \pi/4$ or $< \pi/4$ since they give same probability, so-called "*ambiguity of θ_{23} octant*". The right plot in Fig. 8-1 shows a $\delta_{CP}-\theta_{23}$
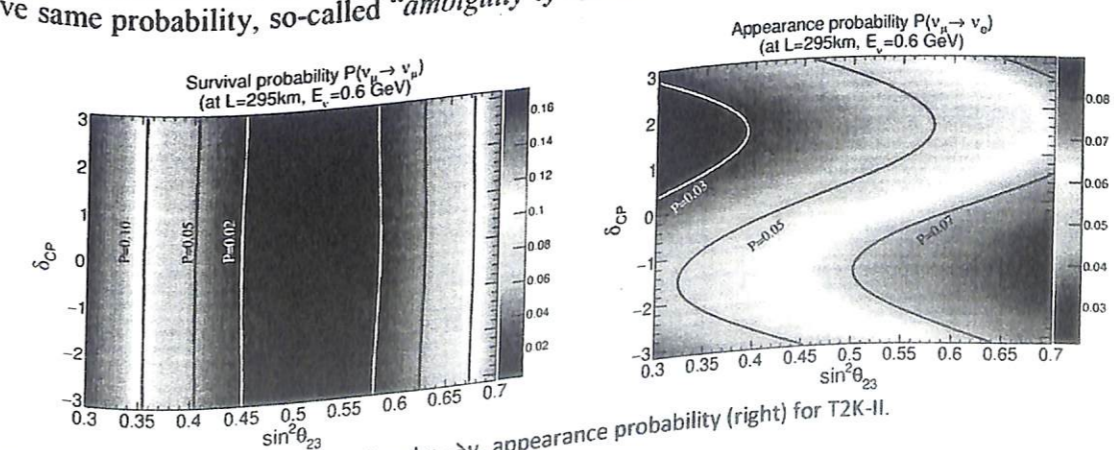

Fig. 8-1. ν_μ survival probability (left) and $\nu_\mu \to \nu_e$ appearance probability (right) for T2K-II.

degeneracy in the $\nu_\mu \to \nu_e$ appearance. Solving the θ_{23} octant can help us to better measure CP violation.

2. Experiment and simulation details

2.1. T2K-II:

Tokai-To-Kamioka (T2K) is the 2nd generation of accelerator-based long-baseline (LBL) neutrino oscillation experiments located in Japan, and T2K-II is a proposal to extend the T2K run until 2026. The T2K far detector, Super Kamiokande (SK), is 295 km away from the neutrino production source and the detector is a Cherenkov detector with 22.5 ktons fiducial volume of pure water. This capability allows T2K(-II) to measure simultaneously the disappearance of muon (anti-)neutrinos and the appearance of electron (anti-)neutrinos from the flux of almost pure muon (anti-)neutrinos. In Ref. [2], T2K proposes to collect 20×10^{21} protons-on-target (POT) thereby exploring CPV with a confidence level 3σ or higher if $\delta_{CP} \sim 270°$ and make precision measurements of θ_{23} and Δm^2_{31}.

2.2. NOvA-II:

NuMI Off-axis ve Appearance is a 2nd generation accelerator LBL neutrino experiment placed in the US with a baseline of 810 km between the production source and the far detector. Such long baseline allows to explore the MH with high sensitivity via the matter effect on the (anti-)neutrino interactions. The far detector is filled with liquid scintillator contained in PVC cells, totally weighted up 14 ktons. In Ref. [3], NOvA aims to extend the run through 2024, we call as NOvA-II, in order to get 3σ or higher sensitivity to the MH in case the MH is normal more than 2σ sensitivity to CPV.

2.3. JUNO:

Jiangmen Underground Neutrino Observatory (JUNO) [4] is a reactor-based medium-baseline neutrino experiment located in China and houses a 20 kton large liquid scintillator detector for detecting the electron anti-neutrinos from the Yangjiang (YJ) and Taishan (TS) nuclear power plants (NPPs) with an average baseline of 52.5 km. Each of the six cores at YJ nuclear plant will produce a power of 2.9 GW and the four cores at TS NPP will generate 4.6 GW each. They combine to produce 36 GW thermal power. With 6 years of data taking, JUNO can achieve better than 1% precision on the solar neutrino parameters θ_{12} and Δm^2_{21} and the atmospheric neutrino mass-squared splitting Δm^2_{31}.

General Long Baseline Experiment Simulator (GLoBES) [5] is used for simulating the statistical significance of the experiments, using flux, cross section, signal/background efficiency, and systematic error as input parameter. Simulation is tuned to obtain the same energy spectral as the design reports.

Table 8-1. Experimental Specifications

Parameters	T2K-II	NOvA-II	JUNO
Exposure (POT)	20×10^{21}	7.2×10^{21}	6yrs @36GW-th
Baseline (km)	295	810	52.5
Energy peak/range	~0.6 GeV	~2.0 GeV	1.8-9 MeV
(Far) Det. Type	Water Cherenkov	Liquid Scintillator	Liquid Scintillator
(Far) Det. Mass	22.5 kt	14 kt	20 kt

3. Results and discussion

We assume true neutrino mass hierarchy (MH) as normal hierarchy (NH). We use both $\nu_\mu \to \nu_e$ appearance and $\nu_\mu \to \nu_\mu$ disappearance samples in this simulation. The true values of oscillation parameters assumed are given in **Table 8-2**.

Table 8-2. Constraint of oscillation parameters with the global neutrino data

Parameter	$\sin^2\theta_{12}$	$\sin^2\theta_{13}$	$\sin^2\theta_{23}$	δ_{CP} (°)	Δm^2_{21} (eV^2)	Δm^2_{31} (eV^2)
Best fit (NH)	0.310	0.02241	0.558	222	7.39e-5	2.523e-3

Fig. 8-2 shows the allowed region in the $\sin^2\theta_{23}$-Δm^2_{31} space at 90% C.L. for T2K-II with reactor constraints, T2K-II and NOvA-II combined, JUNO only and T2K-II+NOvA-II+JUNO (joint analysis) combined. Given a true $\sin^2\theta_{23}$ (octant is known), we calculate the statistical significance[1] analysis.
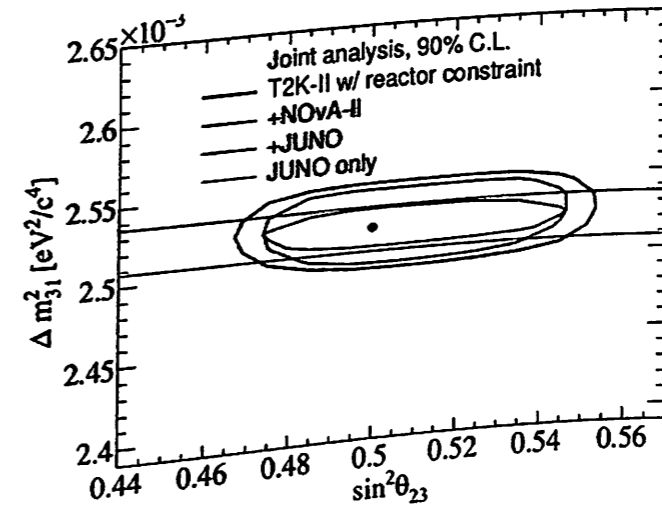
Fig. 8-2. Allowed region in the $\sin^2\theta_{23}$-Δm^2_{31} space at 90% C.L. with various experimental setups. Normal MH and $\sin^2\theta_{23} = 0.5$ are assumed [6].

$\sqrt{\Delta\chi^2}$ to exclude the wrong octant. The allowed regions of $\sin^2\theta_{23}$ as a function of true $\sin^2\theta_{23}$ can be obtained, e.g. at the 3σ C.L, as shown in Fig. 8-3. The statistical significance to exclude the wrong octant.
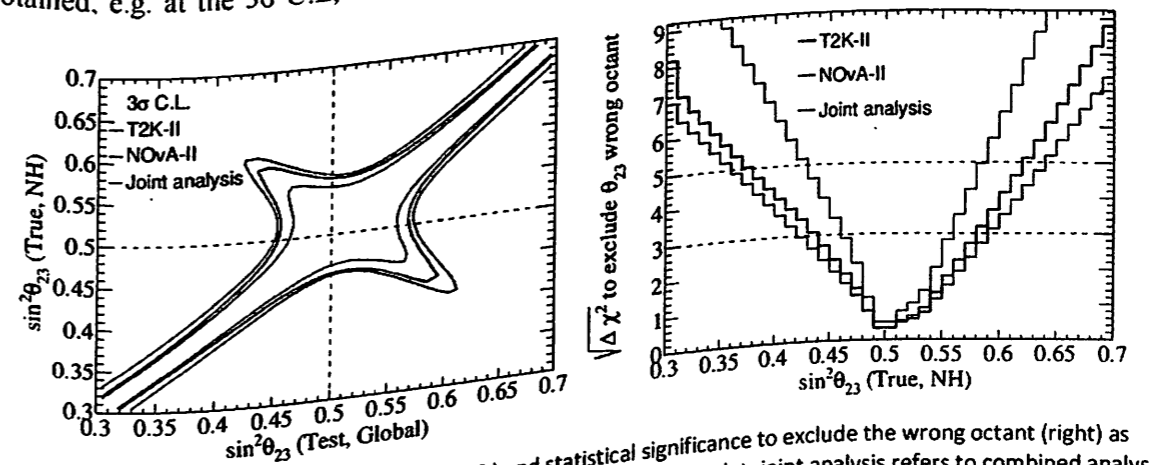
Fig. 8-3. Allowed region of $\sin^2\theta_{23}$ at 3σ C.L. (left) and statistical significance to exclude the wrong octant (right) as function of $\sin^2\theta_{23}$. Normal (MH) and $\delta_{CP} = -270°$ are assumed [6]. In the plot, joint analysis refers to combined analysis of T2K-II+NOvA-II+JUNO.

octant for a given true *(non-maximal)* value of θ_{23} is calculated by taking the difference between the minimal value of the global χ^2 in the wrong octant and the true octant of θ_{23}. The octant resolving sensitivities with T2K-II alone or with a combined analysis is shown in Fig, 8-3. The θ_{23} octant resolving power can be enhanced significantly when combining T2K-II and NOvA-II data samples, particularly the θ_{23} octant can be determined at around 3σ C.L. if $\sin^2\theta_{23}$ is ≤ 0.46 or ≥ 0.56.

4. Conclusions:

We performed the precision measurements of $\sin^2\theta_{23}$ and Δm^2_{31} and octant resolving of θ_{23}. A combined analysis of T2K-II and NOvA-II, can reach a sub-percent level precision on the Δm^2_{31} mass-squared splitting comparing the results to measurements from reactor-based short-baseline neutrino experiments and JUNO respectively. Also, a combined analysis of T2K-II and NOvA-II offers a great sensitivity to determine the octant of the θ_{23} mixing angle.

Acknowledgements:

References:
[1] Z. Maki, M. Nakagawa and S. Sakata, Prog. Theor. Phys. 28 (1962) 870.
[2] T2K Collaboration, K. Abe et al., arXiv1607.08004.
[3] NOvA Collaboration M. Sanchez, XXVIII International Conference on Neutrino Physics and Astrophysics (2018).
[4] JUNO Collaboration, Z. Djurcic et al., arXiv1508.07166.
[5] P. Huber, J. Kopp, M. Lindner, M. Rolinec and W. Winter, Computer Physics Communications 177 (2007) 432.
[6] S. Cao, A. Nath, T. V. Ngoc, Ng. K. Francis, N. T. H. Van and P. T. Quyen, 12 (2009) 08585.

Chapter 9: DETECTION METHODS AND NEUTRINO OSCILLATION EXPERIMENTS: A SHORT REVIEW

Ankur Nath

Tezpur University, Sonitpur, Assam, India
E-mail: ankur04@tezu.ernet.in

Abstract

Neutrino physics is an experimentally driven field. This review paper describes the different detection techniques available in the literature and studies a few neutrino oscillation experiments. The primary focus is on the construction and detection mechanisms of each experiment. In the last decades, we learnt about neutrinos by performing different experiment at different times with different neutrino sources viz. solar, atmospheric, reactor, accelerators and high energy astrophysical; and they have contributed in the determination of neutrino parameters. We need to determine more precise values of the already known parameters $(\theta_{12}, \theta_{13}, \theta_{23}, \Delta m^2_{21}$ and $|\Delta m^2_{31}|)$ and unravel the completely unknown parameters $(\text{sign}(\Delta m^2_{31})$, δ_{CP} and octant of $\theta_{23})$. Other unknown properties include absolute masses of neutrino, number of neutrino species and whether the neutrino is Dirac or Majorana particle. We review a few detection methods employed in the neutrino oscillation experiments and discuss the capabilities of the experiments in addressing the unsolved properties of neutrinos.

Keywords: standard model, neutrino, oscillation parameters, neutrino sources and detection

1. Introduction

1.1. History and Background

Wolfgang Pauli, for the first time in 1930, postulated the existence of the neutrino as a particle with no net charge and no mass, to explain the discrepancy in the beta decay spectrum. The first-ever direct detection of electron anti-neutrino by Clyde L. Cowan et al.[1] took place at the Savannah river reactor plant in South Carolina in 1956. Thereafter, the physics community started conducting underground *(in old mines, excavated beneath the mountains)*, under water *(on seabed)* and under ice experiments and a good number of experiments have been upgraded from time to time to understand better about this particle. The other two active neutrinos viz. muon neutrino (ν_μ) and tau neutrino(ν_τ) were directly observed in 1962[2] and 2000[3] respectively. All the existing experiments detecting the neutrinos from natural sources *(solar, atmospheric and astrophysical)* and man-made sources *(reactor and accelerator-based, see Fig. 9-1)* are based on one of the detection techniques viz. radiochemical methods, Cherenkov method *(water, ice)*, scintillation technique *(solid, liquid)*, tracking calorimeter, nuclear emulsions and liquid argon (LAr).

1.2. Neutrino Oscillation

The Standard Model (SM) of particle physics contains three generation of quarks, three generations of leptons, force carriers of the fundamental interactions *(gluons for strong interactions, $W^\pm$ and Z^0 for weak interactions, graviton for gravitational force and photon for electromagnetic interactions)* and the mass generating particle Higgs boson (H^0). The neutrinos are leptons that are massless within the SM. However, in 2015, Nobel Prize was awarded to Prof. Takaki Kajita and Prof. Arthur D. McDonald for the phenomenon of neutrino oscillation that requires the neutrinos to have mass.
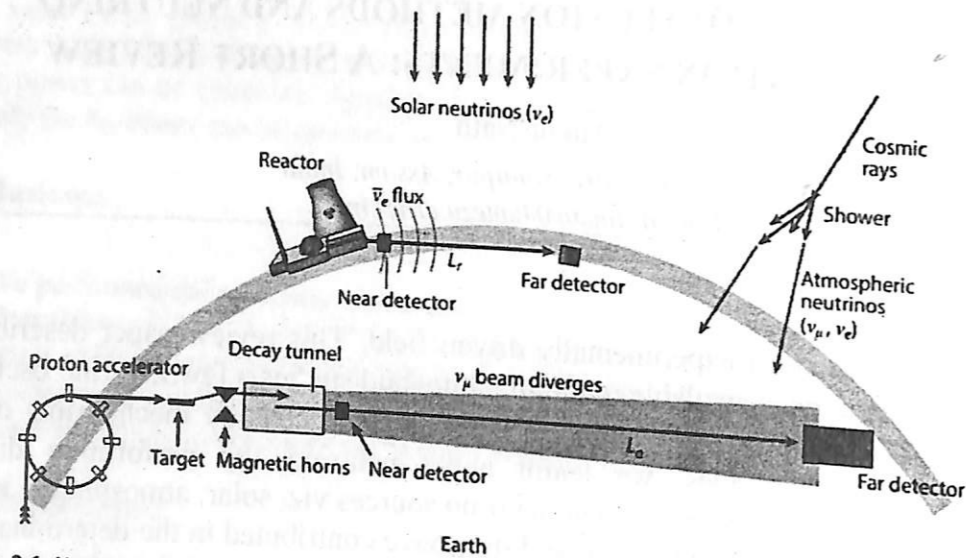
Fig. 9-1. Natural and artificial sources of neutrino in a nutshell [5]

The three known neutrino flavor states (ν_e, ν_μ, ν_τ) are expressed as quantum superposition of three massive states ν_k ($k=1,2,3$) with different masses m_k with a 3X3 unitary mixing matrix $U_{\alpha k}$ ($\alpha=e^-,\mu,\tau$), known as PMNS (Pontecorvo-Maki-Nakagawa-Sakata) matrix U_{PMNS}, given by-

$$U_{PMNS} = U_{\alpha k} = \begin{bmatrix} U_{e1} & U_{e2} & U_{e3} \\ U_{\mu 1} & U_{\mu 2} & U_{\mu 3} \\ U_{\tau 1} & U_{\tau 2} & U_{\tau 3} \end{bmatrix}$$

$$= \begin{bmatrix} c_{12}c_{13} & s_{12}c_{13} & s_{13}e^{-i\delta_{CP}} \\ -s_{12}c_{23}-c_{12}s_{13}s_{23}e^{i\delta_{CP}} & c_{12}c_{23}-s_{12}s_{13}s_{23}e^{i\delta_{CP}} & c_{13}s_{23} \\ s_{12}s_{23}-c_{12}s_{13}c_{23}e^{i\delta_{CP}} & -c_{12}c_{23}-s_{12}s_{13}c_{23}e^{i\delta_{CP}} & c_{13}c_{23} \end{bmatrix} \quad (1)$$

where, $c_{ij}=\cos\theta_{ij}$ and characterized by three non-zero angles θ_{kl} and a charge-parity violating phase δ_{CP}. The mixing angles θ_{kl} are associated with solar, atmospheric and reactor neutrinos given by θ_{12}, θ_{13} and θ_{23} respectively, the mass-squared differences i.e. the mass splitting terms being Δm^2_{21}, Δm^2_{31} (Δm^2_{32}), with $\Delta m^2_{ij}=m^2_i-m^2_j$ such that $\Delta m^2_{21}>0$ and $\Delta m^2_{3n}\equiv\Delta m^2_{31}>0$ is positive for Normal Mass Hierarchy (NH) and $\Delta m^2_{3n}\equiv\Delta m^2_{32}<0$ is negative for Inverted Mass Hierarchy (IH) for the neutrino mass spectrum.

The probability for the transition of β-flavor of neutrino from α-flavor neutrino is expressed by:

$$P(\nu_\alpha \to \nu_\beta) = \delta_{\alpha\beta} - 4\Sigma_{i>j}\Re\left(U^*_{\alpha i}U^*_{\beta i}U_{\alpha j}U_{\beta j}\right)\sin^2\left(\frac{\Delta m^2_{ij}L}{4E}\right)$$

$$+ 2\Sigma_{i>j}\Im\left(U^*_{\alpha i}U^*_{\beta i}U_{\alpha j}U_{\beta j}\right)\sin\left(\frac{\Delta m^2_{ij}L}{4E}\right) \quad (2)$$

Briefly, the probability for an α-flavor to oscillate into β-flavor depends on the three mixing angles, the CP violation phase, the two mass-squared splittings, neutrino energy, baseline of the experiment (L) and the amount of matter neutrinos passing through matter of density. In equation 2, α=β corresponds to disappearance or survival probability of initial flavor α.

It is not certain whether $\theta_{23}<45°$ or $\theta_{23}>45°$ (referred as octant degeneracy) if θ_{23} mixing is not maximal. In equation 1, a purely real matrix corresponds to δ_{CP} being an integer multiple of π and any other value is indication of violation of Charge-Parity (CP) symmetry in any neutrino appearance channel, through the Kobayashi–Maskawa mechanism [4]. The discovery of CP violation in the lepton sector is of great interest and is a major focus of current experiments. Another pressing problem is the sign of Δm^2_{31} which decides the hierarchy of the mass eigenstates. $\Delta m^2_{31}>0$ ($m_1<m_2<m_3$) refers to normal mass hierarchy (NH) and $\Delta m^2_{31}<0$ ($m_3<m_1<m_2$) refers to inverted mass hierarchy (IH). The aim of the ongoing and future experiments is to precisely determine the neutrino mass hierarchy, the octant of θ_{23} and the values of δ_{CP}.

1.3. Neutrino Sources

Neutrinos are the most abundant massive particles in the universe. They are produced in the stars, Earth's atmosphere, supernovae and active galactic nuclei. The man-made sources include neutrino production in nuclear fission in reactors and through pion decay in accelerators. Neutrinos are also produced in the core of the sun through nuclear fusion reactions. The major contribution comes from proton-proton (pp) reaction. More than 90% of the solar neutrinos are produced in the pp process. Neutrino is also produced during production of ^{7}Li and ^{8}B nuclei. The solar neutrinos are electron neutrinos in nature. The deuteron with another proton produces a Helium (^{3}He) nucleus and gamma ray which further results in production of ^{4}He isotope. Both the Helium isotopes now fuse to form Beryllium (^{7}Be) and a gamma ray. The ^{7}Be, then, undergoes electron/proton capture to produce ^{7}Li/^{8}B and electron neutrino. The reactions involved are-

$$p + p \to d + e^+ + \nu_e \,(pp)$$
$$^7Be + e^- \to {}^7Li + \nu_e$$
$$^7Be + p \to {}^8B + \gamma$$
$$^8B \to {}^8Be + e^+ + \nu_e$$
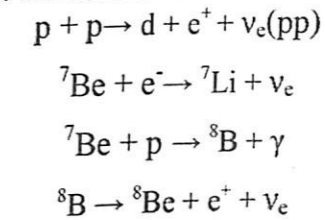
Detection of electron neutrinos is also reported from depth of the solar core through carbon-nitrogen-oxygen (CNO) cycle [6].

Reactor neutrinos are produced in the man-made nuclear reactors via nuclear fission of radioactive isotopes of Uranium and Plutonium generally. They are produced in large quantities and they come in only one flavor: electron antineutrinos. The reaction involved in the production of reactor neutrinos is the beta decay process, given by-

$$n \to p + e^- + \bar{\nu}_e$$
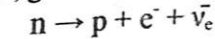
Atmospheric neutrinos are typically produced around 15 kilometers above Earth's surface. They form when a cosmic ray, high energetic particles (mostly protons) from space interact with the Earth's atmosphere. When they strike an atomic nucleus in our atmosphere, there is a cascade of particles. Short-lived particles called mesons form, most of them pions (and a few kaons). These are unstable particles made of two quarks, and they rapidly decay into muons and muon antineutrinos (or antimuons and muon neutrinos). A muon, being unstable, also undergoes decay into an electron, electron antineutrino, and muon neutrino. About two-thirds of atmospheric neutrinos are muon neutrinos and antineutrinos, and the remainder are electron neutrinos and antineutrinos. The reactions involved in the process are-

$$p+X \,(hadron) \to \pi^\pm (K^\pm) \to \mu^\pm + \nu_\mu \,(\bar{\nu}_\mu) \text{ (primary/dominant decay)}$$
$$\mu^\pm \to e^\pm + \nu_e \,(\bar{\nu}_e) + \bar{\nu}_\mu \,(\nu_\mu) \text{ (secondary decay)}$$
$$K^\pm \to e^\pm + \nu_e \,(\bar{\nu}_e) + \pi^0$$
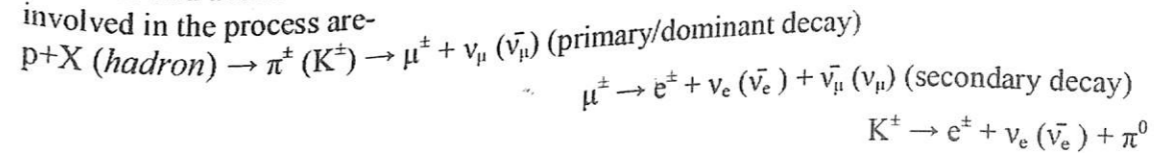
Neutrinos are produced in the accelerator using a similar process as that of atmospheric neutrinos. They are man-made neutrinos where a proton is accelerated to a high energy (of the order of GeV) and hit on a target (X) resulting in production of pions and associated muon neutrinos (anti-neutrinos). The positively (negatively) charged pions are unstable and decay to muons (anti-muons) and almost a pure beam of muon neutrino (anti-neutrino) form. Thus, accelerated neutrinos and anti-neutrinos form almost a pure beam of muon neutrino (anti-neutrino) and they are focussed using high magnetic field to a detector, generally placed underground, 1-10,000 km apart.

2. Neutrino Experiments

2.1. Solar Experiments

Solar experiments measure the electron neutrino disappearance probability $P(\nu_e \rightarrow \nu_e)$, and are sensitive to mixing angle θ_{12} and small mass mixing Δm^2_{21}. Notable solar neutrino experiments are Homestake-Cl, GALLEX, GNO, SAGE, SNO and Borexino.

2.2. Reactor Experiments

Reactor experiments measure the electron anti-neutrino disappearance probability of electron anti-neutrino and are sensitive to mixing angle θ_{13} and solar parameters. Chooz, Double Chooz, KamLAND, RENO, Daya Bay and JUNO experiments use electron anti-neutrinos for neutrino oscillation analysis.

2.3. Atmospheric Experiments

Atmospheric experiments uses the high flux of muon neutrinos to measure the $P(\nu_\mu \rightarrow \nu_\mu)$, $P(\nu_\mu \rightarrow \nu_\tau)$, $P(\nu_\mu \rightarrow \nu_e)$ and the respective anti-neutrino oscillations channels to extract θ_{23}, Δm^2_{31} and CP-violating phase δ_{CP}. Kamiokande, Super Kamiokande, Hyper-Kamiokande, IceCube, PINGU and INO use atmospheric neutrinos for their study.

2.4. Accelerator-based Experiments

Accelerator-based experiments use muon neutrino (anti-neutrino) to measure $P(\nu_\mu \rightarrow \nu_e)$ and the corresponding anti-neutrino oscillations to measure the same parameters accessible to atmospheric neutrino experiments. These experiments are the most ideal sources to address CP violation in the lepton sector. The accelerator-based neutrino oscillation experiments K2K, T2K and T2HK are based in Japan, whereas, MINOS/MINOS+, NOvA and DUNE are located in the United States.

3. Neutrino Detection Techniques

3.1. Radiochemical Method

$$\nu_e + {}^A_Z X \rightarrow e^- + {}^A(Z+1)_Y \qquad (3)$$

Inverse Beta Decay (IBD) is the principle used in the radio chemical method of neutrino detection. In this process, when a solar neutrino is absorbed in the target of the detection medium, the target is c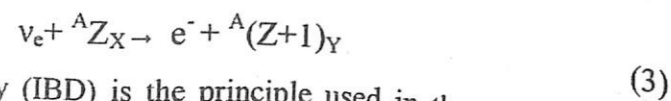onverted into a radioactive element whose decay is further studied and counted. The technique was exploited by the famous Homestake experiment, GALLEX, GNO and SAGE experiments to detect low energy solar neutrinos. The advantage of Gallium target of GALLEX/GNO/SAGE over chlorine target of Homestake is that with lower threshold i.e. Q-value,it is possible to detect neutrinos from the initial proton fusion chain in the Sun. The energy of the solar neutrinos vary from 0.2 to 18 MeV.

3.2. Cherenkov detector

The Cherenkov detection technique has been employed in order to investigate neutrinos for a large range of low to high energies from 0.1 GeV to 10 TeV. When a charged particle traverses in a medium of refractive index ɳ, polarization of atoms in the medium takes place resulting in dipole radiation. If such a particle moves slowly through the medium i.e. $v<c/\eta$, the radiation from the excited dipoles is emitted symmetrically around the path and sum of all dipoles vanishes. If the particle moves with a velocity greater than the local phase velocity of light i.e. $v>c/\eta$, the dipole distribution is asymmetric. As a result, the sum of all dipoles is non-zero and results in radiation of electromagnetic waves. The resulting light wavefront from the radiation is conical with an opening angle θ such that $cos\theta = 1/\beta\eta$ where $\beta = v/c$, v being the velocity of the particle and c, the speed of light (Fig. 9-2). We learn that there is a threshold value of β below which no radiation is emitted coherently w.r.t. to the particle position. For a high speed particle i.e. $\beta \approx 1$, there is maximum angle of emission, the Cherenkov angle with $\theta_{max} = cos^{-1}(1/\eta)$. By detecting the Cherenkov light in form of a cone (Fig. 9-3), in a large detector with an array of PMTs, the light cone is mapped into a characteristic ring. The ring with clean and sharp outer edge is a muon-ring
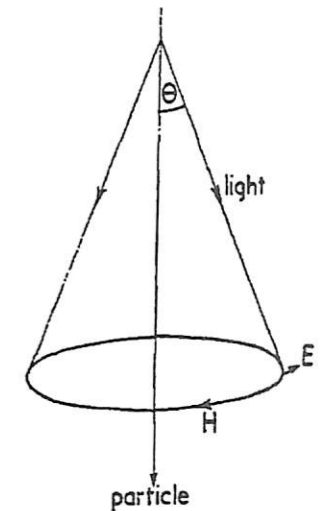
Fig. 9-2. Cherenkov radiation [7]
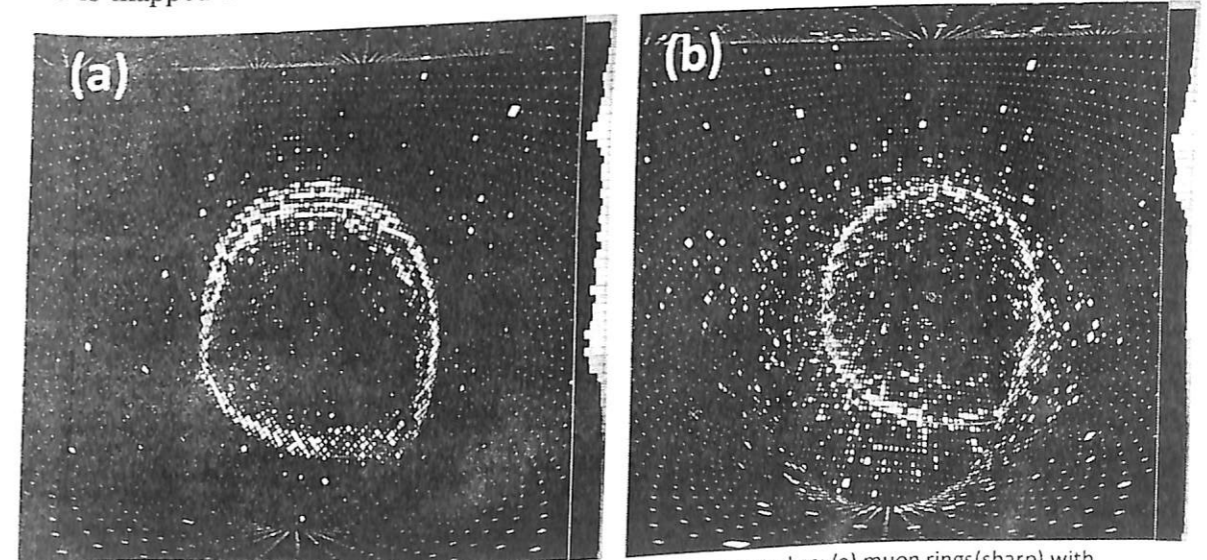
Fig. 9-3. Rings of Cherenkov light detected in 1998 by Super-K, reconstructed as: (a) muon rings(sharp) with momentum of 604 MeV, (b) electron rings(fuzzy) with momentum of 492 MeV. Images are taken from www.ps.uci.edu/~tomba/sk/tscan/compare_mu_e/

whereas the fuzzy ring produced by scattering of electrons corresponds to electron neutrino.

The identification of ν_τ is more difficult due to the short lifetime of the lepton. From the ring, the properties of the incoming particle can be understood precisely. The axis of the cone determines the direction of the particle, and the color of the light gives the particle energy. A few of the experiments which employ Cherenkov detectors are SNO, Super-Kamiokande, B-DUNT, ICARUS, IceCube, Kamiokande, KM3NeT, MiniBooNE, NEVOD, T2K and UNO.

3.3. Scintillation Technique

There are certain organic and inorganic materials which emit light flashes when charged particle, x-rays or gamma rays pass through them. These materials are called scintillators. If a charged particle, a gamma ray or an x-ray is incident on the scintillator, it interacts with matter in three ways: photoelectric effect, compton effect and pair production. In each of these effects, electrons of different energy ranges are produced by successive interactions and the kinetic energy of the

secondary electrons obtained ionizes the scintillator. The excited states of the scintillator material de-excite to lower states by emission of light flashes. This emitted light is scintillation. A certain amount of emitted light falls on the photocathode of the PMT producing photoelectrons (Fig. 9-4). The photoelectrons are then accelerated by the electric field to the first dynode producing a bunch of secondary electrons. The electrons are again accelerated to the next dynodes until the electrons reach the anode with a gain of 10^7-10^8. Thus, the initial ionizing radiation gives a burst of electrons at the anode where an electrical pulse is taken out for further analysis.
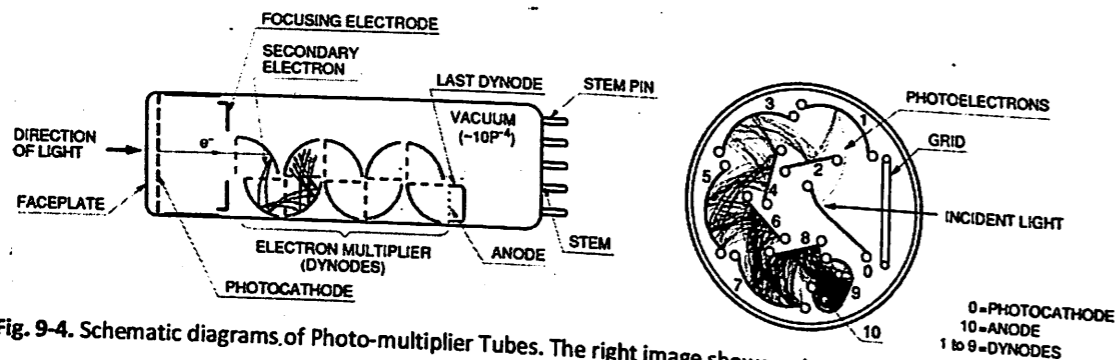
Fig. 9-4. Schematic diagrams of Photo-multiplier Tubes. The right image shows a circular-cage type PMT [8].

The scintillator detectors are most ideal for reactor neutrinos with energy range 3-8 MeV. Some of the experiments like Borexino, CLEAN, Daya Bay, Chooz, Double Chooz, KamLAND, LENS, MINERvA, MINOS, MINOS+, MOON, NOvA, RENO SciBooNE, SNO+, SoLiD, STEREO, JUNO, Braidwood, KASKA, Angra have the scintillation technique undertaken for study of neutrinos.

3.4. Iron Calorimeter (ICAL)

India-based Neutrino Observatory (INO) deploys the Iron Calorimeter (ICAL) technique for understanding the mechanism for detecting neutrinos. ICAL detectors generally detect muon neutrinos (v_μ) only, the INO-ICAL being sensitive to atmospheric v_μ in the 1-15 GeV range. ICAL consists of a number of alternating layers of iron plates of definite thickness and Resistive Plate Chambers (RPCs). The proposed ICAL @INO will have 5.6 cm thick iron plates and RPCs of area 1.84x1.84 m^2 weighing a total mass of 50 ktons. The 29,000 RPCs will be used as active medium for detection. The ICAL will be sensitive to the energy and directions of the muons produced in charged-current (CC) interaction of the atmospheric v_μ with the iron target in the detector. The muon neutrino interacts with the iron to produce a muon which is electrically charged. This charge is picked up by sensors in the RPCs which set off an electrical pulse, to be measured by the electronics. By piecing together the pulses set off in successive glass plates, the path followed by the muon is tracked. The ICAL @INO detector is expected to be magnetized to about 1.5 T in the plane of the iron plates using copper coils. This will able to discriminate between m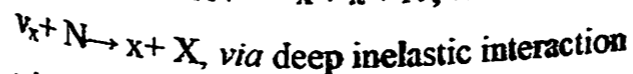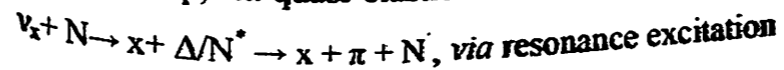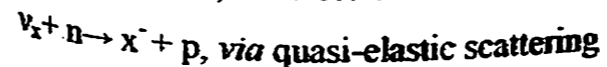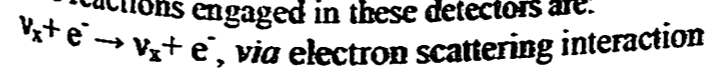uons of different charges and hence, it will be capable of differentiating events induced by v_μ and corresponding anti-neutrinos. Apart from INO, the MINOS experiment also used iron calorimeters to detect neutrinos. Some other experiments which take the advantage of this technique include NEMO-3 and SuperNEMO.

3.5. Liquid Argon (LAr) detector

D. Nyrgen, in 1974, introduced an idea of Time Projection Chamber (TPC) where the electron image of an event occuring in a noble gas is drifted towards a collecting multi-electrode array. A three dimensional image (x, y, z) of the event is then reconstructed from the (x, y) information and the drift time, t. In 1977, C. Rubbia extended the concept to liquefied noble gas, considering Argon, naming it as *Liquid Argon Time Projection Chamber (LAr-TPC)*. The Liquid Argon (LAr) detectors have good calorimetry and excellent particle identification capacity. The principle is simple. The charged particles will ionize the liquid argon and the ionized electrons can be drifted by an applied electric field. The electrons are then accumulated on wire planes which offer a 3D view of the interaction. The LAr detectors have very high neutrino detection efficiencies and excellent background rejection

power. Experiments like DUNE, ICARUS and MicroBooNE use this technique for neutrino detection. CLEAN uses liquid Neon and EXO-200 employ liquid Xenon instead of Argon in their experiments. The reactions engaged in these detectors are:

$v_x + e^- \rightarrow v_x + e^-$, *via* electron scattering interaction

$v_x + n \rightarrow x^- + p$, *via* quasi-elastic scattering

$v_x + N \rightarrow x + \Delta/N^* \rightarrow x + \pi + N$, *via* resonance excitation

$v_x + N \rightarrow x + X$, *via* deep inelastic interaction

where x is a charged lepton, N is a nucleon, Δ and N^* correspond to excited states, decaying with π, and X is a hadron.

4. Current Status of Neutrino: known and unknowns

The updated 2020 global best fit values [9] for the oscillation parameters, assuming normal hierarchy are:

$\sin^2\theta_{12}=0.304$, $\sin^2\theta_{13}(10^{-2})=2.221$, $\sin^2\theta_{23}=0.57$, $\delta_{CP}(^0)=195$

$\Delta m^2_{21}(10^{-5} eV^2)=7.42$, $|\Delta m^2_{31}|(10^{-3} eV^2)=2.514$,

The global fit gives more precise measurements of oscillation parameters of θ_{12}, θ_{13}, Δm^2_{21} and $|\Delta m^2_{31,32}|$. The sign of $\Delta m^2_{31,32}$ referred as mass hierarchy of the three mass eigenstates, the resolving of the octant degeneracy of mixing angle θ_{23} and determination of δ_{CP} have been studied extensively in the two global fits. The solar mixing angle is well measured by solar experiment while the corresponding mass-squared difference Δm^2_{21} is better constrained by KamLAND. The short baseline reactor-based experiments Daya Bay and RENO are sensitive to θ_{13} and $|\Delta m^2_{31,32}|$. The upcoming reactor-based medium baseline experiment JUNO promises to measure the solar parameters apart from θ_{13} and Δm^2_{31} with a better precision. T2K and NOvA are the only ongoing LBL experiments. Although in the global fit K2K and MINOS results besides them are also considered. The LBL experiments are sensitive to θ_{23} and Δm^2_{31} through the disappearance sample $v_\mu \rightarrow v_\mu$ ($\bar{v}_\mu \rightarrow \bar{v}_\mu$), to θ_{13} and δ_{CP} though their appearance $v_e \rightarrow v_\mu$ ($\bar{v}_\mu \rightarrow \bar{v}_e$) samples and to mass hierarchy resolution due to the matter effect potentials the neutrinos (anti-neutrinos) experience in their propagation to the detectors through Earth matter. However, MINOS/MINOS+ is sensitive to $|\Delta m^2_{31}|$ but not to θ_{13} and δ_{CP} due to its operation for muon neutrino disappearance search only. NOvA recently showed evidence of appearance of anti-neutrino with greater than 4σ confidence level (C.L.). T2K alone excludes the CP conserving values of δ_{CP} at almost 3σ C.L. The best fit value of δ_{CP} for T2K lies near $3\pi/2$ for NH, whereas for NOvA, it is 0.82π -close to CP conversing value π. However, for inverted hierarchy, the best fit of δ_{CP} is close to $3\pi/2$.

T2K has better precision for θ_{13} measurement than NOvA but it is not competitive to that of reactor-based short baseline experiments. As the disappearance sample is sensitive to $\sin^2 2\theta_{23}$, octant can't be resolved by this sample alone in long baseline experiments. However, the octant degeneracy can be resolved by adding appearance samples as the term $\sin^2\theta_{23}$ appears and also by considering Super Kamiokande and Ice Cube Deep Core data. The present best fit of θ_{23} lies in the upper octant. The lower octant is allowed at 2.4σ confidence level from the global data fits. Maximal mixing is now disfavored with a significance of $\Delta\chi^2 = 3.9$, including Super-K data.

With Super Kamiokande data included, inverted hierarchy is disfavored with 2.7σ C.L. Normal hierarchy is favored at 2.7σ C.L. considering all the experiments in the global fit. T2K and NOvA alone do not show any preference for any of the hierarchies due to $\Delta\chi^2$=0.4. However, adding all the LBL experiments with reactor experiments gives a boost of $\Delta\chi^2$=2.4 for preference to NH w.r.t IH. A combined analysis of accelerator-based, atmospheric and reactor-based neutrino experiments or joint analysis of the oscillation channels $v_\mu \rightarrow v_\mu$, $\bar{v}_\mu \rightarrow \bar{v}_\mu$, $v_\mu \rightarrow v_e$, $\bar{v}_\mu \rightarrow \bar{v}_e$ and $\bar{v}_e \rightarrow \bar{v}_e$ is crucial to resolve the unknown problems in neutrino oscillation.

5. Conclusions

In this review, we investigate the most common detection techniques employed in the neutrino oscillation experiments. We discuss the oscillation channels addressed by these experiments and the oscillation parameters they measure. Moreover, we describe the updated global fits of the mixing parameters. It is to be noted that there are neutrino experiments like SNO+, NEMO, SuperNEMO that test the Majorana nature of neutrino, and short baseline experiments like MiniBOONE, MicroBOONE, ICARUS and LSND among others that address the sterile neutrino hypothesis and they do not fall in the purview of this review. For detailed information on detection techniques and neutrino experiments, see Ref. [10] and the references cited within.

References

[1] C. L. Cowan, F. B. Harrison, L. M. Langer, F. Reines, II Nuovo Cimento. 3 (1956) 649–651.
[2] G. Danby, et al, Phys. Rev. Lett. 9 (1962)36.
[3] K. Kodama, et al, Phys. Lett. B. 504(2001)218–224.
[4] M. Kobayashi, T. Maskawa, Prog. Theor. Phys. 49 (1973) 652.
[5] Borexino Collaboration, Nature, 587(2020) 577–582.
[6] V.Milind, et al,Ann. Rev.Nucl. Part. Sci. 66, (2016) 47-71.
[7] J. V. Jelley, Brit. J. Appl. Phys. 6 (1955) 227.
[8] Photomultiplier Tubes Hamamatsu and Photomultipliers Tubes Photonics. Basics and applications. Hamamatsu Photonics KK, Iwata City, (2007).
[9] I. Esteban, et al, J. HighEnergy Phys.9 (2020) 178.
[10] A. Nath, Ng. K. Francis, Int. J. Modern Phys. A. (2021)2130008.

Chapter 10: LATERAL DENSITY DISTRIBUTIONS OF CHERENKOV PHOTONS IN EASs PARAMETERISED AS A FUNCTION OF PRIMARY ENERGY (E)

P. Hazarika

Duliajan College, Duliajan-786602
E.mail: poppyhazarika1@gmail.com

Abstract

The CORSIKA simulation code was used to simulate the lateral density distributions of Cherenkov photons in Extensive Air Showers (EASs) for a wide range of primary energy: from 100 GeV to 100 TeV and incident zenith angles from $0°$ to $40°$ over different altitudes of observation. Using these simulations we obtained a parameterisation of lateral density distributions (ρ_{ch}) as a function of energy for the primary γ-ray photons, protons and iron nuclei. This kind of parameterisation significantly contribute towards an understanding of the process of primary particle identification, reconstruction of the shower observables and an efficient disentanglement of the γ-ray showers from the hadronic showers. It can be seen from our parameterisation analysis that the lateral density (ρ_{ch}) distributions of Cherenkov photons follow a functional form $\rho_{ch}(E) = a E^{b}$ for the three given primaries at all the different values of zenith angle (θ), altitude of observation (H) and distance from the shower core (R), but with different values of function parameters (a) and (b).

Keywords: Gamma-ray Astronomy; Cherenkov Radiation; CORSIKA; EASs

1. Introduction

The understanding of origin, propagation and acceleration mechanisms of Cosmic Rays (CRs) constantly impinging the Earth's atmosphere with extraterrestrial particles of high, ultra-high, and extremely high energy remains one of the major unsolved problems till date in the field of CR research (Nakamura et al. 2010; Gaisser 1990; Blasi 2013; Bhattacharjee &Sigl 2000). The primary energy of CRs extends over twelve decades of energy with bulk of the CRs originating from within our galaxy. These CRs mainly consist of charged particles and are deflected isotropically in the intragalactic magnetic fields and thereby reaches us with no information regarding their source(s) direction(s). However, the sources that emit these CRs also emit γ-rays which are neutral and do not loose their direction during propagation. Thus instead of CRs, the detection of these competing γ-rays can also help us in determining the locations of such celestial sources. One of the techniques that is extensively used for such purposes is the Atmospheric Cherenkov Technique (ACT). ACTs mainly consist of ground based telescopes operating within the energy range of some hundred GeV to few TeV (Ong 1998; Holder 2015). The process is indirect and depends on the registration of a very brief flash of blue light known as the Cherenkov radiation. These radiations are emitted in the γ-ray initiated EASs due to the interaction of relativistic charged particles present in it and the atmospheric particles (Hoffman & Sinnis 1999; Weekes 2008; Bhat 2002). The method being indirect, necessitates the use of Monte Carlo simulations to properly analyze the data of the Cherenkov detectors. Synergy between the simulations and the real data ensures proper calibration of the detector array, effective rejection of the CR background, efficient determination of the primary energies and the incident γ-ray's arrival directions. From time to time various researchers from the field of High Energy Physics have carried out extensive studies to establish the dependence of the lateral density and arrival time distributions of Cherenkov photons on the energy of the primary, type of the primary particle, the radial distance from the shower axis, the direction of the shower axis (zenith angle) and the altitude of observation level (Chitnis& Bhat 2001; Al-Rubaiee et al. 2005; Abdulsttar et al. 2016). A spherical

wavefront that travels at the speed of light is used to fit the simulated data. Then the height of the shower maximum and the energy of the primary is estimated from the radius of curvature of this wavefront. The longitudinal distributions of the Cherenkov photons have also been parameterised as function of observation height (Rahman et al. 2001). Use of shower age parameters as a detection technique have been limited to the Cosmic Ray Community (Dey & Bhadra 2013). These studies provide better reconstruction of the longitudinal shower profile, primary energy and better composition measurements. Nerling et al. developed a parameterisation of the angular distributions of Cherenkov photons as a function of shower age and height in EASs (Nerling et al. 2006). The hadronic interaction model dependency of the lateral density and arrival time distributions of Cherenkov photons have also been carried out in details (Hazarika et al. 2015; Das et al. 2018). In our paper we try to parameterise the simulated Cherenkov photon's density distribution as a function of the primary energy (E) and analyze how this parameterisation depends on the distance (R) from the shower core, the incident zenith angle (θ) and the observation altitude (H). A small part of this study has already been presented in (Hazarika et al. 2015; Das et al. 2018).

The different aspects of our study has been outlined in our paper as follows. The detailed CORSIKA simulation process is discussed in Section 2 (Knapp & Heck 1998). A parameterisation is developed for the Cherenkov photons density distributions as a function of energy of the primary (E) for different values of distance from the showercore (R), zenith angle (θ) and altitude of observation level (H) in Section 3 followed by a discussion of results obtained in Section 4. Finally, in Section 5 we present the conclusions that can be derived from our work.

2. Corsika Simulations

For our study, the γ-ray, proton and iron initiated EASs have been simulated using the CORSIKA code (version 6.990). The hadronic interaction model QGSJET 01C has been used for the high energy interactions and GHEISHA 2002d for the low energy interactions (Knapp & Heck 1998; Kalmykov et al. 1997; Fesefeldt 1985). The electromagnetic components of the EASs are simulated using the EGS4 code (Nelson et al. 1985). QGSJET 01C and GHEISHA 2002d are relatively old interaction models. But since density distributions of Cherenkov photons show almost no dependency on the choice of hadronic interaction model and Cherenkov photon's average behaviour w.r.t different shower parameters remains same, the results will not be much affected (Hazarika et al. 2015). So, we have generated the EASs for energies ranging from 100 GeV to 100 TeV which fall within the typical energy range of ACT using this hadronic interaction model combination. We have selected these energies on the basis of their equivalent number of Cherenkov yields for both vertically incident monoenergetic γ-ray, proton and iron primaries as well as for those inclined at zenith angles 10°, 20°, 30° and 40° (Hazarika et al. 2015). Effect of altitude of observation level on the density distributions of Cherenkov photons has been studied using EASs generated at 500 m, 1075 m (Pachmarhi observation level, longitude: 78° 26′ E, latitude: 22° 28′ N), 2000 m, 3000 m and 4270 m (Hanle observation level, longitude: 78° 57′ 51″ E, latitude: 32° 46′ 46″ N) (Chitnis et al. 2009; Majumdar et al. 2003). The details of the EASs generated for the γ-ray, proton and iron primaries is listed in Table 10-1.

We have considered a flat horizontal detector array with each detector having an area of 9 m². The arrangement consists of 25 detectors in the E-W direction with a separation of 25 m and 25 detectors in the N-S direction with a separation of 20 m. In general this wide detector array is capable of detecting a large zenith angle TeV event. We have considered that the cores of the EASs are coincident with the centre of the detector array. Also, wavelength dependency of the Cherenkov photons emission angle is taken. The wavelength of the Cherenkov radiation is considered to lie in the 200-650 nm range. Hadrons, muons, electrons and photons are chosen to have threshold energies (in GeV) 3.0, 3.0, 0.003, 0.003 respectively. For each photon that hits the detector on the observation level, the position and time (with respect to the first interaction) are recorded. A choice of variable bunch size of Cherenkov photon as "5" is taken to reduce the size of the file. The parameter STEPFC in EGS code has been set to 0.1 (Nelson et al. 1985). Since, the choice of atmospheric models does

Table 10-1. Total number of EASs generated for the γ-ray, proton and iron primaries at different values of primary energies, angles of incidence and observation altitudes

Primary Particle	Energy	Number of Showers
γ-photon	100 GeV	10000
	500 Gev	5000
	1 TeV	2000
	2 TeV	1000
Proton	250 GeV	10000
	1 TeV	5000
	2 TeV	2000
	5 TeV	800
Iron	1 TeV	8000
	5 TeV	4000
	10 TeV	2000
	50 TeV	1000
	100 TeV	600

not have much effect on Cherenkov photon's density distributions, we have used the US standard atmospheric model parameterised by Linsley in our study (Das et al. 2018; USSA 1962).

3. Primary Energy (E) dependence of Lateral Density Distributions

For our parameterisation purpose, it is necessary to count the number of photons per shower that are incident on each detector. This gives us the lateral density of the Cherenkov photons. The variation of Cherenkov photon density with respect to core distance is calculated using their average values for the specified number of showers. This cancels out the effects of any inter shower fluctuations that may be present. In our work we will concentrate only on the parameterisation part w.r.t primary energy as the general features of Cherenkov photon density distributions have already been presented in (Hazarika et al. 2015; Das et al. 2018).

The variation of average density of Cherenkov photons (ρ_{ch}) as a function of energy (E) of γ-ray, proton and iron primaries for three different cases viz. different values of distance from the shower axis, incident zenith angles and altitudes of observation have been plotted in Fig.10-1. It can be seen from this figure that the Cherenkov photon density increases with energy for all the primaries. This is expected as in an EAS, the total number of Cherenkov photons produced is proportional to some power of the primary energy i.e. (Nerling et al. 2006; Al-Rubaiee et al. 2005; Das et al. 2018). In view of this we can parameterise the Cherenkov photon density distribution on energy of the primary as

$$\rho_{ch}(E) = a E^b \tag{1}$$

where $\rho_{ch}(E)$ is the energy dependent Cherenkov photon density function, a and b are function parameters having different values for different primaries, E is the energy of the primary. The solid lines in the plots in Fig.10-1 represent the best fit functions, given by Eq.(1). The χ^2-minimization technique available in the ROOT software has been used for these fittings (ROOT 2018).

4. Results and discussion

As is clear from Fig.10-1, our parameterisation works very well for the CORSIKA simulated data for different values of distance from the shower axis (R), incident zenith angles (θ) and altitudes of observation (H). Whereas proton and iron primaries produce hadronic showers along with the electromagnetic showers, the γ-ray primary produces only electromagnetic showers. The three primaries also have three different heights of the shower maximum as a consequence of which the γ-ray primary shows almost linear and faster rate of variation of ρ_{ch} with incident energy, whereas the proton and iron primaries indicate a comparatively slower and non linear increase in ρ_{ch} (Das et al.2018). This is verified by our parameterisation Eq.(1). To get a general idea about the fitting parameters in the Eq.(1), the fitted parameters of the ρ_{ch} distributions of γ-ray, proton and iron primary as a function of E at $H = 4270$ m, $\theta = 10°$ and $R = 50$ m are presented in Table 10-2.
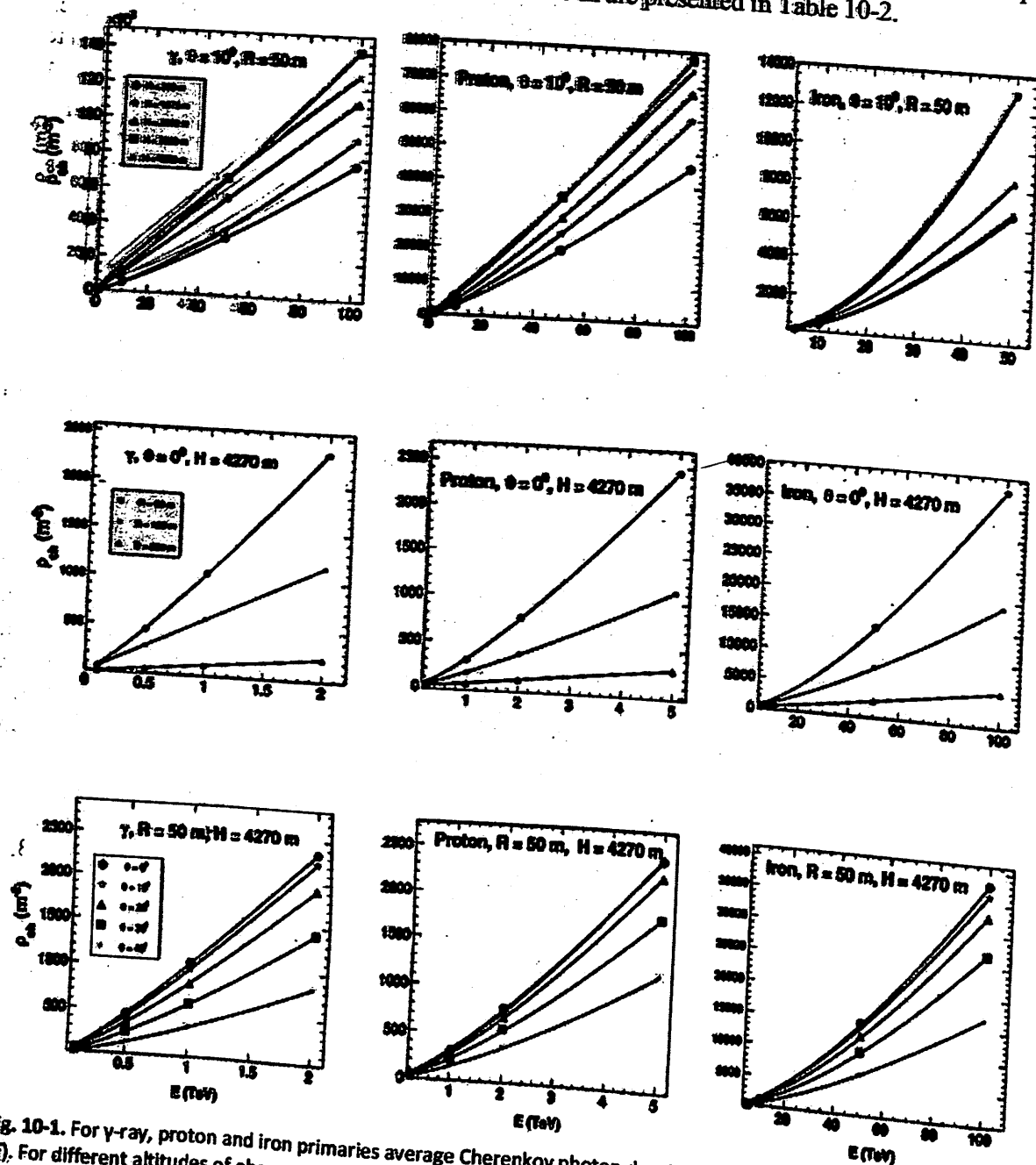

Fig. 10-1. For γ-ray, proton and iron primaries average Cherenkov photon density (ρ_{ch}) is plotted as a function of energy (E). For different altitudes of observation (H) keeping θ and R fixed these variations are plotted in the upper most panel. The same is plotted for different values of R keeping θ and H fixed in the middle panel. Finally, the bottom most panel shows plots for different values of θ keeping R and H fixed at a particular value. The solid lines represents the result of parameterisation Eq. (1) which lie within the limit of statistical error (< ±10%).

4. Conclusions

Table 10-2. For the energy dependent pch distributions of γ-ray, proton and iron primary, the fitted parameter values of Eq.(1) at H = 4270 m, θ = 10° and R = 50 m.

Primary	a	b
γ	11.1469 ± 2.49642	0.9220 ± 0.0349
Proton	0.0448 ± 0.0084	1.0638 ± 0.0309
Iron	0.0014 ± 0.0001	1.7027 ± 0.0002

We have developed an analytical model to parameterise the density of Cherenkov photons in EASs for the three primaries γ-ray, proton and iron primary as a function of energy of the primary (E) for different values of distance from the shower core (R), zenith angle (θ) and altitude of observation (H). This parameterisation is represented by Eq. (1). The estimated results of this parameterisation for the γ-ray, proton and iron primaries at different values of R, θ and H is then compared with the Monte Carlo simulations obtained using the CORSIKA 6.990 code (Knapp & Heck 1998). In general the lateral density of Cherenkov photons is in good agreement with the simulated CORSIKA data. For future work, the parameterisation should be tested over a wider range of energy. This should surely help us for better reconstruction of the shower variables which inadvertently would lead to better estimation of the primary energy and primary particle identification. It is also important to check the applicability of this parameterisation on real data obtained from the atmospheric detectors.

References

[1] K. Nakamura et al. (Particle Data Group), J. Phys. G: Nucl. Part. Phys. 37, 075021 (2010).
[2] T. Gaisser, Cosmic Rays and Particle Physics, Cambridge University Press, 1990.
[3] P. Blasi, Astron. Astrophys. Rev. (2013) 21:70.
[4] P. Bhattacharjee, U. Sigl, Phys. Reports 327, 109 (2000).
[5] A. René Ong, Phys. Reports 305, 93 (1998).
[6] J. Holder, arXiv:1510.05675 (2015).
[7] C. M. Hoffman, C. Sinnis, Rev. Mod. Phys. 71, 897 (1999).
[8] T. C. Weekes, AIP Conf. Proc. 1085, 3 (2008).
[9] P. N. Bhat, Bull. Astron. Soc. India 30, 135 (2002) & B. S. Acharya, Proc. 29th ICRC, Pune 10, 271 (2005).
[10] V. R. Chitnis, P. N. Bhat, Astropart. Phys. 15, 29 (2001).
[11] A. A. Al-Rubaiee, et al, Proc. 29th ICRC, Pune 6, 249 (2005).
[12] M. Marwah Abdulsttar, A. A. Al-Rubaiee, Halim Abdul Kh. Ali, arXiv:1612.08604 (2016).
[13] M.A. Rahman et al., arXiv:astro-ph/0104143v1 (2001).
[14] R. K. Dey, A. Bhadra, Astropart. Phys. 44, 68 (2013).
[15] F. Nerling, J. Blumer, R. Engel, M. Riss, Astropart. Phys., 24, 421 (2006).
[16] P. Hazarika, et al, Astropart.Phys. 68, 16 (2015).
[17] G. S. Das, P. Hazarika, & U. D. Goswami, Astropart. Phys. 100, 38 (2018).
[18] J. Knapp, D. Heck, EAS Simulation with CORSIKA V 6990: A User's Guide (1998); D. Heck et al.: Report FZKA 6019 (1998), Forschungszentrum Karlsruhe; http://wwwik.fzk.de/corsika/physicsdescription/corsikaphys.html.
[19] N. N. Kalmykov, S. S. Ostapchenko & A. I. Pavlov, Nucl. Phys. B (Proc. Suppl.) 52 B, 17 (1997).
[20] H. Fesefeldt, Report PITHA-85/02, RWTH Aachen (1985).
[21] W. R. Nelson, H. Hirayamal, D. W. O. Rogers, The EGS4 Code System, SLAC Report 265 (1985).
[22] V. R. Chitnis et al., Proc. 31st ICRC, Lodz, icrc0696 (2009).
[23] P. Majumdar et al., Astropart. Phys. 18, 333 (2003).
[24] US Standard Atmosphere (US Govt. Printing Office, Washington, 1962).
[25] ROOT Version 6.14/06 (2018); http://root.cern.ch/.

Chapter 11: A REVIEW ON APPLICATION OF UV SPECTROPHOTOMETRY FOR DETECTION OF FOOD FRAUD

Nilima Gogoi

Department of Physics, Duliajan College, Duliajan- 786602
E.mail: nilima.1.dc@gmail.com

Abstract

Economically motivated adulteration (EMA) or food fraud has become a world-scale problem in the present day economy. In order to fight food fraud, many analytical approaches are being adopted from time to time. The UV Visible spectrophotometric analysis is a basic analytical technique employed for the detection of food frauds. This method can be used for the analysis of both inorganic and organic molecules as well as some complex mixtures. This chapter provides a brief idea of the UV-Vis spectrophotometric technique and also discusses some applications of UV-Vis spectrophotometry for detection of food fraud.

Keywords: Economically motivated adulteration (EMA), Food fraud, UV-Visible spectrophotometry

1. Introduction

The adulteration of various types of food materials has become a matter of concern in today's day-to-day life. Economically modified adulteration (EMA), also commonly known as food fraud, is the process of substituting one or more ingredients of food or other types of intentional modification of food in order to gain profit [1]. In today's economic world, the issue of food fraud has become a world scale problem. In this direction, many different analytical methods are being adopted for the detection (and prevention) of EMA in food. One such method is the use of UV-visible spectrophotometry [2-12]. The UV-visible spectrophotometric method [13] is one of the oldest methods used in molecular spectroscopy and is based on the study of the absorption spectrum of various materials. This article discusses the use of the UV-visible spectrophotometric method for the prevention of EMA. The first part of the article gives a basic idea on UV-visible spectrophotometry, whereas the later part will provide a brief discussion on the use of this technique for the detection of intentional adulteration of food.

2. Spectrophotometry: Measurement of light absorption

The basic idea behind spectrophotometry involves the interaction of light with matter. When light falls on a substance, a part of the light may be absorbed whereas, the other part will get reflected. The absorption of light can be studied for the characterization as well as quantitative study of the experimental substance. In the UV-Vis spectroscopic technique [13], the sample under study is illuminated with electromagnetic rays having wavelengths in the ultraviolet range (UV), visible range (abbreviated as Vis) and part of the lower infrared region of the spectrum. When these wavelengths travel through the sample material, light is partially absorbed and the remaining light is transmitted through it, the absorption and transmission being dependent on the sample material. The transmitted light is recorded by a suitable detector which provides the sample's absorption spectrum as a function of wavelength.

The basic principle of the spectrophotometer is based on the Beer-Lambert law (also known as the Bouguer-Lambert-Beer Law) which relates the reduction of intensity of light passing through a solution to the concentration of the solution and the path length of light through that solution [13]. According to this law, if 'a' be the molar attenuation coefficient or absorptivity of the attenuating

substance, 'b' be the optical path length (or cell length) in cm, and 'c' be the concentration of the attenuating substance, the absorbance 'A' of light can be expressed as $A=a.b.c$ [13].

The Fig.11-1 shows the basic schematic of a single-beam spectrophotometer. The main components of the spectrophotometer are the following [13]:

2.1. Light sources:

Two types of lights sources may be present in the UV-visible spectrophotometer- (1) light sources which emit light in visible region and (2) light sources which emit light in the UV region. In case of the spectrophotometers which operate in the full UV-Vis region, both the visible light source and the UV light source are present. The change from one source to the other can be made either by a simple switch, or may take place automatically.

2.2. Monochromators:

One of the basic requirement of the spectrophotometric measurement is monochromatic (or at least approximately monochromatic having the narrowest possible bandwidth in the desired wavelength region) light. The function of the monochromator is to produce the monochromatic light needed for the measurement. Here, the beam of rays emitted from the light source having different wavelengths are passed through an entrance slit. In order to make this beam parallel, mirrors or lenses are placed before or after the slit. The parallel beam is then incident on the dispersing element (a prism or a diffraction grating) of the monochromator. The incoming radiation is deflected by the dispersing element over different angles, depending on the wavelength of the radiation. The deflected light is passed through the exit slit. This light which leaves the monochromator is approximately monochromatic light. The spectrophotometer shown in the Fig. 11-1 uses a grating based monochromator. It should be mentioned that in some light sources (e.g. mercury vapor lamps), a monochromator is not necessary; but a narrow wavelength region can be obtained by the application of appropriate filters, the undesired portion of light having different wavelengths being absorbed by the filter.

2.3. Cell and cell holders:

Cells used in the UV-visible spectrophotometer are made up of glass or quartz. The cells are provided with glass stoppers (or at least with lids) in order to avoid the evaporation of the sample solution as well as to prevent solvent vapors getting into other areas of the instrument. Cell holders are provided to accommodate cells of various pathlengths; the standard cell used very often being the rectangular cell having pathlength of 10 mm. The cell holder is designed in such a way that several solutions can be measured in succession. This can be achieved either by shaping the cell housing such
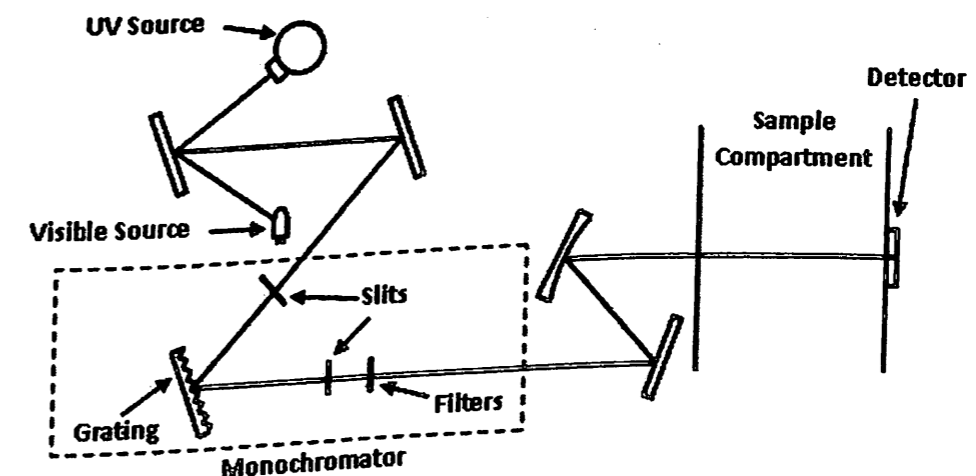

Fig. 11-1. Schematic of a single-beam spectrophotometer using a grating based monochromator

that a series of cells can be drawn into the path of light in succession, or by having specially shaped cells (in modern instruments) which can be emptied and washed after use and then filled up with a new solution without having to remove them from place.

2.4. Detectors:

In order to measure the absorbance, the light intensity is transformed to an electrical signal, such that the intensity of the electrical current is proportional to the intensity of the light. Different types of detectors used in the spectrophotometers are the photocells (used now-a-days in simple single beam spectrophotometers only), electron multiplier (or photomultiplier), silicon cell (used in the full UV-visible region), etc. The photocell is a vacuum tube with a half cylinder-like cathode, the surface covered with cesium antimonide (for use in the UV and visible region below 620 nm, referred to as the blue-sensitive cell) or cesium oxide (red-sensitive layer for use in case of higher wavelengths). An anode rod is present at the axis of the cathode. When illuminated, the material of layer at the cathode surface emits electrons, which move towards the anode, thus producing a photocurrent. The intensity of the photocurrent is proportional to the intensity of the light. After appropriate amplification, the current is measured. The electron multiplier (or photomultiplier) is a special form of vacuum photocell having a much greater sensitivity, and thus, a better spectral purity than with the conventional photocell. This is achieved by using a series of further electrodes called a dynode, also coated with cesium antimonide. The electrons emitted by the photocathode impinge on the first dynode, the secondary electrons emitted from the surface layer of the first dynode move towards the second dynode, etc. By using 8 to10 dynodes in series, with increasingly positive potential, a large photocurrent is obtained at the anode placed after the last dynode. Thus, this method is an excellent method for measuring low light intensities, free of noise amplification. The silicon cell is an alternative to the electron multiplier having a lower sensitivity, based on the property that the conductance of semiconductor silicon is directly proportional to the level of illumination. The easy miniaturization of the semiconductor silicon photodiodes is another added advantage in this direction. A very large number of diodes are mounted as an array, connected to small condensers. In the beginning of the measurement, all of these condensers are in the charged state and, will be discharged when light strikes the diode, to an extent proportional to the intensity of the light. The continuous measurement of the electrical current necessary to recharge them periodically at a high frequency will give a measure of the absorbance.

2.5. Monitors:

In this section of the spectrophotometer, the electrical signal obtained at the output of the detector is amplified electronically. In older instruments, the photocurrent is compensated by a current (scaled into absorbance units) generated from a potentiometer. In modern spectrophotometers, direct absorbance reading can be obtained using digital readout. It is also possible to get the absorbance values in printed form if the instrument be coupled with a microcomputer.

3. Spectrophotometry for detection of food fraud

The UV visible spectrophotometric method is a basic analytical technique used to detect food fraud. This section discusses few applications of this method in the detection of EMA in various types of food such as oil, meat, spices, coffee, etc. During the last two decades, there have been many works to report the application of UV visible spectrophotometry to study food adulteration.

The adulteration of olive oil with other inexpensive and low-quality seed oil is a frequently reported EMA in the food industry. The UV Visible spectrophotometric method has been used by various researchers to detect as well as to quantify the adulteration in olive oil. In the year 2010, J.S. Torrecilla used this method to study adulterations of extra virgin olive oil (EVOO) with other lower grade olive oil [2]. In his work, he calculated the various chaotic parameters from UV-vis scans of adulterated samples of EVOO and linearly correlated them with the adulterant concentrations from large number of adulterated samples of EVOO. Using an external validation process, this method not

only detected the presence of adulterant (refined olive oil and refined olive-pomace oil) in the extra virgin olive oil, but also helped to estimate the adulterant agent concentration. Using results from this work, it also became possible to measure impurities that may accidently be present in the given sample of extra virgin olive oil. A similar work was reported in 2013 by Lingling Jiang et al who proposed the UV spectrometric method coupled with principle component analysis (PCA) and partial least-squares regression (PLSR) as a potential method to detect and quantify adulteration in olive oil–vegetable oil blends [3]. The combined method was used in this work to discriminate the various blends of EVOO, other vegetable oils (such as corn oil, soybean oil, and sunflower oil) and palm oil. Aggelos Philippidis presented a comparative study on the use of the visible spectroscopic method for detection of adulteration of EVOO [4]. This work published in 2016, also focused on the Raman spectroscopic method which is another adulteration detection technique. Using samples of EVOO adulterated with sunflower oil, Philippidis presented a statistical analysis based on PSLR to show that the visible spectroscopy has an adulteration detection limit of 5.5%. He also commented this method to be rapid, noninvasive, and requiring no sample pretreatment. Another comparative study was presented by Oguz Uncu and Banu Ozen in the year 2019 which focused on the adulteration of fresh olive oils with old olive oils by using different spectroscopic approaches in combination with chemometrics, the UV-visible spectroscopy being one of them [5]. Adulterated samples of varying concentrations were analyzed using the various spectroscopic approaches combined with orthogonal partial least square-discriminant analysis (OPLS-DA) and partial least squares regression (PLSR) techniques. The UV spectroscopic method could successfully differentiate the adulterated and non-adulterated oils with over 90% correct classification rate and also successfully predicted the adulteration levels. Thus, this work established the UV–vis spectroscopy as a fast and environment friendly tool having great potential for both detection and simultaneous quantification of adulteration of fresh olive oil using old olive oil. Recently, Michael Didham et al used the UV–Vis spectroscopy as well as MIR(mid infrared) Spectroscopy Coupled with chemometric analysis for the purpose of adulteration detection of fresh olive oil with vegetable oils (canola and sunflower) [6]. The analysis of the absorption spectra of pure oils and mixtures of various concentrations obtained using UV-Vis (200–800 nm), it was established that UV-Vis spectroscopy can detect and quantify the adulterants present for adulteration levels above 10%. The results of their study is attributed to the different fatty acids present, products of the oxidation of lipids as well as the change in the pigment profiles in the oil samples.

The UV-visible spectroscopic method has been also used to study adulteration of other types of food products. In the year 2009, Carolina V. Di Anibal et al used this method, combined with multivariate classification techniques to study the presence of Sudan I-II-III-IV dyes as adulterant in commercial spices [7]. In their work, various commercial spice samples spiked with Sudan dyes with varying concentration were studied using three classification techniques namely the Partial Least Squares Discriminant Analysis (PLS-DA), Soft Independent Modelling of Class Analogy (SIMCA) and the K-Nearest Neighbour (KNN). Cristina Alamprese et al, in 2013 used the UV-visible spectroscopy (UV–vis), near infrared (NIR) spectroscopy and mid infrared (MIR) spectroscopy for detection of minced beef adulteration with turkey meat [8]. In this work, large number of samples of minced beef adulterated with turkey meat in different concentrations were analyzed along with samples of pure beef as well as pure turkey. This work, combined with PCA, LDA (Linear Discriminant Analysis), and PLSR established the UV-visible spectroscopic method as a potential solution for the detection of adulteration of minced beef. Pomegranate molasses syrups, a popular commercially available antioxidant is often reported to be adulterated with date molasses. Nada El Darra et al, in 2017, used the UV–Vis spectroscopic method to detect adulteration of commercial pomegranate molasses using date molasses [9]. UV–Vis spectroscopy coupled with High Performance Liquid Chromatography (HPLC) and Attenuated Total Reflectance Fourier-Transform Infrared (ATR-FTIR) analysis was used to analyze the samples of commercial pomegranate molasses, natural pomegranate molasses and date syrup in light of different parameters (viz. total acidity content, polyphenol yield, anthocyanins concentration, colour intensity, antiradical activity) that could signal adulteration. This method was seen to successfully detect and quantify the presence of date molasses syrups in commercial pomegranate molasses syrups.

The UV-Vis spectroscopic method is also used to detect EMA in various kinds of beverages. The UV-Vis spectroscopy coupled with Successive Projections Algorithm with Linear Discriminant

Analysis (SPA-LDA) is used to detect adulteration in ground roasted coffee [10]. Commercially available ground roasted coffee is a mixture of coffee and adulterants roasted together, resulting in degradation of the quality of the beverage. In 2015, researchers analyzed aquous extracts of ground roasted coffee (prepared in hot water) using the combined method to detect presence of adulterants. In the year 2017, Aggelos Philippidis used the UV-Vis spectroscopy for characterization of Greek Wines [11]. Philippidis presented his analysis of the UV-Visible Absorption Spectra, using principal component analysis (PCA) and hierarchical cluster analysis (HCA), combined with Statistical Multivariate methods. The properties taken under consideration for this work were the total phenolic index for different varieties of white and red wines and color characteristics for the red wine. The results could be used to discriminate the various varieties of wines and to infer the chemical compounds responsible for the discrimination. Recently, Sarah E. Fraser and Mathew J. Francis used UV-Visible spectroscopy along with low powered ultrasound for the characterization of single malt Scotch Whiskey [12]. In their work published in 2020, the techniques used could successfully track both the age and cask type of Scotch Whiskey as well as discriminate between the traditionally matured whiskey samples and alternatively aged whiskey samples (which utilize active maturation techniques and thus take shorter time to produce matured spirits having similar characteristics to the traditionally matured Scotch Whiskey). In addition, the spectrophotometric analysis could also quantify the antioxidant content of the Scotch Whiskey samples via a DPPH (1,1-diphenyl-2-picrylhydrazyl) assay.

4. Future prospects and Conclusion

The issue of economically modified adulteration (EMA) or food fraud has been increasing in different areas at an alarming rate. In this direction, the UV Visible spectrophotometric method is a highly preferred method to detect and quantify the EMA. The UV spectroscopic method, used in molecular spectroscopy, is based on the study of the absorption spectrum of various materials. This method is successfully used to study EMA in various types of food items (such as olive oils, dyes, minced meat, grounded coffee, alcoholic beverages, etc.). It can be used to analyze food items of any nature- inorganic, organic or some complex mixtures. Such studies prove that the method can be used to study adulteration in a wide range of other food items. Moreover, there is a possibility of more rigorous study to quantify adulteration in various food items by combiningthis method with other types of experimental techniques (e.g.- polarimetry to measure optical rotation, chromatography, etc.). At the same time, such combined experimental analysis can also be used to study various other properties of the material under observation.

References

[1] R. B.Petronijević, B. Velebit, and T. Baltić, In IOP Conf. Ser.: Earth Environ. Sci., Vol. 85, 012024 2017.
[2] J. S. Torrecilla, et al, J. Agric. Food Chem., 58 (2010), 1679-1684.
[3] L. Jiang, H. Zheng and H. Lu, J. Food Sci. Technol., 52 (2015), 479-485.
[4] A. Philippidis, et al, Anal. Lett., 50 (2017), 1182-1195.
[5] O. Uncu and B. Ozen, Food control, 105 (2019), 209-218
[6] M. Didham, et al, Food Anal. Methods, 13 (2020), 601-607.
[7] C.V. Di Anibal, et al,Talanta, 79 (2009), 887-892.
[8] C. Alamprese, et al, LWT-Food Sci. Technol, 53 (2013), 225-232.
[9] N. El Darra, et al, Food Control, 78 (2017), 132-137.
[10] U. T. D. C. P. Souto et al, LWT-Food Sci. Technol, 63 (2015), 1037-1041.
[11] A. Philippidis, et al, Anal. Lett., 50 (2017), 1950-1963.
[12] S. E. Fraser, and M. J. Francis, J. Inst. Brew, 127 (2021), 49-58.
[13] S. Gorog, Ultraviolet-Visible Spectrophotometry in Pharmaceutical Analysis, CRC Press, Inc., 2018.

Chapter 12: SOLVOTHERMAL ASSISTED SYNTHESIS OF NiMn₂O₄ NANOPARTICLE AND ITS ELECTROCATALYTIC APPLICATION TOWARDS METHANOL OXIDATION

Bhagyalakhi Baruah

Department of Physics, Duliajan College, 786602, Assam, India
E- mail: bhagyalakhi9@gmail.com

Abstract

This work reports the synthesis of $NiMn_2O_4$ nanoparticle by solvothermal assisted calcination method and its application in methanol oxidation. The current density of 15.07 mA cm^{-2} at an onset potential of 0.26 V in 0.5 M MeOH has been recorded at $NiMn_2O_4$ modified indium tin oxide (ITO) electrode. The improved electrocatalytic activity of $NiMn_2O_4$ can be attributed to the presence of rich binary active sites of Ni and Mn species. This work shows that $NiMn_2O_4$ can be a promising non-precious anode catalyst for methanol electro-oxidation.

Keywords: $NiMn_2O_4$, Direct methanol fuel cell, Electrocatalyst, Methanol oxidation, Solvothermal method.

1. Introduction:

In present times, degrading environmental conditions are major concern for researchers, hence innovation like direct methanol fuel cell (DMFC) which are environment friendly are of great importance. DMFC is a low temperature fuel cell, based on polymer electrolytes membrane technology and has a great potential to rise in market demand due to its eco-friendliness [1-3] and many other advantages such as high energy density (5.04 kWhL^{-1}), low cost, quick refuelling and low operating temperature (60-120 ^{0}C). However, slower oxidation kinetics of DMFC than that of hydrogen fuelled polymer electrolyte fuel cells due to methanol cross-over is the major limitation [4]. Therefore, extensive research works have been going on for the development of efficient anode catalyst to enhance the oxidation kinetics. The kinetics of methanol oxidation reaction (MOR) in DMFC can be increased by improving the electrode surface, electrolyte and electrolytic membrane [5, 6]. Platinum electrodes have long been used in DMFC, but high cost and CO poisoning make it difficult for commercialization [7].

The mixed transition metal oxides (MTMOs) of AB_2O_4 spinel structure, exhibit enhanced electrocatalytic performance such as chemical reactivity, anti-poisoning activity and stability than that of individual components [8, 9]. For example: $CoFe_2O_4$, $MnFe_2O_4$, $NiCo_2O_4$, $NiMn_2O_4$ have been used as the electrode materials in supercapacitors, Zn-Air and Li-ion batteries [10-13]. Among the various MTMOs, $NiMn_2O_4$ is structurally stable, high redox active sites, high electrical conductivity, low cost and electrochemically more active [14].

In the present work, we demonstrate the application of $NiMn_2O_4$ as an alternative to platinum anode catalyst towards methanol oxidation in alkaline media.

2. Experimental details:

2.1. Materials:

Nickel (II) chloride hexahydrate [$NiCl_2.6H_2O$, 98% Sisco Research Laboratories (India)], manganese (II) chloride tetrahydrate [$MnCl_2.4H_2O$, 99%, Merck (India)], oxalic acid [$(COOH)_2$

2H$_2$O, 99%, Fisher Scientific] have been used to prepare NiMn$_2$O$_4$. Indium Tin Oxide (ITO) conductive glasses have been procured from Macwin India Pvt. Ltd. All the experiments have been carried out using deionized (DI) water.

2.2. Synthesis of NiMn$_2$O$_4$:

In a typical synthesis process of NiMn$_2$O$_4$, 0.125g NiCl$_2$ and 0.246g MnCl$_2$ have been first mixed together with 50 ml ethanol and then stirred for 20 min and named as solution I. Then, 0.189 g oxalic acid has been added to 20 ml ethanol and stirred for 20 min and named as solution II. Both the solutions have been mixed together and stirred for 2 h. The reaction mixture has been then transferred to a 50 ml Teflon lined autoclave and heated at 130^{0}C for 10 h. Subsequently, the autoclave has been allowed to cool naturally and the green coloured precipitate has been filtered with repeated washing using DD water and ethanol and dried at 70^{0}C. Finally, the product has been annealed thermally at 370^{0}C for 3 h to produce black coloured NiMn$_2$O$_4$ powder [15].

2.3. Physicochemical and electrochemical characterizations:

Morphology of the prepared sample has been investigated using transmission electron microscopy (model JEOL JEM 2100) and structural characterization has been done using Raman spectroscopy (Model LabRam HR, Horiba Jobin Vyon) with 514.5 nm argon ion laser. The electrochemical measurements have been carried out in potentiostat/galvanostat (Autolab PGSTAT 302N, Metrohm, Netherlands) with a standard three electrode systems equipped with NOVA software. The electrocatalytic activity towards oxidation of methanol molecules has been investigated by cyclic voltammetry (CV) in a solution of 0.5 M NaOH + 0.5 M methanol at a scan rate 50 mVs^{-1}. The stability of the catalyst has been checked by chronoamperometry (CA) in a solution containing 0.5 M NaOH and 0.5 M methanol at a certain voltage for 3600 s.

3. Results and discussion:

The TEM image (Fig. 12-1(a)) of NiMn$_2$O$_4$ reveals the formation of spherical nanoparticles within diameter 35-40 nm. NiMn$_2$O$_4$ nanoparticles have been synthesized in precisely optimized reaction conditions to control size of the particles, however diameter of all the synthesized particles are not identical and lies within the range from 35 to 40 nm. Therefore, a particle size distribution (PSD) graph has been plotted by measuring the diameter of 100 randomly chosen particles as shown in Fig. 12-1(b). This PSD graph reveals a narrow size distribution of NiMn$_2$O$_4$ nanoparticles with a mean diameter of about 37.6 nm.
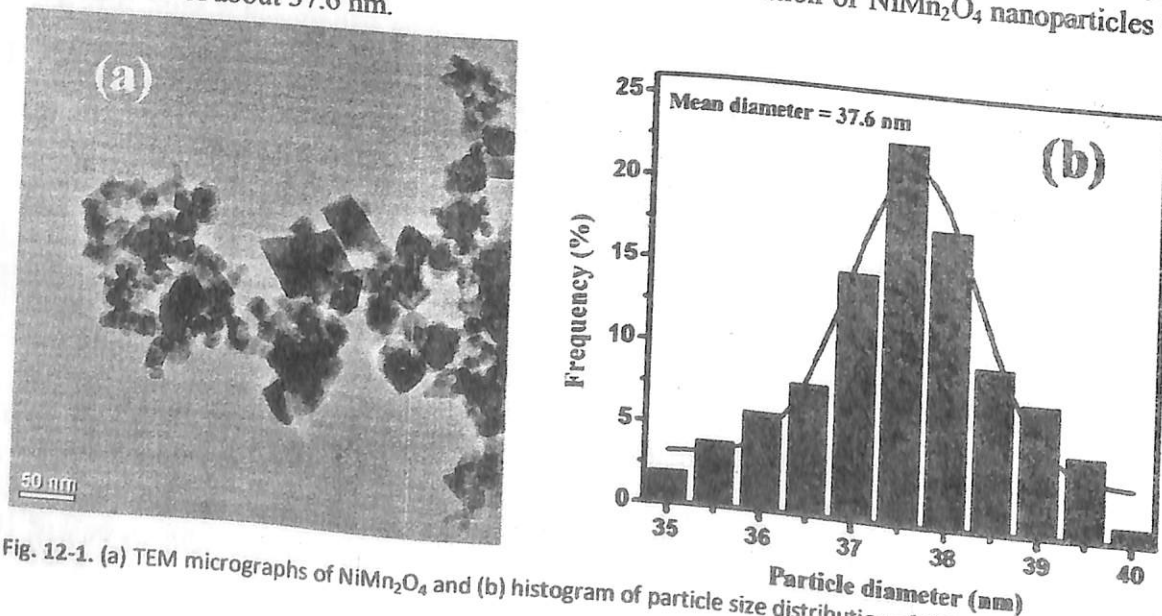

Fig. 12-1. (a) TEM micrographs of NiMn$_2$O$_4$ and (b) histogram of particle size distribution of NiMn$_2$O$_4$ nanoparticles

Raman spectroscopy is a widely used tool to analyse the structural properties such as defects and disorders present in the materials. The Raman spectra of NiMn$_2$O$_4$ in Fig. 12-2 displays three bands: first band at 625 cm^{-1} is attributed to A$_{1g}$ active mode related to asymmetric Mn-O stretching vibration mode of MnO$_6$ unit, the second band at 562 cm^{-1} is assigned to F$_{2g}$ mode and the third peak at 512 cm^{-1} is ascribed to Ni-O stretching vibration mode in NiMn$_2$O$_4$ [16, 17].

Fig. 12-2. Raman spectrum of NiMn$_2$O$_4$

As shown in Fig. 12-3(a), NiMn$_2$O$_4$ modified electrode exhibits a pair of redox peaks within the range from -0.24 V to +0.36 V, which mainly originates from the charge transfer processes through solid state redox pairs of Mn^{2+}/Mn^{3+} and Ni^{3+}/Ni^{2+} in the NiMn$_2$O$_4$. The redox peaks appear due to following reactions [18]:

$$NiMn_2O_4 + OH^- + H_2O \rightarrow NiOOH + 2MnOOH + e^- (1)$$
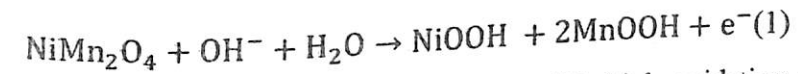
A good anode catalyst must exhibit high oxidation peak current at less onset potentials. NiMn$_2$O$_4$ modified indium tin oxide (ITO) electrode exhibits a current density of 15.07 mA cm^{-2} at an
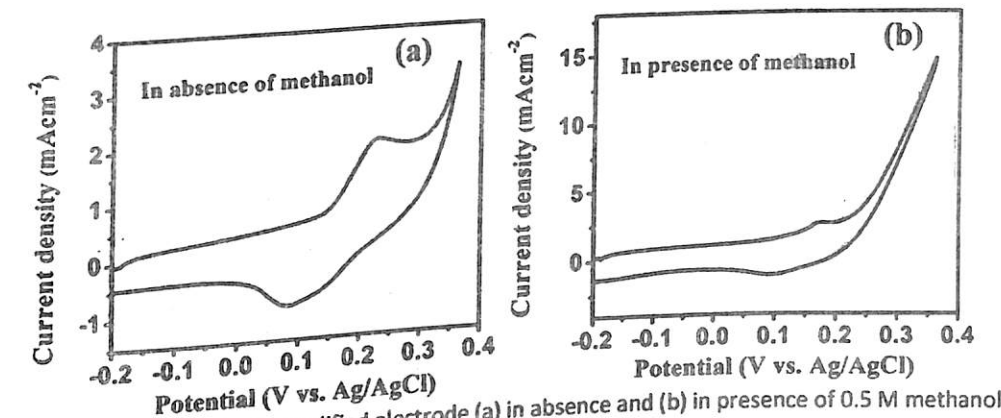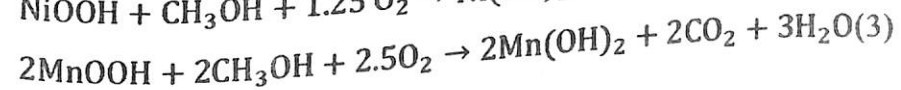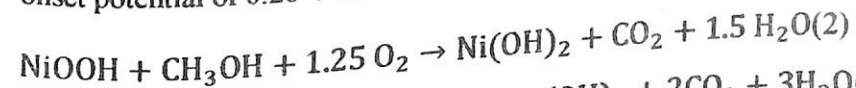

Fig. 12-3. CV curves of NiMn$_2$O$_4$ modified electrode (a) in absence and (b) in presence of 0.5 M methanol solution containing 0.5 M NaOH at a scan rate 50 mV/s.

onset potential of 0.26 V in 0.5 M MeOH (Fig. 12-3(b)).

$$NiOOH + CH_3OH + 1.25 O_2 \rightarrow Ni(OH)_2 + CO_2 + 1.5 H_2O (2)$$

$$2MnOOH + 2CH_3OH + 2.5O_2 \rightarrow 2Mn(OH)_2 + 2CO_2 + 3H_2O (3)$$

Initially, Ni and Mn in NiMn$_2$O$_4$ are oxidized to higher oxidation states (Eq. 1) and then the higher oxidation states of Ni and Mn oxidize methanol molecules and finally reduced back to lower oxidation states. NiMn$_2$O$_4$ is converted into NiOOH and MnOOH, which act as electroactive species in methanol oxidation [19]. The oxidation of methanol molecules initiates through the cleavage of C-C and C-H bonds and then forming the carbonaceous intermediates, which further oxidize to carbon dioxide and water.

The stability of electrocatalyst has been studied by the chronoamperometric (CA) measurements. The generation of the carbonaceous products during oxidation of methanol molecules causes poisoning and thus the sudden current decay within first few seconds and then current becomes uniform throughout the period for all the electrodes [20]. From Fig. 12-4, the values of steady current density after 100 s of methanol oxidation and current retention factor have been found to be 5 mA cm^{-2} and 24%, respectively.
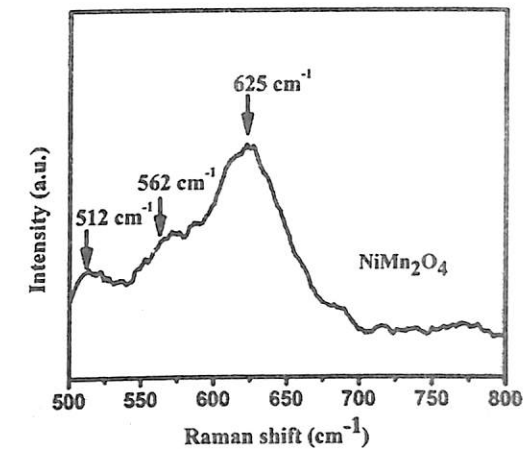
4. Conclusion:

In this work, $NiMn_2O_4$ nanoparticles have been synthesized by solvothermal method and the electrocatalytic performance of the synthesized nanoparticles has been investigated towards methanol oxidation. The successful formation of the particles has been confirmed by TEM microscopy and Raman spectroscopy. An oxidation current density of 15.07 mA cm^{-2} at an onset potential of 0.26 V has been exhibited by $NiMn_2O_4$ catalyst in 0.5 M methanol solution. The main role of redox active species (Mn^{2+}/Mn^{3+} and Ni^{2+}/Ni^{3+}) present in $NiMn_2O_4$ nanoparticles in methanol oxidation has been discussed by a given mechanism. The above results confirm that $NiMn_2O_4$ exhibits good electrocatalytic activity towards methanol oxidation.

Fig. 12-4. Chronoamperometric curves of $NiMn_2O_4$ modified ITO electrode with 0.5 M methanol containing in 0.5 M NaOH.

References:

[1] Y. Zhao, L. Zhan, J. Tian, S. Nie, Z. Ning, Electrochimica Acta 56 (2011) 1967.

[2] S. J. Zaidi, M. A. Rauf, Fuel cell fundamentals. In Polymer membranes for fuel cells, Springer, Boston, MA, 2009.

[3] P. Joghee, J. N. Malik, S. Pylypenko, R. O'Hayre, MRS Energy & Sustainability 2 (2015).

[4] O. O. Fashedemi, K. I. Ozoemena, Electrochimica Acta 128 (2014) 279.

[5] S. Ghosh, T. Maiyalagan, R. N. Basu, Electrocatalysts for Low Temperature Fuel Cells: Fundamentals and Recent Trends, 2017

[6] D. Sebastián, A. Serov, K. Artyushkova, J. Gordon, P. Atanassov, A.S. Aricò, V. Baglio, Chem. Sus. Chem 9 (2016) 1986.

[7] C. Sealy, Materials Today 11 (2008) 65.

[8] C. Goswami, K. K. Hazarika, P. Bharali, Materials Science for Energy Technologies 1 (2018) 117.

[9] H. Osgood, S. V. Devaguptapu, H. Xu, J. Cho, G. Wu, Nano Today11 (2016) 601.

[10] V. S. Kumbhar, A. D. Jagadale, N. M. Shinde, C. D. Lokhande, Applied Surface Science 259 (2012) 39.

[11] M. Fei, et al, ElectrochimicaActa 368 (2021) 137586.

[12] J. Yin, et al, Advanced Materials 32 (2020) 2001651.

[13] S. J. Rajoba, et al, Journal of Composites Science 5 (2021) 69.

[14] J. Huang, W. Wang, X. Lin, C. Gu, J. Liu, Journal of Power Sources 378 (2018) 677.

[15] J. P. Kumar, S. D. Giri, A. Sarkar, International Journal of Hydrogen Energy 43 (2018) 15639.

[16] X. Rong, et al, Journal of industrial and engineering chemistry 26 (2015) 354.

[17] G. George, S. Anandhan, RSC advances 4 (2014) 62009.

[18] A. Ray, et al, Applied Surface Science 463 (2019) 513.

[19] B. Baruah, A. Kumar, Synthetic Metals 245 (2018) 74.

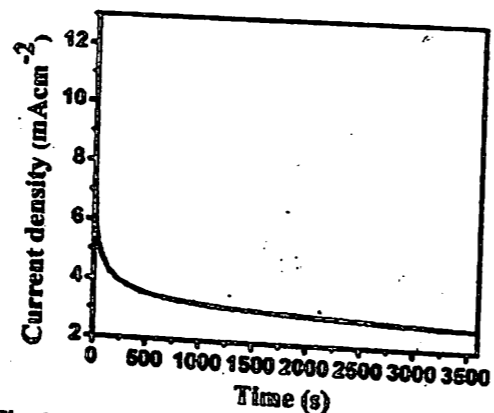[20] B. Baruah, A. Kumar, G. R. Umapathy, S. Ojha, Journal of Electroanalytical Chemistry 840 (2019) 35.

Chapter 13: SPIN POLARIZED FERROMAGNETISM IN HALF METALLIC FE DOPED ZnO

D. Saikia[a*], Hemant Kumar[b], J. P. Borah[b]

[a]Department of Physics, Duliajan College, Duliajan, Dibrugarh, 786602, Assam India
[2]National Institute of Technology Nagaland, Chumukedima, Dimapur, Nagaland, 797103, India
*Email:dipraj.saikia7@gmail.com

Abstract

Based on first principle calculations using GGA+U approach, we have studied the origin of room temperature ferromagnetism in Fe doped ZnO. The ferromagnetic coupling and the contribution of Fe-d states on the ferromagnetism of ZnO are studied. The p-d exchange interaction between the Fe-d and O-p states is responsible for the ferromagnetism at lower Fe concentration in ZnO, whereas at the higher concentration, the enhanced short range antiferromagnetic coupling between Fe ions dominates over ferromegnetism. The DOS results depicts that the Fe-d$_{t2g}$ state predominantly contributes the hybridization at the fermi level resulting the magnetism in the Fe doped ZnO system. The total energy calculations reveal the existence of short range ferromagnetic coupling in the system.

Keywords- Diluted magnetic semiconductors, Ferromagnetism, Density of states

1. Introduction

In the recent years, Diluted magnetic semiconductors (DMS) have been discerning materials with greater applications in spintronic devices due to their remarkable spin polarized property [1, 2]. In order to enhance the performances of spintronic devices such as magnetic storages and sensors, researchers have been focusing on transition metal (Fe, Mn, Ni, Co. etc.) doped DMSs [3-5]. Doping of transition metal elements into the DMS materials invoke magnetic coupling by inducing spin polarization in those materials [6, 7]. Among all DMSs, ZnO is the most suitable candidate for spintronics application due to its abundance and environment-friendly nature also a suitable optoelectronic material with a wide band gap 3.3 eV [8, 9]. It is essential to recognize the physical mechanisms responsible for the RTFM in these materials from both fundamental and technological prospective. Being a superior ferromagnetic transition metal with high curie temperature, it is covenient to use Fe as a doping agent in ZnO in order to introduce ferromagnetism into it [10, 11]. The exchange interactions between the unfilled d states of Fe contributes the RTFM in Fe doped ZnO.

In this report we have studied the magnetic properties of Fe doped ZnO and performed spin polarized DFT calculations using GGA+U approach to investigate the actual mechanisms responsible for the origin of RTFM in Fe doped ZnO. The magnetic coupling, formation energy and the magnetic moment are calculated and analyzed the effect of Fe-d state on the ferromagnetism of ZnO.

2. Experimental and Computational details

Nanoparticles of Fe-doped ZnO are synthesized by chemical co-precipitation method using zinc acetate [Zn $(CH_3COOH)_2 \cdot 2H_2O$] and sodium hydroxide (NaOH) as the precursor and ferric nitrate [Fe $(NO_3)_3 \cdot 9H_2O$] as dopant. By varying the molar concentration of ferric nitrate we have prepared Fe doped ZnO nanoparticles at doping percentages of 1%, 3%, 5%, 7% and 10%.

DFT calculations are executed by full-potential linearized augmented plane wave plus local orbital (FP-LAPW + lo) method implemented in the Wien2k package [12]. Perdew – Burke – Ernzerhof generalized gradient approximation with the Hubbard correction (GGA+U) is used for the exchange correlation potential [13, 14]. A plane wave cut off of RK_{max}= 6 is used for self-consistence method and 1000 k-points with 10×10×10 k-mesh are used for the sampling of brillouin zone. We have

constructed a 2×2×2 supercell of ZnO, substituting one Zn atom by a Fe atom for spin polarized calculations.

3. Results and discussion

Fig. 13-1(a) displays the refined x-ray diffraction spectrum of 1% Fe doped ZnO nanoparticles which demonstrates the formation of hexagonal Wurtzite structure of ZnO with crystallite size of ~38nm. No additional peaks for secondary or mixed phases are detected in the XRD spectra which signify the phase purity of the samples [4]. We didn't observe any appreciable difference in XRD spectra at other percentages of Fe, and therefore those spectra are not displayed. The variation of magnetization with respect to applied magnetic field for Fe doped ZnO nanoparticles recorded at room temperature are depicted in fig. 13-1(b). All the samples show S-shaped hysteresis loop with ordered magnetic structure. It is observed that at 1%-7% doping percentage of Fe, the M-H curves show decent ferromagnetic properties with the values of saturation magnetization between 0.0633 emu/gm to 0.10297 emu/gm. The p-d exchange interaction between the localized d-states of Fe present on the surface of nanoparticles and the p-states of O gives rise to resultant magnetization to the sample [8, 15].The room temperature ferromagnetic behavior can be attributed to the interaction between the smaller magnetic dipoles located on the surface of the nanocrystals and the nearest neighbors. Accordingly, the exchange energy in those magnetic dipoles makes the neighboring
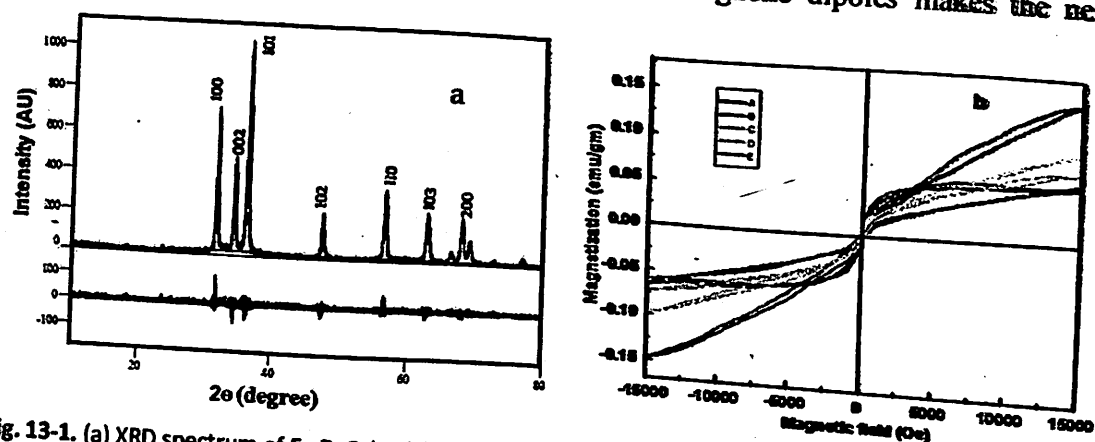

Fig. 13-1. (a) XRD spectrum of Fe:ZnO (1%) (b) Room temperature M-H curves of Fe doped ZnO nanoparticles at 1% (A), 3% (B), 5% (C), 7% (D) and 10% (E) doping percentage

dipoles to be oriented in the same direction. Due to the higher surface to volume ratio in the nanocrystals, the population of magnetic dipoles oriented in the same direction will increase at the surface. Subsequently, the total magnetic dipoles oriented along the same direction will increase which results the crystal surface to become more magnetically oriented [16]. However, when the doping percentage of Fe is increased to 10%, the antiferromagnetic super exchange interaction between the Fe atoms dominates overall ferromagnetic nature of the samples [17, 18]. Prashant K. Sharma et al., [16] observed similar ferromagnetic behavior in Fe doped ZnO nanoparticles for the lower concentration of Fe. Similar type of variations was also observed by several co-workers in Fe doped ZnO nanoparticles [17, 19, 20, 21].

In order to determine the magnetic stability and ferromagnetic coupling of Fe doped ZnO system, the formation energy and the total energy difference between ferromagnetic (EFM) and antiferromagnetic (EAFM) [EAFM - EFM] states have been calculated as displayed in table 13-1. It is clear from the table that all the configurations possess ferromagnetic coupling except the configuration I. The configuration I demonstrates ground state as antiferromagnetic state which is in agreement with the experimental results. When the separation between Fe is less, the short range antiferromagnetic coupling dominates, as observed in the M-H curve in the Fig. 13-1(b) at higher concentration of Fe. Particularly, the magnetic moment and ΔE decreases with increasing Fe-Fe separation for the configurations II-IV which indicates that Fe doped ZnO system exhibits short range ferromagnetic coupling. Similar results were also obtained by G. Shaoqiang et al., [20] in Fe doped

Table 13-1. The energy difference in ferromagnetic and antiferromagnetic states of Fe atom in Fe doped ZnO system and the corresponding formation energies

Configuration	Fe-Fe separation (Å)	E_{FM} (eV)	E_{AFM} (eV)	Energy difference (ΔE) (eV)	Formation energy (eV)	Magnetic moment (μ_B)
I	2.26	−46,379.8752	−46,379.8962	-21.0	-1.01	2.98
II	2.89	−48,672.8562	−48,672.8263	29.9	-1.03	3.95
III	3.54	−49,784.2864	−49,784.2596	26.8	-0.95	3.79
IV	4.21	−50,721.7965	−50,721.7763	20.4	-0.85	3.65

ZnO. Subsequently the negative values of the formation energy demonstrate the greater stability of the system and can be easily manufactured experimentally [22].

The spin polarized total density of states Fe doped ZnO system for spin up and spin down configurations are depicted in Fig. 13-2. In the spin up state, the valence band is occupied by the Fe-d, Zn-d and O-p states, while the conduction band is occupied by some Zn-d and O-p states. Consequently, it shows semiconducting nature with band gap of 0.78eV that is much smaller compared to the bulk ZnO (3.40eV) due to band gap underestimation of DFT [22]. In contrast, for spin down state, the fermi level is filled by Fe-d and O-p states displaying a significant hybridization between Fe-3d states and O-2p states, which portrays the half metallic character of doped ZnO with 100% spin polarization [23, 24].
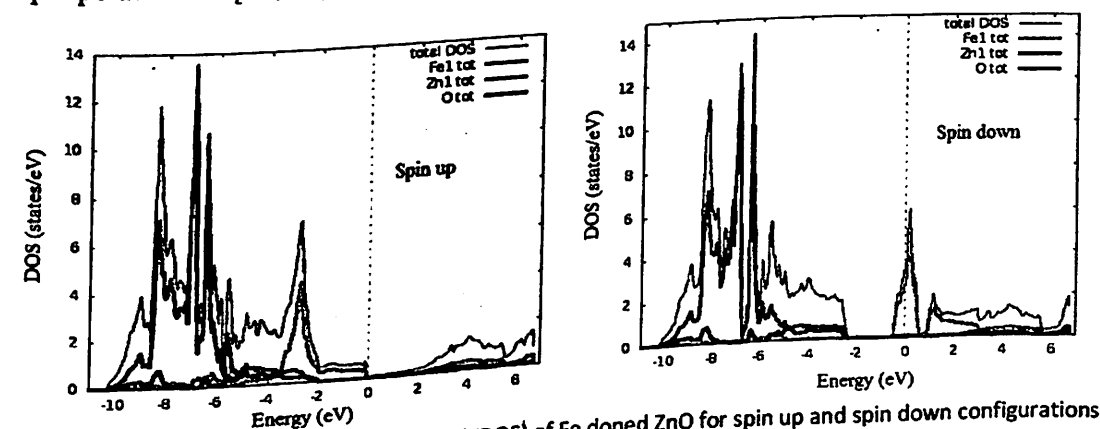

Fig. 13-2. Spin polarized total density of states (TDOS) of Fe doped ZnO for spin up and spin down configurations

In order to identify the degenerate level of Fe-d state that takes part into the hybridization, the projected DOS for single Fe atom is illustrated in Fig. 13-3. It is observed that the fermi level is filled by t_{2g} degenerate level of Fe-d state without any contribution of eg level. In the spin up configuration, Fe-dt_{2g} states have 4 energy states/eV, which is at -2.5eV from Fermi level. Whereas, in the spin down configuration, Fe-dt_{2g} states have 5 states/eV exactly at the Fermi level. Thus, it can be established that Fe-dt_{2g} state predominantly takes part in to the p-d hybridization process for spin down state resulting pin polarized behaviour in Fe doped ZnO system [25].

4. Conclusions:

In conclusion, we have investigated the origin of RTFM in Fe doped ZnO and studied ferromagnetic coupling mechanisms and the electronic structures of the system. We observed RTFM at lower concentration of Fe to the p-d exchange interactions between localized d spins and free delocalized carriers. The total energy calculations demonstrate the existence of short range
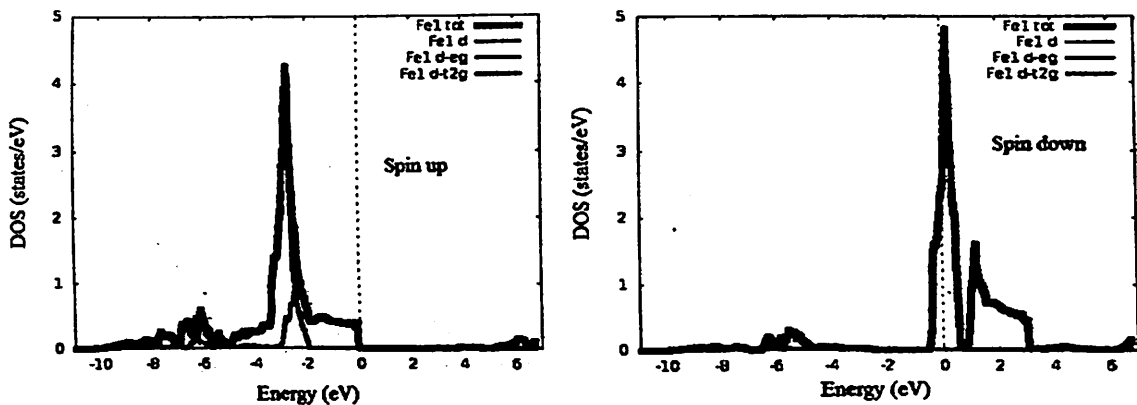
Fig. 13-3. Spin polarized density of states (PDOS) Fe-d eg and t_{2g} degenerate states for spin up and spin down configurations

ferromagnetic coupling for Fe-Fe separation of 2.89 Å with a magnetic moment of 3.95 μ_B. Whereas for high concentration of Fe (10%) and Fe-Fe separation 2.26Å, the system shows antiferromagnetic coupling which dominates the ferromagnetism. The electronic structure calculations show half metallic character of ZnO:Fe with the filled fermi level in spin down configuration by t_{2g} degenerate level of Fe-d state that contributes the p-d hybridization process. From the formation energy calculations, we can conclude that Fe doped ZnO can be experimentally manufactured very easily and can be utilized in spintronic devices.

References:

[1] J. K. Furdyna, J. Appl. Phys. 64 (1988) R29

[2] H. Ohno, H Science. 281 (1998) 951

[3] S. Fathhoor Rabbani, I. B. Shameem Banu, Comp. Mater. Sci. 101 (2015) 281–286

[4] C. Xia, C. Hu, Y. Tian, P. Chen, B. Wan, J. Xu, Solid State Sci. 13 (2011) 388-393

[5] B. Panigrahy, M. Aslam, D. Bahadur, Nanotechnology 23 (2012) 115601

[6] C. E. Housecroft, A. G. Sharpe, Inorganic Chemistry, (2nd eds), Pearson Prentice-Hall, ISBN:13: 978-0130399137 20-21 (2005)

[7] A. Saha, et al, Phys. Chem. Lett.7 (2016)2420-2428

[8] H. Shi, Y. Duan, J. Appl. Phys. 103 (2008) 073903

[9] M. H. Huang, Set al, Science 292 (2001) 1897

[10] A. Gonano, R. E. Zich, M. Mussetta, Prog. Electromagn. Res. B, 64 (2015) 83-101

[11] G. Gu, et al, J. Appl. Phys. 112 (2012) 023913

[12] K. Schwarz, P. Blaha. G. K. H. Madsen, Comput. Phys. Comm. 147 (2002) 71

[13] Y. Wang. J. P. Perdew, Phys. Rev. B 44 (1991) 13298

[14] V. I. Anisimov, F. Aryasetiawan, A. Lichtenstein, J. Phys.: Condens. Matter, 9 (1999) 767-808

[15] A. Sahai, Y. Kumar, V. Agarwal, S. F. Olive-Mendez, N. Goswami, J. Appl. Phys. 116 (2014) 164315

[16] P. K. Sharma, et al, J. Magn. Magn. Mater. 321 (2009) 2587

[17] T. A. Abdel-Baset, et al, Nanoscale Res Lett. 11 (2016) 115

[18] B. Pal, S. Dhara, P. K. Giri, D. Sarkar, J. Alloys. Compd. 615 (2014) 378–385

[19] Karmakar, et al, Phys. Rev. B. 75 (2007) 144404

[20] G. Shaoqiang, H. Qingyu, X. Zhenchao, Z. Chunwang, Physica B 503 (2016) 93–99

[21] P. K. Sharma, R. K. Dutta, A. C. Pandey, J. Colloid interface Sci. 345 ((2010) 149

[22] H. Q. Xie, L. J. Tang, P. Peng, J. Magn. Magn. Mater. 377 (2015) 239

[23] B. Belhadji, et al, J. Phys.: Condens. Matter 19 (2007)436227

[24] P. Eckelt, O. Madelung, J. Treusch, Phy. Rev. Lett. 18 (1967) 16

[25] S. Tariq, et al, Eur. Phys. J. Plus 133 (2018) 87